Piezo-Induced Fatigue of Solder Joints

by

Catherine L. Sanders

B.S. Mechanical Engineering (1997)
B.S. Materials Engineering (1997)
Drexel University

Submitted to the Department of Aeronautics and Astronautics
in Partial Fulfillment of the Requirements for the Degree of

Master of Science in Aeronautics and Astronautics
at the
Massachusetts Institute of Technology

June 2000

© 2000 Massachusetts Institute of Technology.
All rights reserved.

Signature of Author:_____
Department of Aeronautics and Astronautics
May 19, 2000

Certified by:_____
S. Mark Spearing
Esther and Harold E. Edgerton Associate Professor of Aeronautics and Astronautics
Thesis Supervisor

Accepted by:_____
Nesbitt W. Hagood IV
Associate Professor of Aeronautics and Astronautics
Chairman, Department Committee on Graduate Students

MASSACHUSETTS INSTITUTE OF TECHNOLOGY
SEP 07 2000
LIBRARIES
Aero

PIEZO-INDUCED FATIGUE OF ADHESIVE JOINTS

by

Catherine L. Sanders

Submitted to the Department of Aeronautics and Astronautics
on May 19, 2000 in Partial Fulfillment of the
Requirements for the Degree of Master of Science in
Aeronautics and Astronautics

ABSTRACT

Piezomechanical loading of an adhesive joint is a very close analogue to the loading imposed by adherends with dissimilar thermal expansion coefficients under a temperature change. Using this concept, a double lap joint test specimen was developed to investigate the damage mechanisms in solder joints for electronic packaging applications under cyclic loading conditions. Analytical results are derived for the plastic shear strain at the free edges of such a specimen using a shear lag model. Results are also presented for the strain energy release rate for steady state crack growth. Experimental results and observations are presented for the damage processes in lead-tin eutectic solder joints between PZT-5H adherends. The lifetime of a specimen can be divided into two regimes: initiation and steady crack growth. Cracking was generally observed to initiate at voids and other defects in the solder joint. The time to initiate damage, the total joint life, and crack growth rates were quantified as a function of applied loading. Data for damage initiation was quite scattered, reflecting the variation in joint quality, but broadly conformed to a Coffin-Manson relationship. The data for crack growth rate approximately corresponded to a Paris law at higher applied voltages. At lower voltages, a strong dependence on frequency was observed, and there was evidence of a threshold strain-energy release rate. Crack growth rates increased with increasing temperature over the range 0-25°C, but decreased up to 80°C. The appendices detail the specimen manufacturing techniques, the experimental set-up, and the testing methods and regime. An expanded literature review for this work is also provided in the appendices for further background and insight as to the issues surrounding adhesive fatigue.

Thesis Supervisor: S. Mark Spearing
Title: Esther and Harold E. Edgerton Associate Professor of Aeronautics and Astronautics

Acknowledgments

Reflecting on my experience at MIT, I realize what valuable learning and life experiences I have gained. In the last three years, I developed great educational insight, but more importantly, insight into myself. It has been a road of self-discovery and awareness. Along this journey, I have had many who have helped me, some of those contributed advice, others offered a helping hand, some taught a needed skill or simply were friends, and a special few picked me up when I thought I could not continue, reminding me to look toward my goals, to follow my heart and my dreams. To all of you, my sincere thanks.

I wish to thank the Department of Defense for awarding me the National Defense Science and Engineering Graduate Fellowship that allowed me to pursue my education at MIT. I also wish to thank Rockwell International for supporting my expenses during the summer of 1998 and sponsoring the experimental work both at Rockwell Science Center and at MIT. Additionally, there are a few shining individuals that I especially wish to acknowledge at this time for their contributions. First, I wish to thank my husband, Wynn, whose continual support and love has been my pillar of strength. Wynn, you are my true soul mate; without you, my life would not be complete. I also wish to thank my parents, Roger and Janice Miller. Dad, in many ways, you are my inspiration. Mom, your love and unending devotion enable my dreams to become a reality. The next couple I wish to thank are my best friends, Ann Calamia and Eric Rohrbaugh – Eric for providing technical support and Ann for providing emotional support and for teaching me the value of the road not taken. I would be remiss if not to thank my good friend, Staci Jenkins. Staci, in the face of challenge, it was comforting to know I had a friend at my side. A special thank you to Chris Dunn, the only other TELAC graduate student who understands the value of the night shift. Jocelyn Wiese, my MIT UROP, also deserves a warm word of thanks for her helping hand. To my friends Craig Winterhalter and Stephanie Voss from California, thanks for helping an East-coast girl survive on the West coast and for being true friends in my home away from home for three months. Craig, I cannot thank you enough for all your long hours helping me with the design and construction of the voltage cycling circuit, plus all your other technical help. I could not have done it without you. Mike Shaw from Rockwell Science Center deserves great thanks for allowing me to use Rockwell's facilities for sample production and giving me the resources to advance this research.. Thank you to my angels, Paul Bissonette and Steve Tower, from Olin-Aegis who allowed me to use their facilities to complete my sample production when I had only five samples left and what seemed like 500 more tests to go. It is always important to remember one's roots. Therefore, I wish like to thank my professors at Drexel University, especially Profs. Gary Ruff, Roger Doherty, and Linda Schadler, for helping me build a strong foundation in science and engineering and encouraging me to reach for the stars. Finally, saving the best for last, I would like to especially thank my advisor, Mark Spearing, who made the dream of coming to MIT a reality and allowed me to be part of his cutting-edge scientific research. Mark, your insight and example taught me more than I could ever learn from a textbook. Thank you for your patience and understanding throughout my entire experience at MIT. Each of you have in your own way shaped me, creating who I am today, and for this I am ever grateful.

Two roads diverged in a yellow wood,
And sorry I could not travel both
And be one traveler, long I stood
And looked down one as far as I could
To where it bent in the undergrowth;

Then took the other, as just as fair,
And having perhaps the better claim,
Because it was grassy and wanted wear;
Though as for that the passing there
Had worn them really about the same,

And both that morning equally lay
In leaves no step had trodden black.
Oh, I kept the first for another day!
Yet knowing how way leads on to way,
I doubted if I should ever come back.

I shall be telling this with a sigh
Somewhere ages and ages hence;
Two roads diverged in a wood, and I –
I took the one less traveled by,
And that has made all the difference.

- Robert Frost

Table of Contents

1. Introduction

The thermomechanical fatigue of solder joints is a common cause of failure of microelectronic devices. Notwithstanding the importance of this failure mode, there is a general lack of clear guidelines for the selection of materials, the design, and the manufacturing of solder joints to ensure their reliability. This reflects the fact that the lifetimes of solder joints in service are governed by multiple interacting factors. Typically, fatigue failures occur in solder joints between sub-components with different thermal expansion characteristics, either because of the use of dissimilar materials, or because of thermal gradients in the device. Thus, when the device is turned on or off, a temperature change occurs and the solder joint is subjected to a stress/deformation cycle. This mechanical loading couples with time-dependent material responses. Since solders are low melting point alloys (T_m ~ 200°C), creep effects are significant over the temperature range of a typical thermal cycle (-50 to +150°C). Furthermore, prolonged operation at elevated temperature can lead to diffusion-controlled processes, such as grain growth, segregation, void growth and diffusion of metallization layers into the bulk of the solder. Anecdotal evidence also suggests that the presence of voids, the shape of fillets at the edge of joints, the metallizations applied to the adherends, and the solder layer thickness all play important roles in determining joint reliability.[1-4] It is difficult to separate the relative importance of these effects experimentally to determine the fatigue life. Generally, testing consists of power cycling complete devices, or thermal cycling, which is achieved by alternately transferring devices between hot and cold environments. These approaches inevitably result in both cycle-dependent and time- and temperature-dependent effects occurring simultaneously. This convolution of degradation processes has hitherto prevented the construction of effective models for the failure of solder joints. Various investigators have developed methods to apply purely mechanical loading to solder joints in attempts to isolate the mechanical contribution to solder fatigue.[5] However, applied mechanical loading does not exactly replicate the stress and strain state that is induced by thermal expansion mismatch, particularly for the case of lap joints with relatively large bonded areas, as opposed to solder bumps, pin attachments, or wire bonding.

The hypothesis behind the work presented in this paper is that piezo-actuation can be used as an analogue of thermal cycling. The deformation of piezo-ceramic materials under an electric field is similar to thermal expansion-induced deformation. By actuating piezo-ceramic substrates soldered together, a stress and strain state can be induced in the solder, which is nearly identical to that which would be produced in a joint between two dissimilar adherends

with a thermal expansion mismatch under thermal cycling conditions. Since the piezo-actuation does not involve a temperature change, this approach should make it possible to separate the effects of mechanical fatigue from time and temperature dependent effects. Two further opportunities are provided by this piezo/thermal analogue. Firstly, the rate of thermal cycling is limited by the time required for the specimen to reach thermal equilibrium before the temperature is reversed. This limits the frequency of testing to the order of four cycles per hour for liquid to liquid testing, and even slower rates for gas to gas testing.[6] Given the high frequency capability of piezo-ceramics, the potential exists for performing accelerated testing. Secondly, since test specimens do not have to be transferred between chambers of hot and cold fluids, it is easier to make *in situ* observations of damage accumulation during cycling. This capability is important in isolating the mechanisms of solder fatigue failure.

The research presented in this thesis shows experimental results and supporting analysis of the capability to use piezo-actuation to cyclically load solder lap joints to failure. Section 2 presents mechanics analyses of the analogy between thermomechanical and piezomechanical actuation of solder joints. Section 3 presents the experimental details of the manufacturing and testing of the piezo-actuated solder fatigue specimens. Section 4 presents the experimental results. Section 5 contains a discussion of the results and section 6 presents some conclusions and suggestions for future work.

2. Modeling

The fatigue failure of solder joints can be divided into two regimes: damage initiation and damage growth.[7] For different joint configurations, solder types, and loading cases, either regime may control the overall lifetime of the joint. In this section, these two regimes are treated separately. The analysis presented here will focus on the double lap joint configuration shown in Figure 1. This geometry has several experimental advantages over a single lap joint, which is more commonly found in microelectronic applications. The symmetry of the specimen eliminates bending deformations by actuating the piezo-ceramic adherends 180° out-of-phase, which reduces the likelihood of cracking of the brittle piezo-ceramics. Additionally, actuating the piezo-ceramics out-of-phase increases the deformation in the solder for a given applied voltage to the piezo-ceramic adherends.

Fatigue Damage Initiation

The fatigue life of ductile materials, including solders, has been empirically correlated with the plastic strain range experienced by the material. A simple approach to relating the plastic strain range in an adhesive joint to the applied loading (thermal or piezo) is to use a one dimensional shear lag model.[8]

Consider a symmetric tri-layer joint configuration as shown in Figure 1. The adherends, materials 1 and 2, are considered to be perfectly elastic and the solder is modeled as being perfectly plastic with a constant shear strength, τ. The thermoelastic behavior of the solder is ignored, as is any shear deformation of the adherends. A change in temperature (ΔT), causes in-plane stresses σ_1 and σ_2 to be induced in the adherend layers at a distance x from the free end.

Now, consider the equilibrium of a differential element, length dx, as shown in Figure 2. Equilibrium for the center adherend (Figure 2b) is given by:

$$t_2 b\left(\sigma_2 + d\sigma_2\right) - t_2 b\left(\sigma_2\right) + \tau b dx = 0$$

$$\frac{d\sigma_2}{dx} = -\frac{\tau}{t_2} \tag{1}$$

Similarly for the outer adherend (Figure 2a):

$$\frac{d\sigma_1}{dx} = \frac{\tau}{t_1} \tag{2}$$

This implies that the stress in the layers varies linearly from zero at the free edge to the far-field stress over a slip length, ℓ. The slip length, and the relationship to the temperature change, can be obtained by consideration of the stresses and deformations in the far field, i.e., in the center of the joint, where the strains in the adherend layers are equal.

From compatibility:

$$\varepsilon_1 = \varepsilon_2 \tag{3}$$

From the thermoelastic constitutive behavior of the adherends:

$$\frac{\sigma_1}{E_1} + \alpha_1 \Delta T = \frac{\sigma_2}{E_2} + \alpha_2 \Delta T \tag{4}$$

From equilibrium:

$$\sigma_1 t_1 b + \sigma_2 t_2 b = 0$$

$$\sigma_2 = -\sigma_1 \frac{t_1}{t_2} \tag{5}$$

substituting (3) and(4) into (5) produces:

$$\sigma_1 = \frac{(\alpha_2 - \alpha_1)\Delta T}{\left(\frac{1}{E_1} + \frac{t_1}{E_2 t_2}\right)} \tag{6a}$$

and

$$\sigma_2 = -\frac{t_1}{t_2}\frac{(\alpha_2 - \alpha_1)\Delta T}{\left(\frac{1}{E_1} + \frac{t_1}{E_2 t_2}\right)} \tag{6b}$$

Integration of equation 1 or 2 and substitution for the boundary condition of equation 6 for the far-field stress results in the slip length:

$$\ell = \frac{t_1}{\tau}\frac{(\alpha_2 - \alpha_1)\Delta T}{\left(\frac{1}{E_1} + \frac{t_1}{E_2 t_2}\right)} \tag{7}$$

The resulting variation of stress in the adherends is shown schematically in Figure 3.

The average shear strain in the solder at a distance, x, from the edge is given by the difference in displacements of the adherends at that location, as shown in Figure 5. i.e:

$$\gamma = \frac{\delta}{h} = \frac{u_2(x) - u_1(x)}{h} \tag{8}$$

The displacements can be obtained by integrating the strain in the adherends. The maximum shear strain occurs at the free edge hence:

$$\Delta\gamma_{\max} = \frac{1}{h}\int_0^{\ell}\left(\varepsilon_2(x) - \varepsilon_1(x)\right)dx \tag{9}$$

After integration and substitution, the maximum shear strain occurring in the solder joint is given by:

$$\Delta\gamma_{\max} = \frac{\left(\alpha_2 - \alpha_1\right)^2 \Delta T^2}{2h\tau}\left(\frac{E_1 t_1 E_2 t_2}{E_1 t_1 + E_2 t_2}\right) \tag{10}$$

An analogous shear lag analysis can be performed for piezo-induced strains, due to an applied voltage across the adherends, as shown in Figure 6 (see also Appendix E). In this case, the constitutive behavior of the adherend materials is given by:

$$\frac{\sigma_1}{E_1} + \vec{E}_1 d_{31,1} = \frac{\sigma_2}{E_2} + \vec{E}_2 d_{31,2} \tag{11}$$

Where $\vec{E}$ is the applied electric field ($\Delta V/t$) and $d_{31,1}$ is the piezoelectric coupling coefficient between a field applied across the thickness of a piezoceramic and the strain induced in-plane. For a constant adherend thickness and uniform applied electric field, this reduces to:

$$\sigma_1 = \frac{\left(\vec{E}_2 d_{31,2} - \vec{E}_1 d_{31,1}\right)}{\left(\frac{1}{E_1} + \frac{t_1}{E_2 t_2}\right)} \tag{12a}$$

$$\sigma_2 = -\frac{\left(\vec{E}_2 d_{31,2} - \vec{E}_1 d_{31,1}\right)\frac{t_1}{t_2}}{\left(\frac{1}{E_1} + \frac{t_1}{E_2 t_2}\right)} \tag{12b}$$

By proceeding through the same analysis, but replacing equation 4 with equation 11 as given in equations 1-7, the maximum shear strain in the solder is given by :

$$\Delta\gamma_{\max} = \frac{1}{2h\tau}\left(\vec{E}_1 d_{31,1} + \vec{E}_2 d_{31,2}\right)^2\left(\frac{E_1 t_1 E_2 t_2}{E_1 t_1 + E_2 t_2}\right) \tag{13}$$

Strain-Based Approach: Coffin-Manson Prediction

The well-known Coffin-Manson equation assumes that the inelastic strain range is the governing parameter for low cycle fatigue. This analysis has previously been used to predict the lifetime of solder subjected to shear-strain-dominated deformation.[9,10] Generally, the Coffin-Manson relationship is expressed as:

$$\frac{\Delta\gamma}{2} = \gamma_f \left(2N_f\right)^c \tag{14}$$

where $\Delta\gamma$ is the plastic shear strain amplitude determined from the aforementioned shear lag analysis, N_f is the number of cycles to failure (initiation based failure criteria), γ_f and c are empirically determined material constants. In combination with equations 10 and 13, this provides a means to interpret and compare thermal and voltage cycling data.

Fracture Mechanics Approach: Strain Energy Release Rate

Various researchers have shown that a fracture mechanics approach in conjunction with a "Paris law" can be applied to describe the growth of damage in solder joints[11] and monolithic specimens of solder.[12] For a lap joint, cracks growing in the solder joints under thermal or piezo loading reach a steady state in which the strain energy release rate does not depend on the crack length once they have grown more than a few times the adherend layer thickness in extent. This simplifies analysis since the complex stress state at the crack tip does not have to be directly considered. As a further simplification, the contribution of the solder layers to the strain energy release rate will also be ignored.

The strain energy available for the advancement of the crack is calculated by considering control volumes with length *da* far ahead and behind the crack tip. The difference in strain energy between the control volumes is equivalent to advancing the crack by a distance *da*[13] (see Figure 10). In the particular case of a double lap joint, there are two possible crack configurations; cracks either grow simultaneously in both solder joints, or only in one of the joints. In the former case, the material in the wake of the crack tip is stress free, whereas in the latter case, the pair of adherends that remain joined acts as a bimaterial strip and is not stress free. The asymmetric single cracking case was usually observed experimentally.

Symmetric Double Fracture:

Since material in the wake of the crack tip is stress free, all the stored strain energy in the three layer stack is available to propagate the crack. The stresses in the two layers are given by the compatibility, equilibrium, and constitutive considerations of equations 4-6. The stresses in layers 1 and 2 are:

$$\sigma_1 = d_{31}\frac{E}{t}\left(\Delta V_1 + \Delta V_2\right) \tag{15}$$

Since the stresses are uniform through the layer thicknesses, the strain energy stored in length *da* is given by:

$$U = \frac{\varepsilon_p^2 t_1 E_1}{2 + \lambda\xi} \tag{16}$$

Where for the piezo case: $\varepsilon_p = \frac{d_{31}}{t}\left(\Delta V_1 + \Delta V_2\right)$, and for the thermal case $\varepsilon_p = \left(\alpha_1 - \alpha_2\right)\Delta T$, $\xi = \frac{t_1}{t_2}$, $\lambda = \frac{E_1}{E_2}$.

From the definition of strain energy release rate, $G = dU/da$, thus the strain energy release rate is simply:

$$G = \frac{3}{2} d_{31}^2 \frac{E}{t}\left(\Delta V_1 + \Delta V_2\right)^2 \tag{17}$$

Single joint fracture:

The procedure for calculating *G*, for this case is similar for the double crack case given above except that the strain energy associated with the intact bond in the crack wake must be taken into account. This is shown schematically in Figure 11.

The total strain energy release rate is given by:

$$G = \frac{U_A - \left(U_B + U_C\right)}{w\,da} \tag{18}$$

The strain energy for region A is given by equation 17, above.

$$U_A = \frac{3}{2} d_{31}^2 \frac{E}{t}\left(\Delta V_1 + \Delta V_2\right)^2 \tag{19}$$

Region B is stress free, therefore $U_B = 0$.

$$U = \int \frac{\sigma^2}{2E} tb\, da \tag{20}$$

Region C requires the evaluation of the strain energy in a bilayer, bimaterial strip. This is obtained by enforcing considerations of equilibrium of forces and bending moments and the compatibility of strains and curvatures in the two layers (Spearing, 1996). Hence:

$$U_C = \frac{\beta^2 \xi^2 t_1 \left(\lambda\xi^2 + 1\right)}{2E_1}\left[\xi^2\left(\lambda\xi + 1\right)\left(\lambda\xi^3 + 1\right) + 3\lambda\xi^3\left(\xi + 1\right)^2\right] \tag{21}$$

where

$$\beta = \frac{\varepsilon_p E_1}{\xi\left(\lambda\xi^3 + 1\right)\left(\lambda\xi + 1\right) + 3\lambda\xi^2\left(\xi + 1\right)^2}\ ,\ \varepsilon_p = \frac{d_{31}}{t}\left(\Delta V_1 + \Delta V_2\right)\ ,\ \xi = \frac{t_1}{t_2}\ ,$$

$$\text{and } \lambda = \frac{E_1}{E_2}$$

In the case corresponding to the experiments in which the piezoceramic substrates are made of the same material with the same thickness, $\lambda = \frac{E_1}{E_2} = 1$, $\xi = 1$

This simplifies to:

$$\Delta G = \frac{13}{48}\frac{E}{t} d_{31}^2 \left(\Delta V_1 + \Delta V_2\right)^2 \tag{22}$$

3. Experimental

Specimen Manufacture

Test specimens consisted of three substrates of 0.19 mm thick lead-zirconate-titanate (PZT) 5H (PiezoSystems, Inc.). The substrates were supplied cut to size, with widths of 6.35 mm and lengths of 31.75 mm for the outer pieces and 38.10 mm for the central pieces. The longer length of the central pieces facilitated access to the center piezo-ceramic for electrical connections (Figure 8). The substrates were bonded with 25.4 μm thick eutectic lead (37

wt%)-tin (63 wt%) solder preform (Indium Corporation). The piezo-ceramic substrates were supplied coated with a 5000 Å gold layer over an electroless nickel-plated metallization to promote wetting of the solder.[14] The joints were made by a standard (proprietary) solder reflow process in a reducing atmosphere, which was performed in a batch furnace for the first batch of specimens and in a belt furnace for subsequent batches. A polished tri-layer specimen is shown in Figure 9. Compositional analysis of the solder revealed significant diffusion of the gold adhesion layer into the solder. Figure 10 shows a scanning electron microscope (SEM) micrograph of a polished cross section of the solder indicating the presence of three distinct phases. Electron dispersive spectroscopy revealed the presence of the expected Pb-rich and Sn-rich phases of the lead-tin eutectic, but also a tin-gold phase containing approximately 4 at% gold.

The material properties required for modeling were obtained from the suppliers' data sheets, except for the piezo strain coefficients, which were measured using a laser extensometer after poling. The Young's modulus, E, of PZT-5H is 60 GPa, the piezo-strain coefficient, d_{31}, is -320×10^{-12} m/W, and the shear yield stress of the solder is assumed to be 37 MPa, based on the solder manufacturer's data sheets. See Appendix B for details on specimen manufacture.

Testing

Testing requires the outer two piezo layers to be actuated 180° out-of-phase from the center piezo (Figure 11). This requires separate connections to be made to both surfaces of all three piezo ceramic substrates. A specimen holder with flexible copper fingers (Figure 12) was designed to achieve this without the need for additional soldering of leads. Since piezoelectric materials have a preferred actuation direction determined by poling (orienting the dipoles in the ceramic), a DC offset is required to prevent de-poling when actuated in the opposite direction. A constant 100 V DC offset was used for all specimens and the AC component of the voltage was cycled about this offset. The utilization of a DC offset allowed use of the piezo-ceramic's maximum actuation range. An H-bridge voltage cycling circuit was used to achieve these applied voltages. See Appendix C for details on the design and construction of the circuit.

Piezo-induced fatigue experiments were performed in which voltage amplitude, frequency, and temperature were varied. Voltage, which controls the amount of shear strain applied to the solder, was varied from $100\,V_{DC} \pm 90\,V_{AC}$ to $100\,V_{DC} \pm 200\,V_{AC}$. The effects of three frequencies, 0.5 Hz, 1 Hz, and 5 Hz, were characterized. Tests were also performed at 25°C, 80°C, and 0°C, for several voltage levels at a fixed frequency of 1 Hz.

Crack growth rate and crack opening displacement were monitored *in situ* using a high resolution long-working distance microscope mounted on a motor-driven calibrated X-Y stage. This system provided a resolution of 10 μm on damage observations and crack length measurements. When acquiring data, the cycling frequency was reduced to 0.01 Hz, so that an accurate measurement of crack opening displacement and crack length could be made.

Thermal testing (0°C, 25°C and 80°C) was performed using a thermoelectric heating/cooling system utilizing Peltier junctions. A small fan inside the chamber provided convection to assure a uniform temperature, which was manually monitored. Temperature was controlled to better than ±3 °C during the conduct of each test. A transparent plastic window allowed *in situ* crack growth measurements during the thermal testing. See Appendix D for details regarding testing procedures.

4. Results

In situ observations of specimens during voltage cycling revealed that the primary failure mechanism was the initiation and growth of fatigue cracks in the solder joints. Such cracks invariably initiated at voids, debonded regions, or other defects in the solder (see Figure 13a). Although not quantified in the present study, the presence of such defects in the solder correlated with a greatly reduced number of cycles to crack initiation. Figure 13b shows the fracture surface of a failed specimen. Multiple cracks, originating at different defects in the same joint, were often observed; however, once one of the cracks reached the free end of the specimen, this crack would dominate over the other smaller cracks. This behavior is consistent with previous observations.[7] As shown in Figure 18, the growth of such primary cracks away from the free ends of the specimen was observed to occur at an approximately constant rate; however, their growth was measurably accelerated by interactions with voids and pre-existing small cracks. In some specimens, the coalescence of short cracks and voids to form a primary crack was observable as a distinct phase of the failure process. In others, the primary crack appeared to form over a very short number of cycles, as was the case for the specimen observed in Figure 14. In most specimens, the steady-state growth of a single primary crack was observed to occupy a significant portion of the fatigue life.

The cracks generally initiated within the solder material, and the initial phase of growth was also generally confined to a cohesive mode. However, subsequent growth would often occur in an adhesive mode at the interface between the solder and the substrate surface or oscillate between cohesive and adhesive fracture. The overall rate was not significantly affected by the

mode of growth. The data in Figure 18 contains regions of both cohesive and adhesive fracture.

It was possible to measure directly the crack opening displacement using the micrometer stage on the microscope. A crack opening from the free end of a specimen can be seen in Figure 15. A typical plot of crack opening displacement versus number of cycles is shown in Figure 16. The trend in crack opening displacement as a function of cycles is consistent with the crack growth behavior.

Data was recorded for the number of cycles to initiate fatigue damage. To circumvent uncertainties in identifying precisely when and where damage first initiated, an arbitrary crack length of 2 mm was defined as constituting damage initiation. Using this criterion, the data presented in Figure 17a was obtained. The applied voltage was converted to a cyclic shear strain using equation 13 with an assumed shear strength of 37 MPa. Figure 17b shows the data for the total number of cycles to failure, i.e. the point at which the specimen could no longer actuate as intended.

Figure 18 shows reduced data for steady state crack growth rates as a function of applied strain energy release rate from equation 22. At higher strain energy release rates, the data for tests conducted at different frequencies converge to a monotonic dependence of growth rate on strain energy release rate. However, at lower strain energy release rates, the data sets diverge. Tests conducted at lower frequencies exhibit higher growth rates for a given applied strain energy release rate than those cycled at higher frequencies. At the higher strain energy release rates, a "Paris Law" relationship appears to hold. There is some indication of a threshold strain energy release rate that is frequency dependent.

Figure 19 shows the effect of temperature on the steady state crack growth rate at various strain levels. There is nearly an order of magnitude increase in the crack growth rate at a given nominal strain energy release rate at 25°C compared to 0°C. However, the crack growth rates at 80°C are lower than those at 25°C. See Appendix E for details on how data analysis was performed and Appendix F for a listing of all data sets. Tables I through III list a summary of crack growth rate results for the three testing temperatures.

5. Discussion

The results presented in the previous section demonstrate the capability of using piezo-mechanical cycling to cause fatigue in solder lap joints. The stress and deformation levels are similar to those that would be achieved in conventional thermal cycling of joints between adherends with different thermal expansion coefficients. This opens the possibility of using this method as a research tool for exploring the mechanisms of the thermo-mechanical fatigue of solder joints and for performing accelerated tests. It remains to be established whether the degradation mechanisms and number of cycles to failure correlate with data obtained from thermal cycling tests.

The data obtained for crack initiation, shown in Figure 17a, can be fitted with a Coffin-Manson relationship in which the exponent is -0.23 and the pre-factor is 3.34×10^{-2}. This compares with corresponding values of –0.54 and 1.13 found by Lau[8] conducting mechanical fatigue tests on eutectic lead-tin solders. The difference may be explained by the embrittlement of the solder by the inclusion of the gold. It is also significant that the data for fatigue crack initiation and total life is very scattered. This can be attributed to the observation that damage initiates preferentially at voids and other defects. There was considerable variation in the area fraction of voids and their spatial distribution over the joint area from specimen to specimen. These observations suggest that the elimination of defects from the solder joint is a key to achieving a high level of reliability. They also suggest that using an empirical relationship, such as the Coffin-Manson equation should be accompanied by careful characterization of the joint microstructure. It is interesting to note that there is not a clear correlation between the test frequency and the number of cycles to initiate damage. This is somewhat surprising, since at slower loading rates, creep effects would be expected to result in a greater accumulation of inelastic strain, therefore resulting in early damage initiation. It is possible that if such an effect were present, its influence would be obscured by the scatter in the data due to specimen to specimen variations in joint microstructure.

The crack growth rate data is considerably less scattered than the crack initiation data. This is to be expected since the time to initiate damage depends on the local microstructure of the solder, whereas steady state crack growth rates depend on the average response of the joint, which is expected to be less subject to variation. The crack growth rate approximately conforms to a Paris Law at higher cyclic strain energy release rates. It is interesting to note that the slope of the Paris law and the crack growth rates for the piezo-mechanical loading of joints in this study are significantly greater than those observed in fatigue tests conducted on compact

tension specimens of eutectic solder.[12] This discrepancy can be ascribed to the influence of the constraint imposed by the joint configuration, the differences in microstructure, gold absorption into the solder and the presence of voids, which may not be present in monolithic solder specimens. This discrepancy illustrates the need to conduct testing of solders in configurations as close to the service environment as possible.[15] These experimental observations also suggest that, given the scatter in times to initiate damage, calculations based on the time for cracks to grow to a significant length, may offer a robust, conservative approach to life prediction.

The influence of test frequency on crack growth rates is an important observation. It confirms the role of plastic and viscous behavior in the fatigue crack propagation process. At lower frequencies, there is more time for irreversible deformation to occur at the crack tip, resulting in a greater increment of crack growth per cycle. The results are consistent with those of Logsdon et al[12], who observed similar increases in cyclic growth rates at frequencies below 2 Hz on monolithic solder specimens.

The temperature data is unexpected. It is to be expected that decreasing the temperature would reduce the cyclic crack growth rate because it reduces the extent of the creeping plastic zone at the crack tip. This was observed between 0°C and 25°C. However, upon increasing the temperature further, the rate *decreased.* This may indicate that there is a transition in damage mechanisms between 25°C and 80°C, particularly the role of creep deformations at the crack tip. This observation requires further examination and verification.

The work presented here raises the possibility that the failure of joints by piezo-mechanical loading may be a concern for the long-term reliability of systems containing active elements. Preliminary work has shown that polymer adhesive joints are also liable to undergo fatigue failure via piezo-mechanical loading. As single crystal piezo-ceramics that allow higher actuation strains are developed, the durability of the adhesive joints used to bond them together into stacks or to attach them to structural elements for vibration and noise control may become a limiting issue.

The analysis and experimental results presented here confirm the potential for using the analogue of piezo-mechanical loading to thermo-elastic loading of solder joints to better understand the mechanisms of failure. However, considerable work is still required to establish the usefulness of the analogue as a means of performing accelerated testing and of separating the influence of different factors on lifetime.

6. Conclusions

The capability to cause fatigue failure in solder lap joints by piezo-mechanical loading has been demonstrated. Analysis shows that the solutions for the free edge strain levels and cyclic strain energy release rates for crack growth achievable by piezo-mechanical loading are analogous to those expected to be induced by thermo-mechanical loading. The double lap joint configuration introduced in this article and the associated circuitry for voltage cycling has been shown to be a straightforward means of achieving this capability. For the tests described in this work, the life of these joints can be divided into two distinct regimes: crack initiation and steady state crack growth. Damage initiation depends strongly on the presence of voids and other defects in the joint, and as a result, the number of cycles to initiate damage was quite scattered. In the growth phase there was less scatter. At higher applied voltages, data conformed to a Paris type relationship of crack growth rate on strain energy release rate amplitude. At lower voltages, there was evidence of a threshold strain energy release rate, and frequency was observed to have an increased effect. Low-frequency loading resulted in higher cyclic growth rates. Overall this test technique has great potential for allowing a rational investigation of the factors contributing to the thermomechanical fatigue and reliability of solder and other adhesive joints.

7. Future Work

Possibilities for future work include a full battery of temperature tests, fully characterizing this effect and how it relates to creep in the solder. A further study could be performed on the metallization layer on the piezoceramic, selecting a different manufacturing technique to reduce the solder's impurities. Another interest would be to test other active materials and to explore their actuating and bonding capabilities. Testing other actuator materials could produce insight directly impacting the burgeoning active material industry. Another potential application is to automate the testing technique by using interferometry, changes in curvature, etc. instead of visual crack inspection. This would reduce human error as well as further reduce manufacturers' testing costs. Finally, one could apply this piezo-induced technique to other adhesives, such as epoxy or other compositions of solders. Apart from further experimental studies, it is necessary to validate the shear lag model by performing finite element analysis and *in situ* strain mapping.

8. References

1. Solomon, H.D. "Predicting Thermal and Mechanical Fatigue Lives of Soldered Joints from Isothermal Low Cycle data." *Solder Joint Reliability.* Ed: J.H.Lau. New York, NY: Van Nostrand Reinhold, 1991, pp. 406-454.

2. Hwang, J.S. *Modern Solder Technology for Competitive Electronics Manufacturing.* New York: McGraw-Hill, 1996.

3. Markstein, H.W. "Are Surface Mount Technology Solder Joints Reliable?" *Electronic Packaging and Production.* **29** (2), 1989, pp. 66-69.

4. Krinke, T.A. and D.K. Pai. "Factors Affecting Thermal Fatigue Life of Leadless Ceramic Chip Carrier Solder Joints." *Welding Journal.* **67**, 1988, pp. 33-40.

5. Xie, D.J., Chan, Y.C., Lai, J.K.L., Hui, I.K. "Fatigue life estimation of surface mount solder joints." *IEEE Transactions on Components, Packaging, and Manufacturing Technology, Part B: Advanced Packaging.* **19**, 1996, 669-678.

6. Engelmaier, W. "Surface Mount Solder Joint Long-term Reliability: Design, Testing, and Prediction." *Soldering and Surface Mount Technology.* **1**, 1989, pp. 14-22.

7. Kaminishi, K., M. Iino, M Taneda, "Fatigue Life Prediction of Microelectronics Solder Joints." *Experimental Mechanics vol. 2 - Advances in Design, Testing, and Analysis, I.M. Allison, ed.* A.A.Balkema/Rotterdam/Brookfield, 1998, pp. 975-980.

8. Lau, J. H. *Solder Joint Reliability: Theory and Applications.* New York: Van Nostrand Reinhold, 1991.

9. Coffin, L.F. "A Study of the Effects of Cyclic Thermal Stresses on a Ductile Metal." *Transactions of the ASME.* **76**, 1954, pp. 931-950.

10. Manson, S.S. "Behavior of Materials under Conditions of Thermal Stress." *NACA Report 1170.* 1954.

11. Pao, Y-H. "A Fracture Mechanics Approach to Thermal Fatigue Life Prediction of Solder Joints." *IEEE Transactions on Components, Hybrids, and Manufacturing Technology.* **15** (4) 1992, pp. 559-570.

12. Logsdon, W.A., P.K. Liaw, and M.A. Burke. "Fracture Behavior of 63Sn-37Pb Solder." *Engineering Fracture Mechanics.* **36** (2), 1990, pp. 183-218.

13. Spearing, S. M., "Design Diagrams for Reliable Layered Materials," *AIAA Journal.* **35** (10), 1997, pp. 1638-1644.

14. Jacobson, D.M. and G. Humpston, G. "Gold Coatings for Fluxless Soldering." *Gold Bulletin.* **22** (1), 1989, pp. 9-18.

15. Qian, Z. and S. Liu. "On the Life Prediction and Accelerated Testing of Solder Joints." EEP-Vol. 24, *Thermal-Mechanical Characterization of Evolving Packaging Materials and Structures, ASME,* 1998, pp. 1 -11.

9. Tables

Table I: Crack growth rate results at room temperature.

Frequency (Hz)	Voltage (V)	crack growth rate, da/dN (mm/cycle)	rsq	cycles to initiation
0.5	100V +/- 90V	6.81E-05	0.94875	27320
0.5	100V +/- 100V	3.01E-04	0.95824	48300
0.5	100V +/- 100V	3.98E-04	0.96926	62550
0.5	100V +/- 120V	1.43E-04	0.97132	27650
0.5	100V +/- 130V	3.65E-04	0.93288	10990
0.5	100V +/- 150V	6.78E-04	0.9476	270
0.5	100V +/- 150V	4.47E-04	0.98808	6630
0.5	100V +/- 160V	3.55E-03	0.90881	240
0.5	100V +/- 170V	3.77E-03	0.93827	2040
0.5	100V +/- 180V	3.28E-03	0.97288	900
1	100V +/- 130V	5.46E-05	0.94195	43400
1	100V +/- 140V	3.86E-04	0.94837	500
1	100V +/- 150V	1.51E-03	0.88906	730
1	100V +/- 160V	1.00E-03	0.93961	1000
1	100V +/- 175V	2.51E-03	0.87864	3290
1	100V +/- 190V	2.59E-03	0.96549	300
1	100V +/- 200V	6.49E-02	0.99521	330
5	100V +/- 170V	5.37E-04	0.95497	3030
5	100V +/- 180V	5.06E-03	0.95278	620
5	100V +/- 180V	2.51E-03	0.97514	1930
5	100V +/- 190V	2.54E-03	0.9703	1150
5	100V +/- 200V	2.91E-02	0.96673	1030

Table II: Crack growth rate results at 0°C.

Frequency (Hz)	Voltage (V)	crack growth rate, da/dN (mm/cycle)	rsq	cycles to initiation
1	100V +/- 160V	4.52E-04	0.99528	11160
1	100V +/- 180V	3.25E-04	0.98499	2250
1	100V +/- 200V	1.10E-03	0.96380	1920
1	100V +/- 200V	7.12E-04	0.99798	10940
1	100V +/- 220V	2.63E-03	0.89872	1920
1	100V +/- 220V	3.10E-03	0.91534	1440

Table III: Crack growth rate results at 80°C.

Frequency (Hz)	Voltage (V)	crack growth rate, da/dN (mm/cycle)	rsq	cycles to initiation
1	100V +/- 130V	2.37E-04	0.97487	2880
1	100V +/- 140V	5.75E-04	0.95498	5250
1	100V +/- 140V	8.02E-04	0.89272	25630
1	100V +/- 160V	1.20E-03	0.97967	7470
1	100V +/- 180V	6.89E-03	0.98459	8850
1	100V +/- 180V	1.04E-02	0.97048	7640

10. Figures

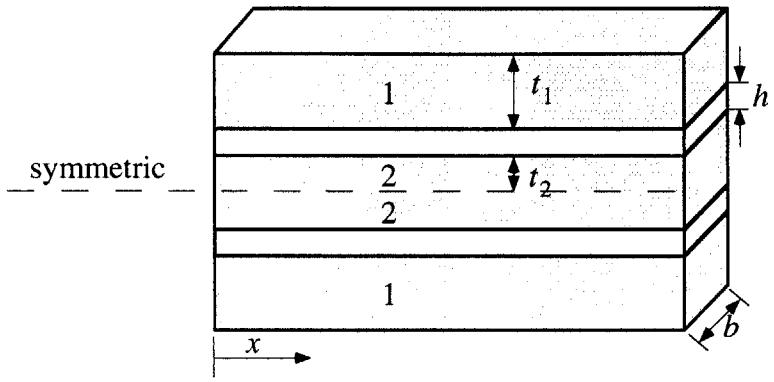

Figure 1: Double lap joint configuration where t_1, t_2 are the thicknesses of the top and center layers respectively, and b is the width of the layers.

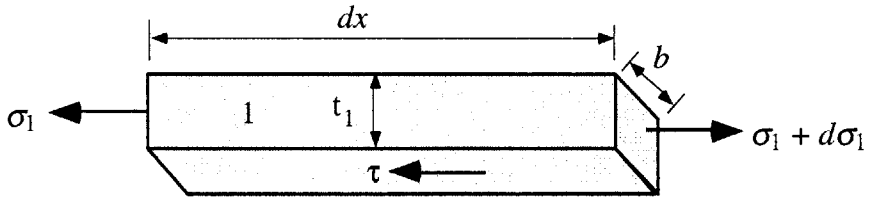

Figure 2a: Differential element of outer adherend layer.

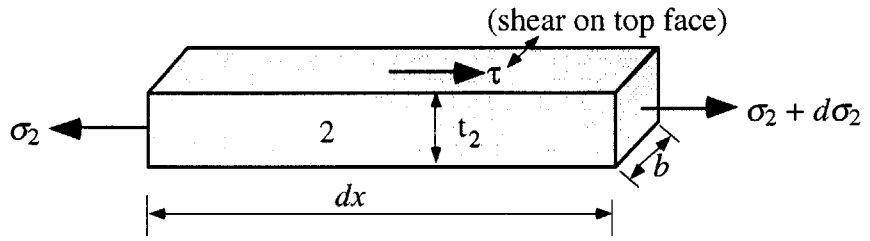

Figure 2b: Differential element of center adherend layer.

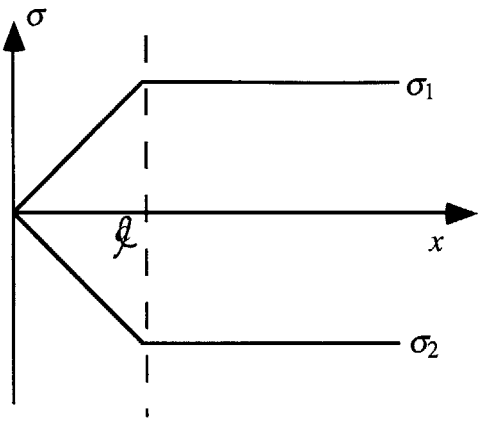

Figure 3: Variation of in-plane stress for inner and outer adherends from the free edge to the far field stress state.

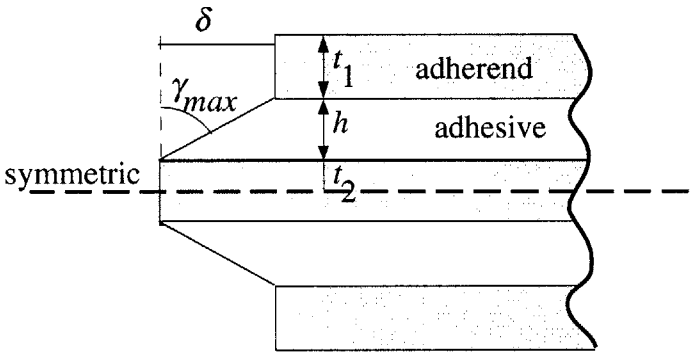

Figure 4: Shear strain in the solder layer.

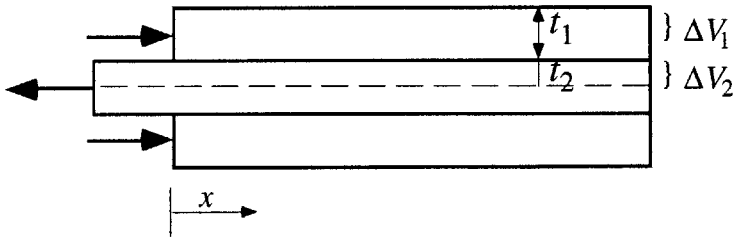

Figure 5: Shear lag analysis for out-of-phase piezo actuation.

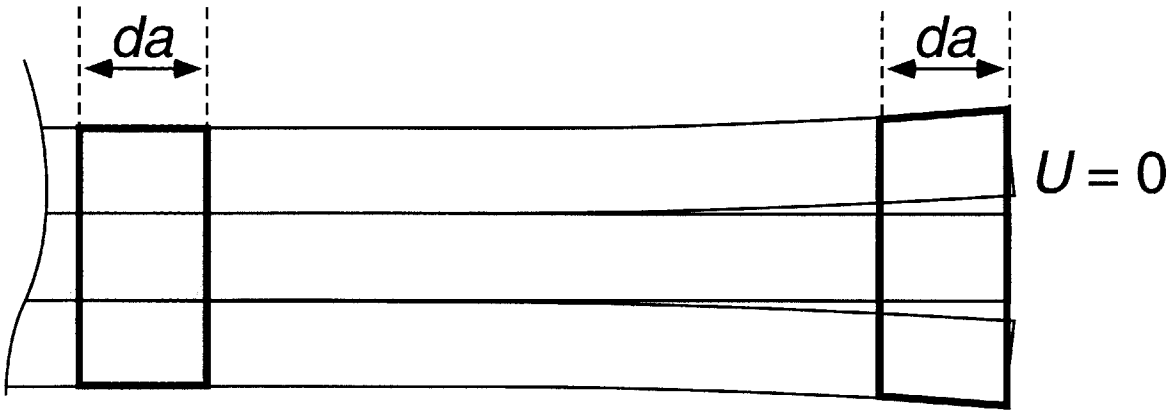

Figure 6: Control volumes ahead and behind the crack tip are used to calculate the strain energy available for crack propagation.

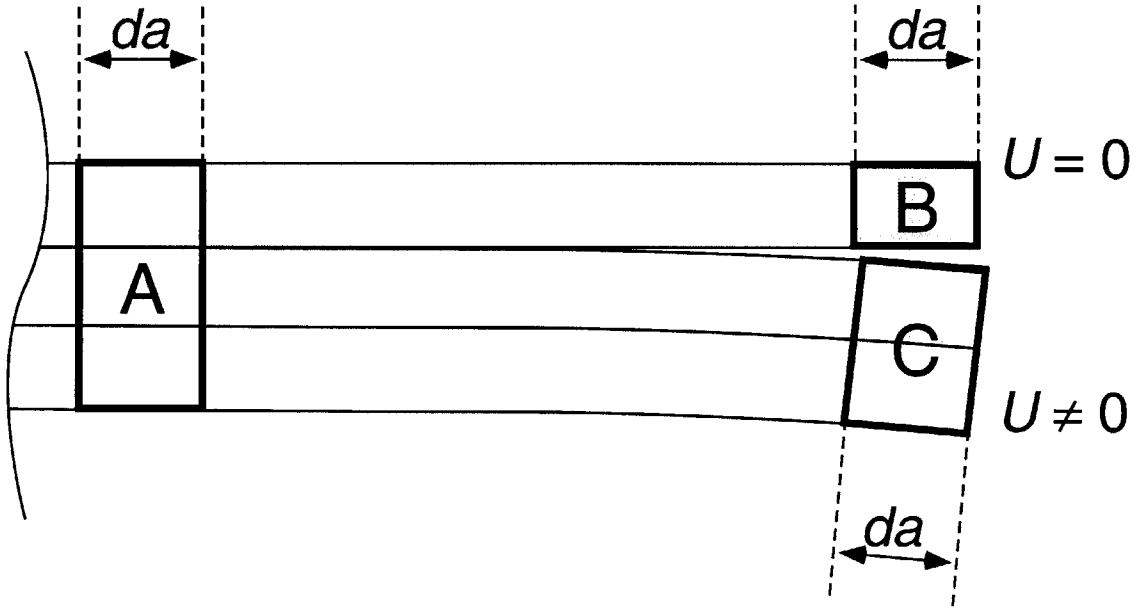

Figure 7: Cracking scenario for piezo/solder tri-layer stack. As the crack passes, the top layer is stress free, but there is still strain energy stored in the bottom two layers.

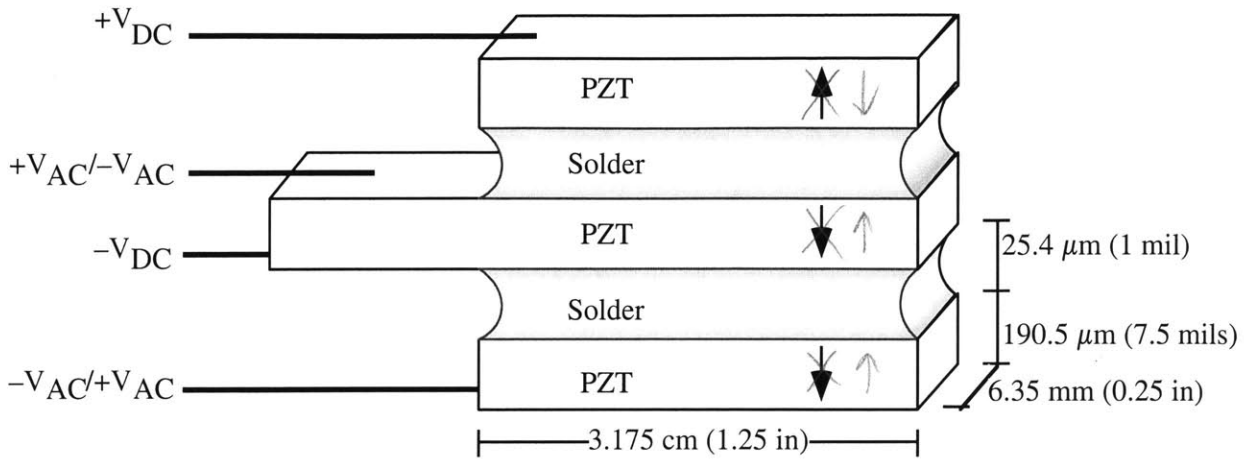

Figure 8: Schematic diagram of piezo/solder stack and applied voltages. The piezoceramic layers are actuated 180° out-of-phase to induce maximum shear in the solder and to eliminate bending.

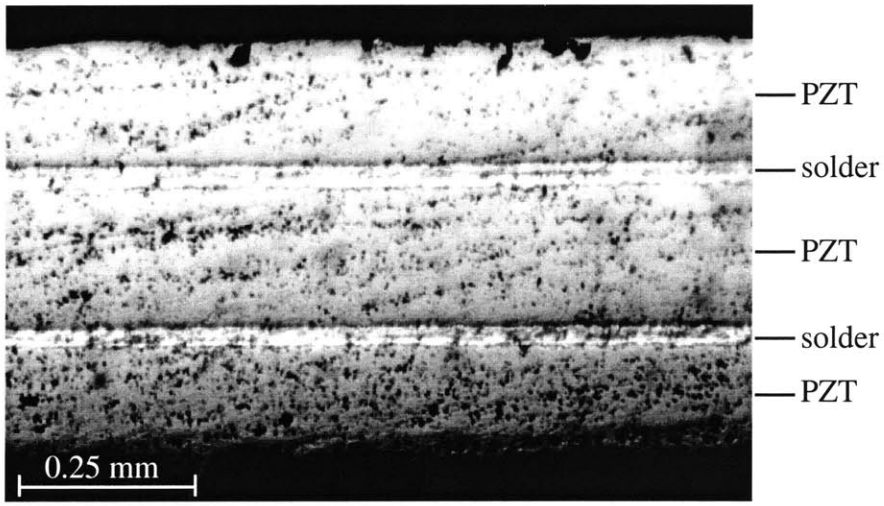

Figure 9: Polished cross edge of a test specimen. The dark marks on the solder and piezoceramic layers are embedded particles from polishing.

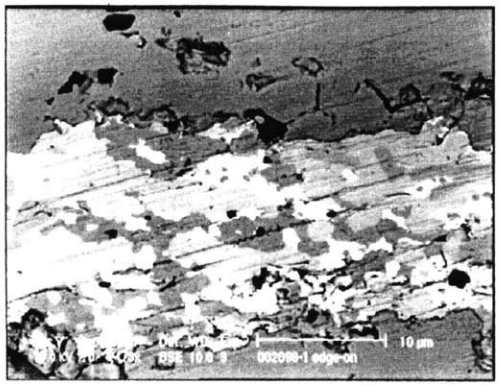

Figure 10: Compositional analysis of gold-embrittled solder. Bright regions: Pb-rich; Medium Gray Regions: Sn-Au; Dark Gray Regions: Sn-Rich

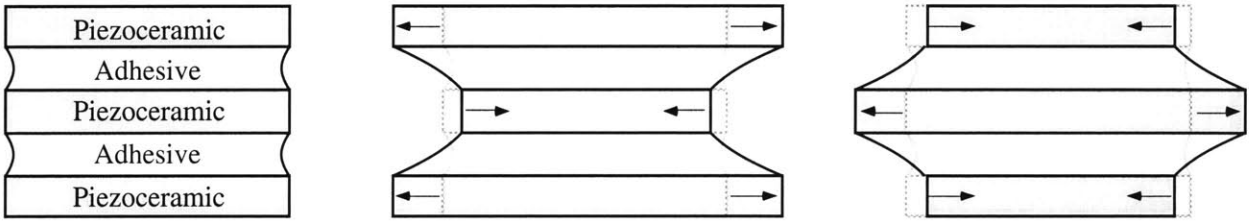

Figure 11: Out-of-Phase Actuation. State 1 (middle): center piezo contracts; outer piezos expands. State 2 (right): center piezo expands; outer piezos contract.

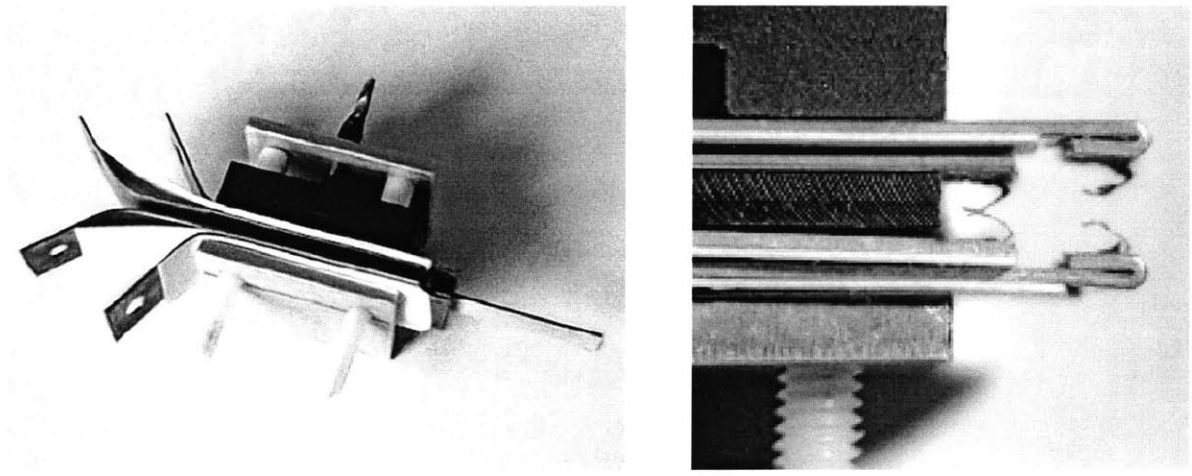

(a) (b)

Figure 12: Test specimen holder. Specimen holder constrains one end of specimen during testing and delivers the proper voltage to the appropriate layers. (a): specimen holder with specimen inserted. (b): Close-up of copper finger mechanism.

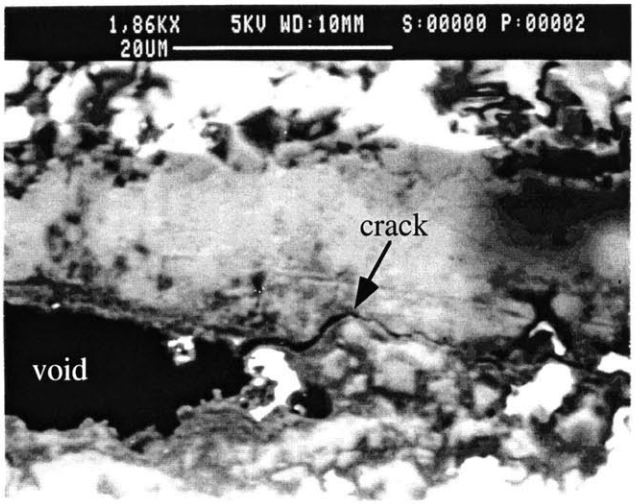

Figure 13a: A micro-crack initiating at a void in the solder joint.

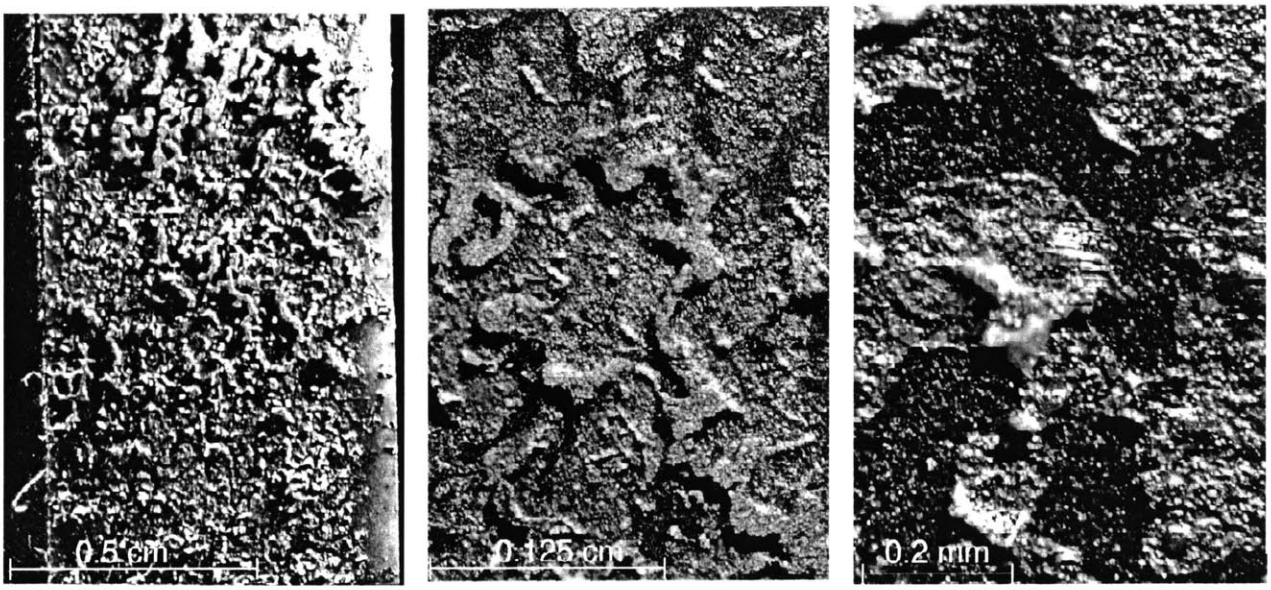

10X 38X 150X

Figure 13b: Fracture surface of a failure piezo/solder joint.

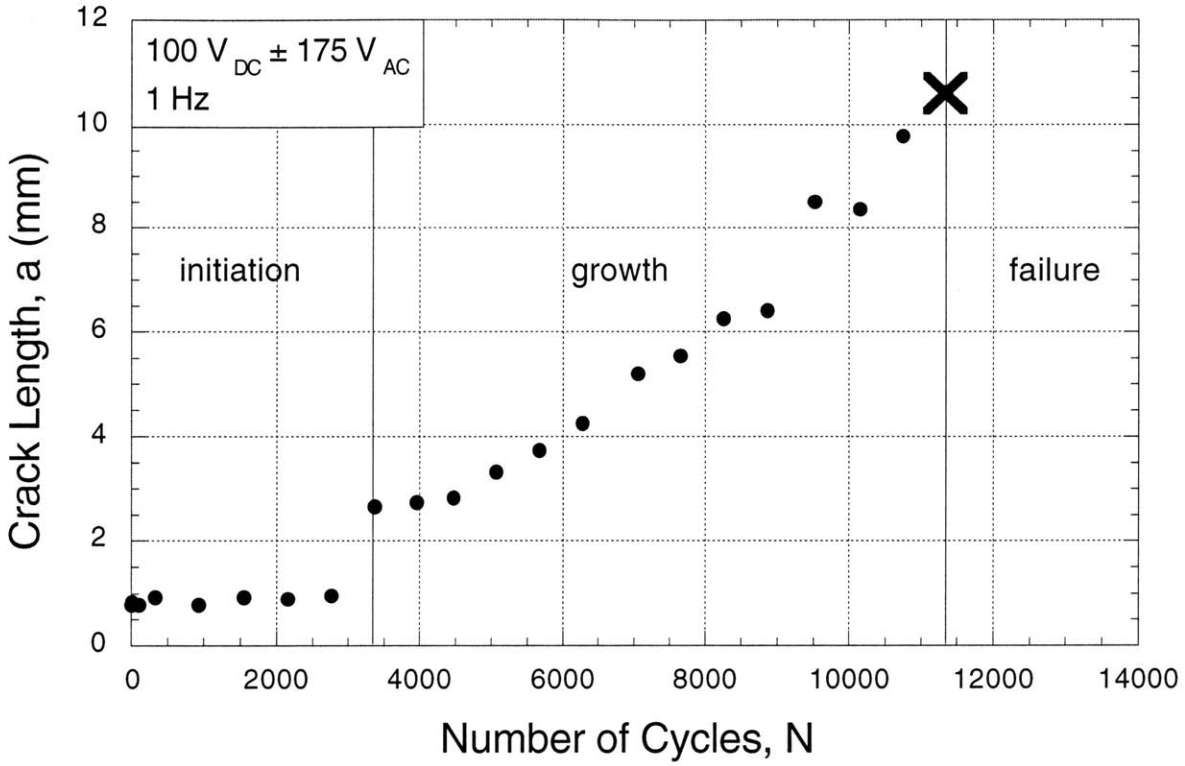

Figure 14: Crack length versus number of cycles for one particular voltage and frequency case.

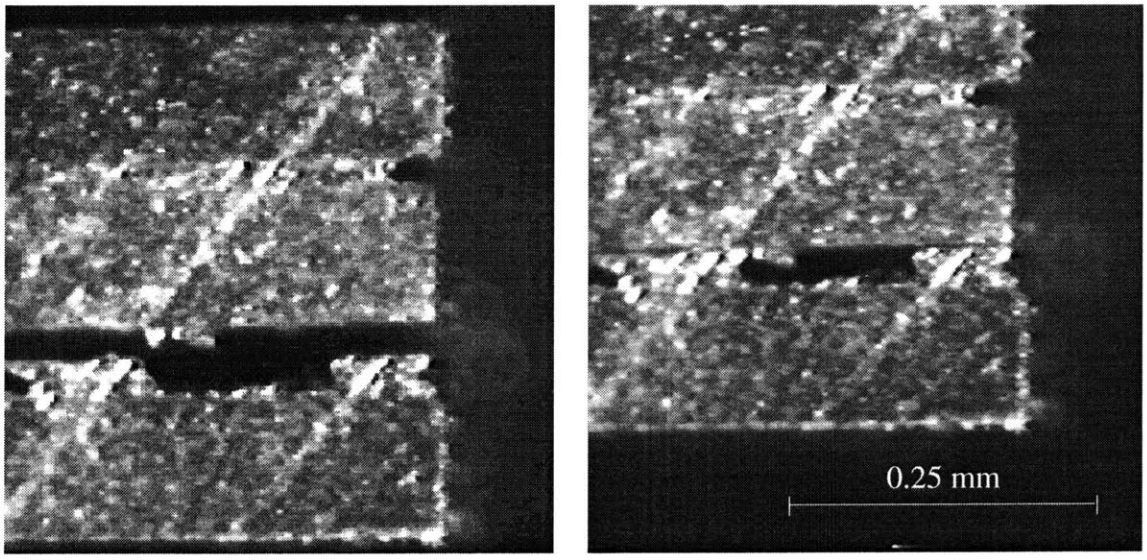

Figure 15: Crack opening displacement as measured for free end cracks (bottom joint in the figure). The left picture shows the crack in the open state; the right figure shows the crack in the closed state. The crack initiated from the void shown in the center of the picture.

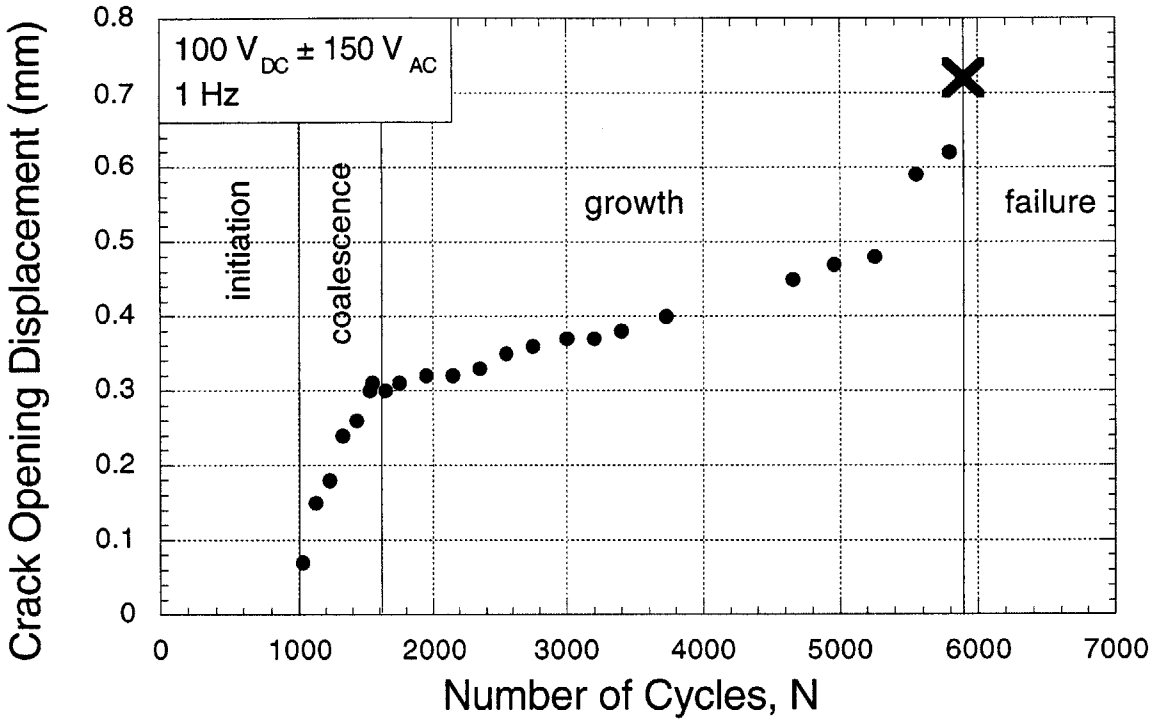

Figure 16: Crack opening displacement versus number of cycles. The curve is characterized by three distinct regions, initiation, coalescence, and growth before failure occurs.

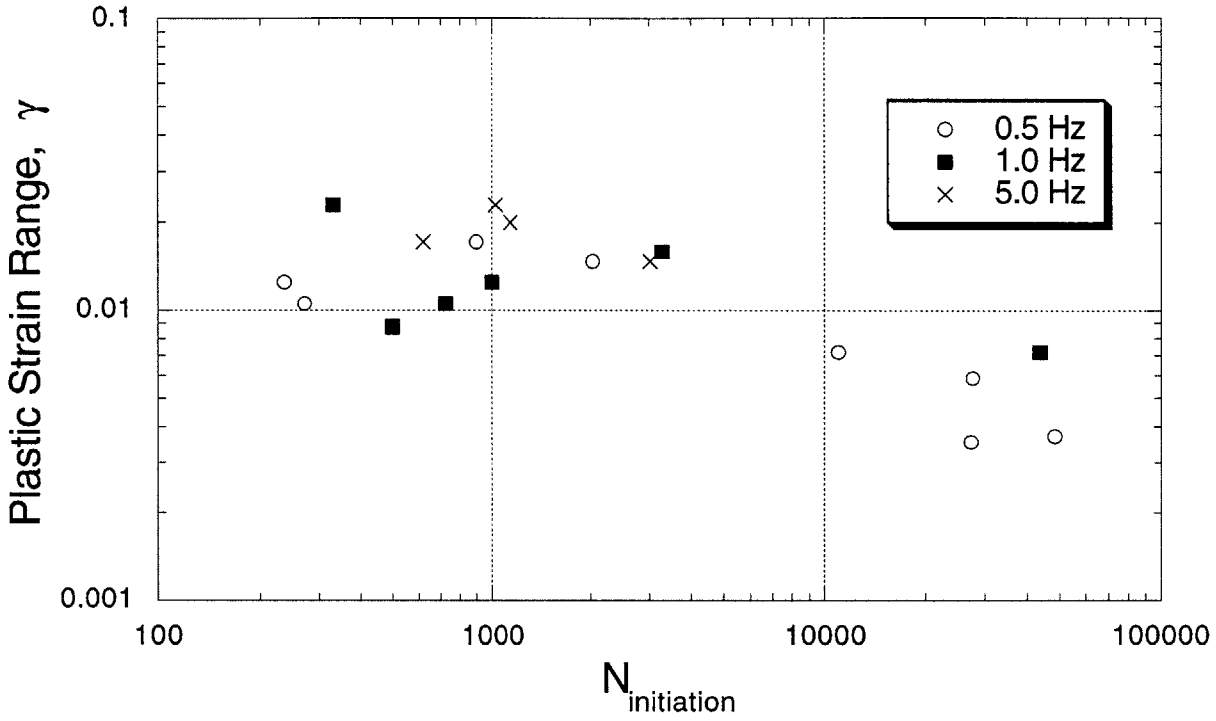

Figure 17a: Cycles to initiation (2 mm criteria). Shear strength of the solder is assumed to be 37 MPa.

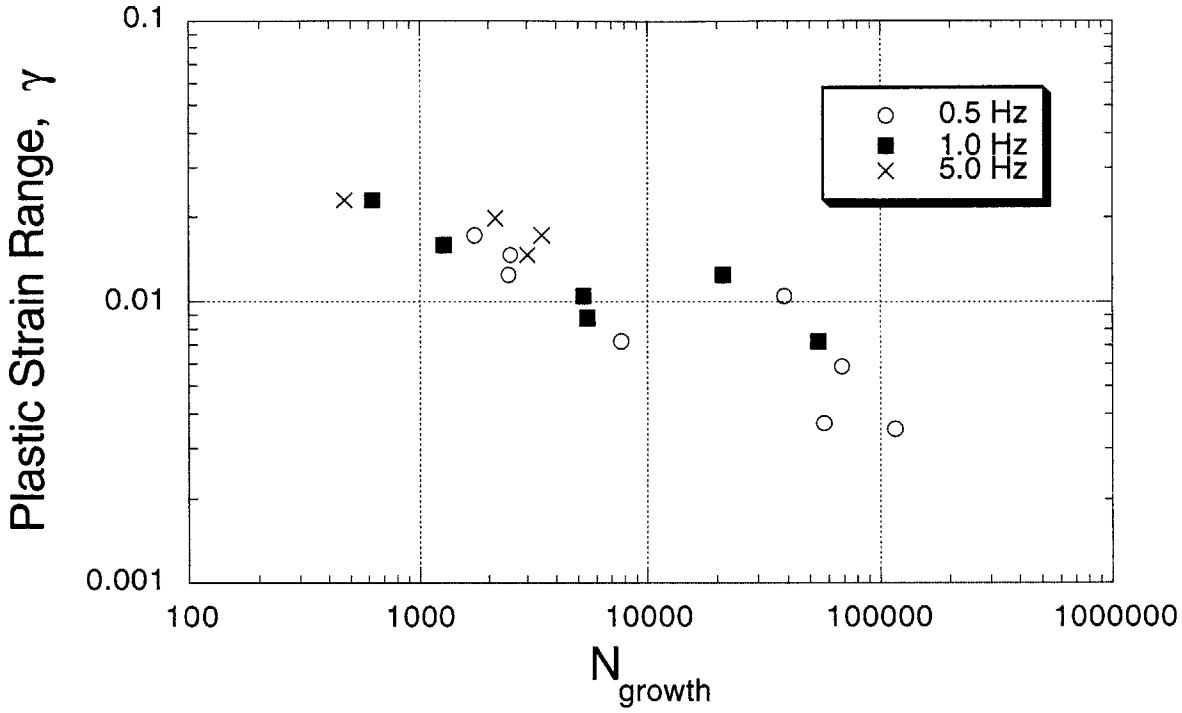

Figure 17b: Growth cycles (cycles to failure – cycles to initiation). Shear strength of the solder is assumed to be 37 MPa.

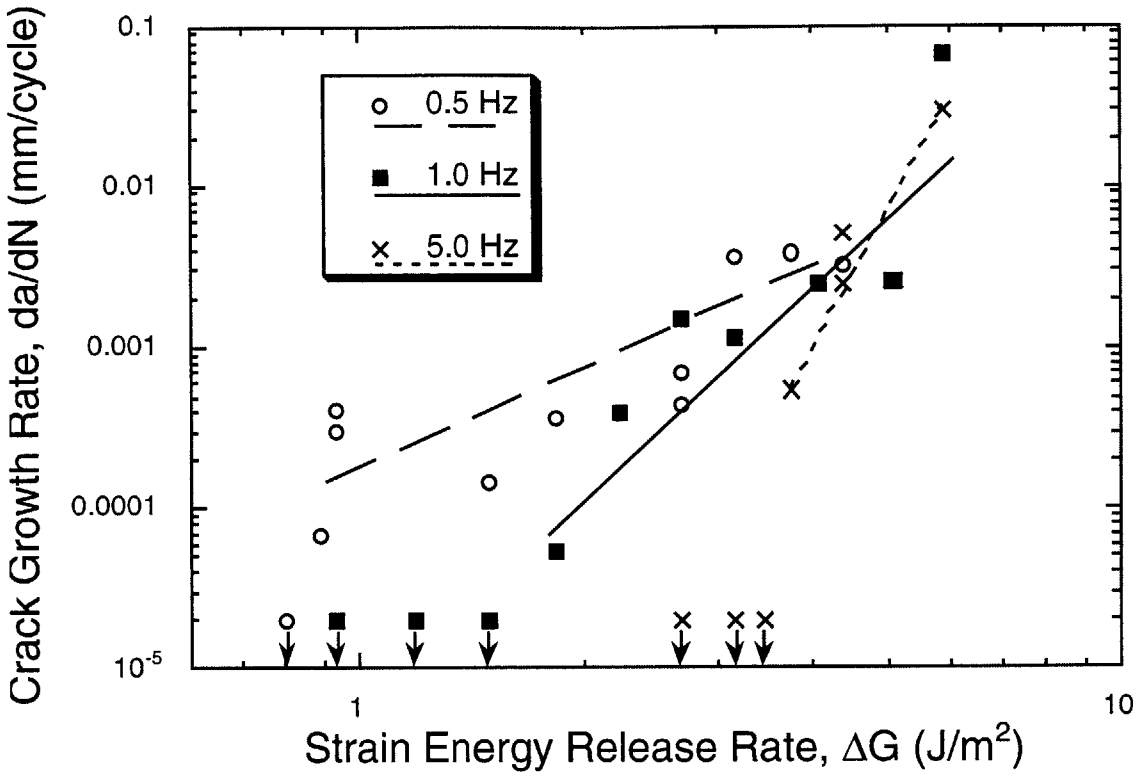

Figure 18: Crack growth rate versus strain energy release rate for three separate frequencies. Downward arrows indicate that no visible crack growth was detected.

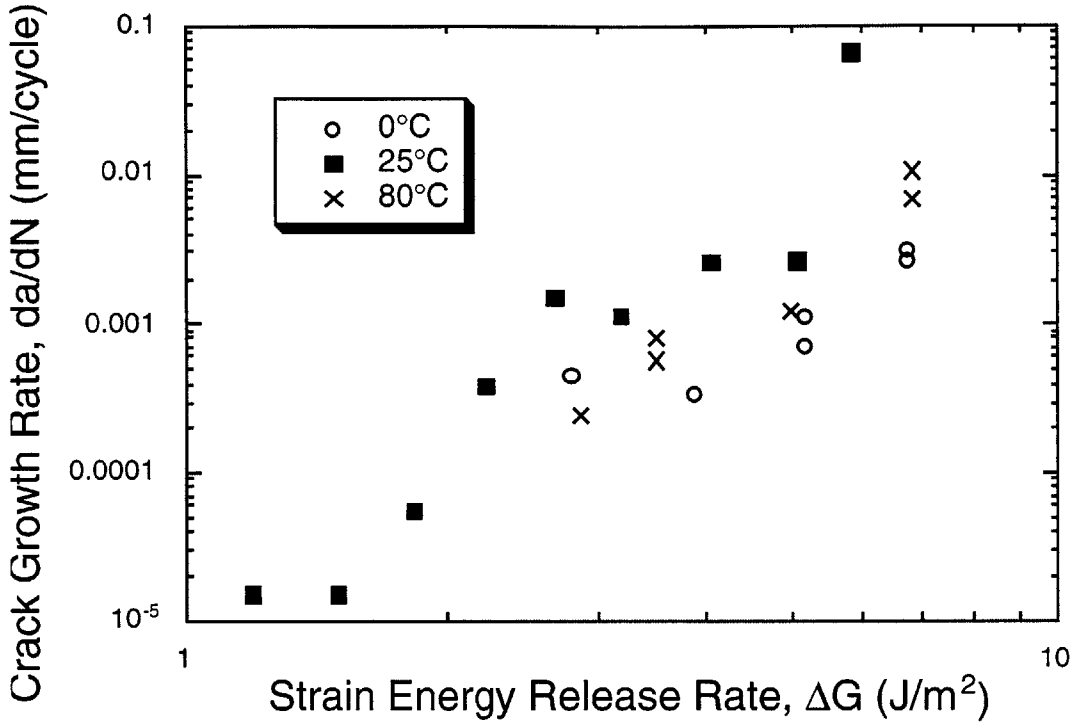

Figure 19: Crack growth rate versus strain energy release rate for RT, 80°C, and 0°C at 1 Hz.

Appendix A: Additional Literature Review

The fatigue of solder joints due to the thermal expansion mismatch of joined components has been a well-known problem in the microelectronics industry for decades. The understanding of the mechanisms contributing to thermal solder fatigue has been mostly anecdotal. To compound the issue, a majority of solder and microelectronics manufacturers either do not publish data collected on solder joint fatigue or the data obtained were too narrow a range to be extrapolated to make broad conclusions on solder behavior under a cyclic thermal strain. This work provides a new method for investigating solder fatigue without performing time-consuming cyclic thermal tests; therefore, there are no direct references regarding the piezo-induced fatigue of solder joints. However, in order to gain a complete understanding of the problem, it was necessary to investigate past work on the fatigue of solder in general, whether by mechanical or thermal means. This knowledge was then applied to the case of piezo-induced solder fatigue. The background literature research performed for this work considered the stresses experienced by adhesives in loaded joints, cyclic strain life prediction methodologies of solder joints, and fracture mechanics methodologies to predict crack growth.

Background to Solder Fatigue

Solder joints fail due to one or more interacting loading conditions: cyclic differential thermal expansion, vibration (high-cycle fatigue), thermal shock (rapid temperature change), mechanical shock (high acceleration due to misuse).[1] However, the primary concern for solder joint reliability is the cyclic differential thermal expansion problem. The common method for determining joint reliability is to perform both low-cycle and high-cycle fatigue tests on potential joint designs. The low-cycle fatigue tests more accurately simulate the effects that influence long-term reliability such as dwell time (creep) and environmental exposure; however, accelerated testing allows for a lifetime of cycles to be applied to a potential joint design.[1]

Stresses in Adhesive Bonds

Shear lag modeling of adhesive single and double lap joints was first performed by Volkerson in the 1930s.[2] This initial analysis assumed that the adherends were rigid and that the adhesive deformed uniformly with constant shear strain. Further analysis with single lap joints was performed by Goland and Reissner in the 1940s, which accounted for elastic adherends and subsequent edge shear effects in the solder.[2] Hart-Smith derived explicit analytical solutions

for double lap joints, extending the elastic solution to account for adhesive plasticity, adherend stiffness imbalance, and thermal mismatch between adherends.[3] Hart-Smith discovered that the load-carrying capability of a joint increases with adherend overlap only up to a certain point, beyond which no greater load transfer can be realized, giving rise to the concept of a slip length.

Strain-Based Approach to Solder Joint Fatigue Life Prediction

Many researchers have worked extensively developing models to understand and predict the fracture behavior of solder joints. Initially, researchers believed the fatigue life of a solder joint was based solely on crack initiation. Final failure was considered imminent after crack initiation. The Coffin-Manson law, developed in the 1950s, uses a linear cumulative damage concept based on cyclic strain range to predict the number of cycles to failure of solder joints.[4] In the late 1960s and early 1970s, researchers at IBM and Bell Laboratories discovered that the Coffin-Manson relation was in need of modification because other factors were found to affect the fatigue life of the solder joint. Frequency and maximum temperature during thermal cycling were experimentally found to be important factors affecting fatigue life, and a modified Coffin-Manson equation was proposed to account for these effects.[5] High temperature dwell time was also found to have an effect, and the Coffin-Manson equation was further modified.[6] Assuming that the plastic strain term in the original Coffin-Manson equation was pure shear and applying fitting techniques based on test data to account for frequency and temperature effects, Engelmaier developed an advanced model for predicting the fatigue life of LCC (leadless chip carrier) solder joints.[7] The Coffin-Manson equation (and its derivatives) uses terms related to the mechanical properties of the bulk solder and joint geometry, except for the strain levels, which must be calculated by additional detailed analysis. In the one-dimensional case, these strains are usually easy to determine, but strain mapping may be required for multi-dimensional cases before applying the Coffin-Manson equation.[8] Lau indicates that the Coffin-Manson equation can still be used for fatigue life predictions of SMT (surface mount technology) solder joints if detailed strain analysis for both plastic and creep strains is performed, most likely by using a finite element method with a mapping function.[8]

Fracture Mechanics Approach to Solder Joint Fatigue Life Prediction

Although prediction methodologies involving crack initiation have been developed for 50 years, it has been only recently that prediction methods of crack extension life have been applied to the solder joint problem. However, Lau clearly states that there are four stages of

the solder fatigue process: (1) crack initiation, (2) slip-band crack growth, (3) crack growth on planes of high tensile stress, and (4) ultimate ductile failure.[8] The later stages involving crack growth were typically ignored in terms of solder joint fatigue life prediction until the late 1980s and early 1990s. For cases where macroscopic cracks form and extend, fracture mechanics-based life prediction methodologies were found to be valid. Damage or *J* integrals describing the rate of change of potential energy by an advancing crack were applied to fatigue life prediction of solder joints, as was the C^* integral, which is the viscous analog of the path-independent *J*-integral based on a power-law steady-state creep assumption.[9, 10] Crack growth rate, *da/dN*, data were collected on solder joints by Kaminishi et. al. and compared to FEM predictions of crack extension path and life.[11] Regions of initiation, steady-state crack growth, and failure were observed in the data. Logsdon et. al. accumulated much data on the fracture behavior of monolithic solder including J_c, a measure of the toughness of the solder joint which has been used by Pao and others as a failure criteria. The fatigue crack growth rate of bulk solder was found at various temperatures and frequencies. It was found that the crack growth rate of eutectic solder decreased with a decreasing temperature over the range of 24 to -55°C and was insensitive to frequency over the range of 2 to 10 Hz.[12]

In order to create a Paris-type relation with this work to complete the fracture mechanics approach to solder fatigue life, the collected crack growth data must be compared to a calculated strain energy release rate for the solder joint. Shetty developed equations for interfacial strain energy release rate for debonding in single lap joints as well as double lap joints undergoing simultaneous debonding of both interfaces.[13] The equations were based on the steady-state phenomenon, assuming that crack propagation is independent of crack length. Uniform, in-plane forces of the individual layers were given by Euler-Bernoulli beam theory.

Appendix A References

1. Engelmaier, W. "Surface Mount Solder Joint Long-term Reliability: Design, Testing, and Prediction." *Soldering and Surface Mount Technology.* **1**, 1989, pp. 14-22.

2. Lau, J. H. *Solder Joint Reliability: Theory and Applications.* New York: Van Nostrand Reinhold, 1991.

3. Hart-Smith, L.J. "Adhesive-Bonded Double Lap Joints." *NASA CR 112235*, 1973.

4. Manson, S.S. "Behavior of Materials under Conditions of Thermal Stress." *NACA Report 1170,* 1954.

5. Norris, K.C., A.H. Landzberg. "Reliability of Controlled Collapse Interconnections." *IBM Journal of Research and Development.* May, 1969, pp.266-271.

6. Shah, H.J., J.H. Kelly. "Effect of Dwell Time on Thermal Cycling of the Flip-Chip Joint." *Proceedings of the ISHM Symposium.* 1970, pp. 3.4.1-3.4.6.

7. Engelmaier, W. "Functional Cycling and Surface Mounting Attachment Reliability." Surface Mounting Technology: *Monograph Series 6984-02.* ISHM, Silver Springs, MD, 1984.

8. Lau, J.H. and D.W. Rice. "Solder Joint Fatigue in Surface Mount Technology: State of the Art." *Solid State Technology.* **28** (10) 1989, pp. 91-104.

9. Subrahmanyan, R., J.R. Wilcox, and C.-Y. Li. "A Damage Integral Approach to Thermal Fatigue of Solder Joints." *IEEE Transactions on Components, Hybrids, and Manufacturing Technology.* **12** (12) 1989, pp. 480-491.

10. Pao, Y-H. "A Fracture Mechanics Approach to Thermal Fatigue Life Prediction of Solder Joints." *IEEE Transactions on Components, Hybrids, and Manufacturing Technology.* **15** (4) 1992, pp. 559-570.

11. Kaminishi, K., M. Iino, M Taneda, "Fatigue Life Prediction of Microelectronics Solder Joints." *Experimental Mechanics vol. 2 - Advances in Design, Testing, and Analysis, I.M.* Allison, ed. A.A.Balkema/Rotterdam/Brookfield, 1998, pp. 975-980.

12. Logsdon, W.A., P.K. Liaw, and M.A. Burke. "Fracture Behavior of 63Sn-37Pb Solder." *Engineering Fracture Mechanics.* **36** (2), 1990, pp. 183-218.

13. Shetty, S.P. *Fracture and Failure of Layered Materials Under Thermomechanical Loading.* S.M. Thesis, Cambridge: Massachusetts Institute of Technology, 1997.

Appendix B: Specimen Manufacture

Materials Selection

The piezoceramic material selected to perform the desired actuation is lead-zirconate-titanate (PZT) 5H from Piezo Systems, Inc. PZT 5H was chosen because of its actuation capabilities in the in-plane direction; Table B1 details the properties of PZT 5H. Piezoelectric materials deform under an applied electric field; they expand in one direction and contract in the other direction (this is partially due to Poisson's contraction). A piezoceramic is poled by exposing it to a strong electric field, which orients the domains, creating a preferred actuation direction. After poling, when the piezoelectric is exposed to an electric field, the domains respond by Coulombic attraction or repulsion, resulting in deformation of the material (Figure B1). The strongest piezoelectric effect is in the direction of the applied electric field, usually through the thickness, conventionally defined as the three (3) direction, as shown in Figure B2. Subsequent deformation also occurs perpendicular to the applied electric field (1 direction). In this study, the focus was on this latter 31 actuation; the electric field was applied through the thickness and the actuation was in-plane or perpendicular to the applied electric field.

The substrates were bonded with eutectic lead (37 wt%)-tin (63 wt%) solder preform from Indium Corporation. The piezoceramic substrates were supplied coated with a 5000 Å gold layer over an electroless nickel-plated metallization to promote wetting of the solder. Piezoceramic with traditional nickel electrodes were found to have a tenacious oxide layer that prevented solder wetting. Figure B3 shows the futile bonding attempts using piezoceramic with nickel electrodes. The use of flux is not prudent because gas evolution leads to bubbles in the final solder joint, especially when the joint is bonded over a large area. Therefore, the use of a gold adhesion layer became necessary to promote wetting without a flux.

The thickness of the solder joint was chosen to be 25.4 μm (1 mil), which is considerably smaller than the thickness of the piezo adherends of 0.19 mm thick (7.5 mil). Joints of this thickness are typical in the microelectronics industry and, thus, are of great interest to microcomponent manufacturers. Eutectic lead-tin solder was chosen as the adhesive because it is probably the most widely used solder; therefore, a substantial amount of information is available regarding its mechanical properties.

Piezoceramic Characterization

In order to generate the maximum shear strain on the solder, it is desirable to operate the piezoceramic over its maximum actuation range. Because piezoelectric materials have a preferred direction of actuation, defined by the poling direction, this maximum actuation range is asymmetric. The range is bounded by the shortage voltage in the positive actuation direction (poling direction) and by the depoling voltage in the negative actuation direction. When a poled piezoceramic is operated within these limits, a fairly linear strain-voltage curve is generated, as shown in Figure B4. When the depoling voltage is exceeded, the piezoceramic returns to its natural, unpoled state, characterized by a "butterfly curve" (see Figure B18). If the voltage limit in the positive actuation direction is exceeded, the piezoceramic will spark and will result in destruction of part or all of the piezoceramic. Experiments using a laser interferometer were performed to determine the exact voltage limits for the supplied PZT 5H. Strain was measured for a given DC offset voltage and AC cycling voltage. Data from these experiments is shown in Figures B4 through Figures B17. From these experiments, it was found that the maximum voltage range is -200 V to +400 V. In order to remain well within the useful actuation range and to avoid possible depoling of the ceramic but still achieve the maximum actuation possible, the actuation range for the experiments performed in this study was restricted to -150 V to +350 V, corresponding to an electric field of 0.79×10^6 V/m to 1.84×10^6 V/m). These limits were never quite reached during testing (-100 V to +300 V) due to excessive sparking and subsequent rapid failure of the piezoceramic or joint. An H-bridge voltage cycling circuit, as detailed in Appendix C, is utilized in the asymmetric voltage application. The effective piezoelectric strain coefficient defined in this study is based on the maximum strain range for each supplied voltage level. The value of d_{31} is plotted versus voltage in Figure B19. A line was fit through the data and a linear equation for d_{31} as a function of voltage was determined. The fit deviates from the data below $\pm$ 50 V; however, no testing was performed below $\pm$ 90 V because of the shear strain requirements. Therefore, the d_{31} in future calculations is based on values determined through this linear fit.

Specimen Geometry

The specimen geometry consists of three piezo sheets joined by two solder joints as shown in Figure 8. Using the characterization data of the piezoceramic, it was determined that the actuation of a single piezo sheet adhered to a rigid substrate would not be sufficient to achieve the levels of strain that are induced during a typical thermal cycle. To achieve the desired strain levels in the solder, the piezoceramic adherends must be actuated in opposite directions. In order to eliminate the bending that is induced by such a configuration, the resulting tri-layer

symmetric stack was designed. The shorter piezo sheets (0.25 $\times$1.25 in) are actuated 180° out-of-phase from the longer, inner piezo adherend (0.25 $\times$1. 5 in). When the center piezo contracts, the outer two piezos expand and vice versa. This allows the shear strain in the solder to be doubled without inducing bending. The center piezo tab permits electrical connections to be made and aids in holding the specimen in the holder. The first batch of specimens was manufactured with one center tab, and the second set was manufactured with tabs on both ends. The dual tabs are shorter, 0.175 in, compared to 0.25 in of the first batch. Dual tabs provide greater flexibility during testing because they allow the specimen to be reversed in the specimen holder during testing should the center tab break or if the free end is needed to facilitate cracking (K_I mode). The piezo sheets were cut to specifications (0.01 in tolerance) by Piezo Systems, Inc as shown in Figure B20.

Joint Manufacturing Procedures

The piezo/solder stacks were manufactured by first cutting the solder preform to the proper size, cleaning the adherend and adherent surfaces, carefully arranging the layers, then placing the stack in either a reflow solder oven or a belt furnace. The piezo sheets was provided with a red ink mark indicating the positive-poled direction. When cleaning in acetone solution to remove dirt and oils, this red mark disappeared. To maintain the poled designation, the piezo ceramic was carefully chipped in the upper left corner when the red line was facing up. After cleaning, the positive poled side could be easily identified. Other options, such as scratching or marking the adherend surface were not as desirable because it could adversely affect the soldering process. The 1 mil thick solder preform ribbon was cut to the size of the joint (0.25 in $\times$1.25 in) using a razor blade on a clean glass surface with a straight edge. The piezo sheets and trimmed solder preforms were placed in an acetone ultrasonic bath for at least 15 minutes. Each piece was then removed from the bath, rinsed with acetone, and dried with an air jet. The components were then carefully stacked and aligned. A glass slide and small copper weights were placed on the stack to apply pressure. Reflow soldering was performed in a reducing atmosphere of nitrogen in a solder reflow oven (at Rockwell Science Center) for the first batch of specimens and in a belt furnace (at Olin-Aegis Corporation) for the second batch of specimens. For the first batch of specimens, a time/temperature profile was determined for optimum bonding of the solder joint, as shown in Table B2. For the second batch of specimens, which were prepared in a belt furnace, the temperature was fixed at 210°C; the pull speed of the belt was three inches per minute, which resulted in approximately the same hold time at maximum temperature as the first batch of specimens. It is standard procedure to set the

peak temperature of the reflow cycle to 40-50°C above the melting temperature of solder. The peak temperature achieved in this manufacturing procedure was 210°C, 27°C above the eutectic lead-tin solder melting temperature of 183°C. Higher peak temperatures were avoided to prevent the piezo from approaching its Curie temperature of 250°C, which is the temperature at which the poled domains randomly switch back to their natural state. If the piezos were to depole during manufacturing, there would be no way to repole them independently of one another and the specimen would be useless. After the cooled specimens were removed from their respective solder reflow devices, they were marked and individually wrapped with tissue paper and a cardboard backing for protection.

Verification of Joint Integrity

The integrity of the joint was verified in a variety of ways. First, the joints were sectioned and observed in the scanning electron microscope (SEM). The piezoceramic is not conductive and tends to charge in the SEM; therefore, the specimen was mounted on carbon tape, and the surface was coated with carbon paint. Some charging did still occur; however, it was kept to a minimum. The joints were inspected for voids, debonded regions along the interface, and other defects. The largest debonded region observed was approximately 150μm in diameter (Figure B21); the largest void observed was approximately 50μm in diameter (Figure B22). Next, the integrity of the joint was verified using ultrasound to observe the interior of the specimen nondestructively. Although the ultrasound was difficult to perform with a layered ceramic material, the scan seemed to indicate that the overall joint integrity was good. The resolution of the ultrasound was 2 mm, so it was unable to indicate small voids or debonded regions. Figure B23 shows the scan, with blue areas indicating well-bonded regions. In this specimen, the best bonding occurred in two square locations, exactly where the copper weights were placed. This specimen was made before glass slides were used to distribute the pressure over the entire joint. Because of time and cost constraints, another ultrasound scan was not made, but from this scan, it can be inferred that applying pressure over the entire joint should improve bonding.

Solder Composition

Upon observing the specimen in the SEM, it was immediately apparent that the eutectic tin-lead composition had been altered. The gold adhesion layer (approx. 4 wt%) completely diffused into the solder, creating a new gold-tin phase and shifting the relative contents of lead and tin in the remaining two phases. An electron dispersive spectroscopy (EDS) compositional analysis

can be seen in Figure B24. This new gold-tin phase is somewhat troublesome because it is well understood that gold embrittles solder. Although this phase was unavoidable in this study because of the need for wetting surfaces on the piezo, it could be avoided in future work if other electrodes that neither produce an oxide nor diffuse into the solder are used.

Specimen Polishing

In order for crack growth to be monitored *in situ*, at least one edge of the piezo/solder stack must be polished. It is difficult to polish the stack because piezoceramic and solder have such disparate values of toughness and hardness. Also, the crucial center tab in the piezo stack has a tendency to break off, rendering the specimen useless. A mounted and polishing procedure was developed to address these problems. The specimens were mounted temporarily in a thermoplastic wax material (Crystalbond) between square bars of steel. The bar dimensions were 1.75 in $\times$0.25 in $\times$0.25 in. Therefore, the height of the bar was the same as the piezo/solder stack on its edge. The bars and thermoplastic assembly acted to hold the piezos securely in place during polishing while protecting the fragile piezo tab. To mount the specimens, a polishing disk was heated on a hot plate and Crystalbond was melted on to it. The bars were then placed down and the specimens placed between them. More Crystalbond was applied, and then the assembly was cooled and ready to polish. Four to seven specimens could be polished at the same time depending on the size of the polishing disk used. To polish, sandpaper of the following grits were used in succession: 240, 400, 800, 1200, 4000. Then 0.3μm alumina solution was used on a felt polishing wheel. This procedure yielded specimens that could be adequately viewed in the microscope during testing. A polished sample is shown in Figure 9. To remove the specimens from the temporary mount, the polishing disk was again heated on the hot plate until the thermoplastic was extremely fluid. Since the heated thermoplastic is a shear-thinning liquid, the specimens were slid out from the sides rather than pulled from the top. The specimens were allowed to air cool for a few seconds to reduce thermal shock and then were placed into an acetone bath. The acetone completely dissolves the thermoplastic, leaving a clean, polished surface.

Appendix B Tables

Table B1: Properties of PZT 5H (Piezo Systems, Inc.)

PIEZOELECTRIC:		
Composition		Lead Zirconate Titanate
Material Designation		PSI-5H-S4 ENH
Relative Dielectric Constant (@1 KHz)	K_{33}^{T}	3800
Piezoelectric Strain Coefficient	d_{33}	650×10^{-12} m/V
	d_{31}	-320×10^{-12} m/V
Polarization Field	Ep	1.5×10^{6} V/m
Initial Depolarization Field	Ec	3.0×10^{5} V/m
MECHANICAL:		
Density		7800 kg/m^3
Elastic Modulus	E_3	5.0×10^{10} Pa
	E_1	6.2×10^{10} Pa
THERMAL:		
Thermal Expansion Coefficient		3×10^{-6} m/m/°C
Curie Temperature		250°C

Table B2: Time/temperature profile of solder reflow oven for first batch of specimens. Total processing time ~ 35 min.

step	time (min:sec)	temperature (°C)	environment
0	00:10	25	air
1	02:00	25	vacuum
2	02:00	25	nitrogen
3	02:00	25	vacuum
4	02:30	40	nitrogen
5	06:30	170	nitrogen
6	05:00	210	nitrogen
7	02:30	210	nitrogen
8	01:00	210	vacuum
9	01:00	210	nitrogen
10	05:30	60	nitrogen
11	03:00	35	processing nitrogen +extra nitrogen

Appendix B Figures

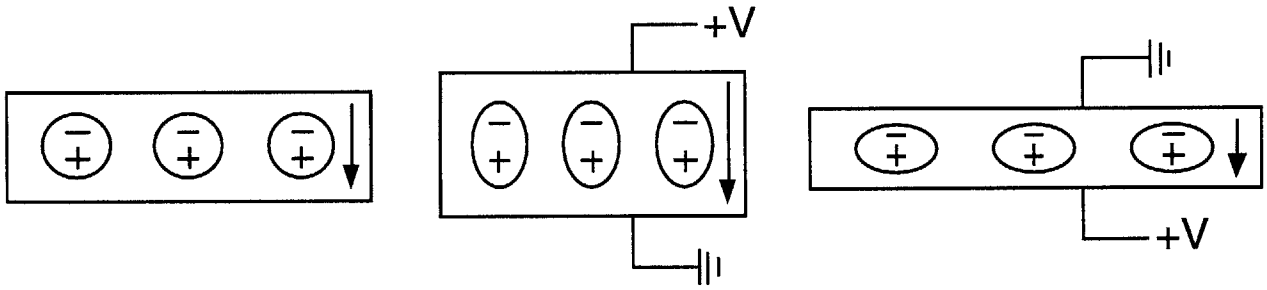

Figure B1: Response of a poled (arrow) piezoceramic to an applied electric field.

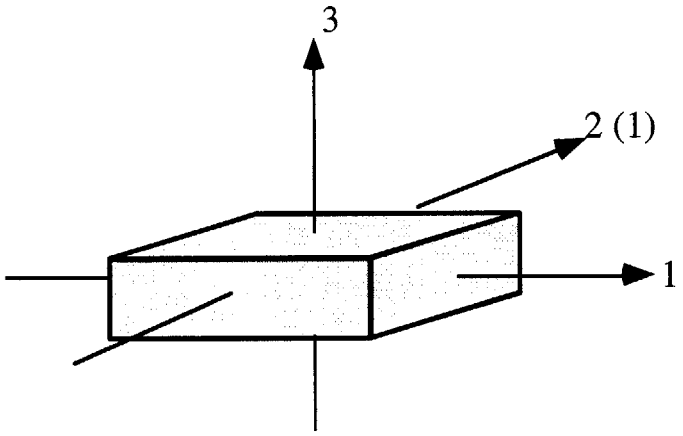

Figure B2: Piezoelectric axes.

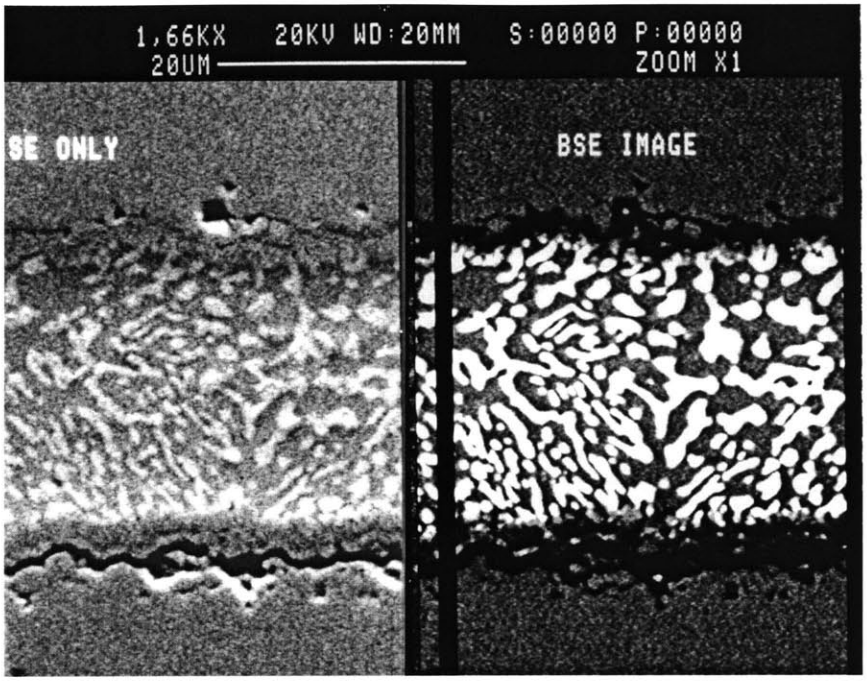

Figure B3: SEM backscatter image showing lack of bonding along nickel oxide/solder interface (nickel electrodes).

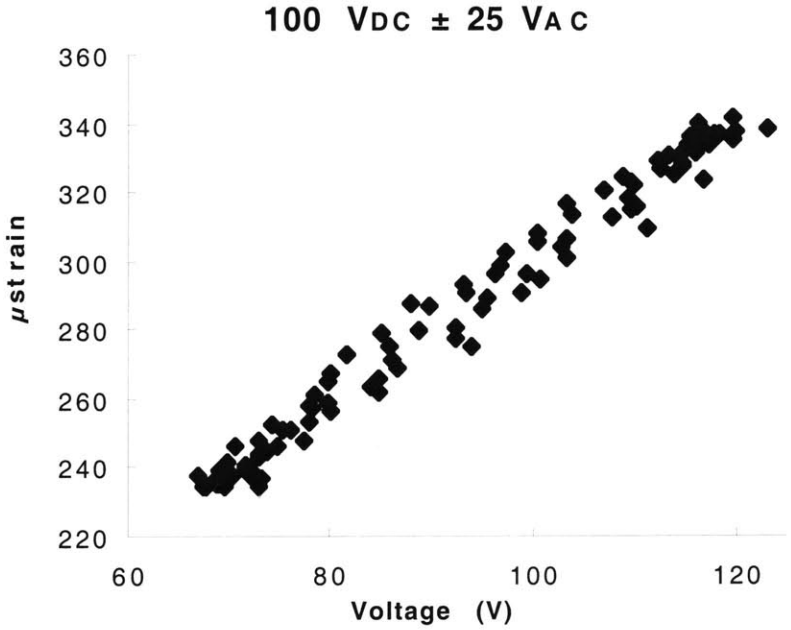

Figure B4: PZT 5H characterization.

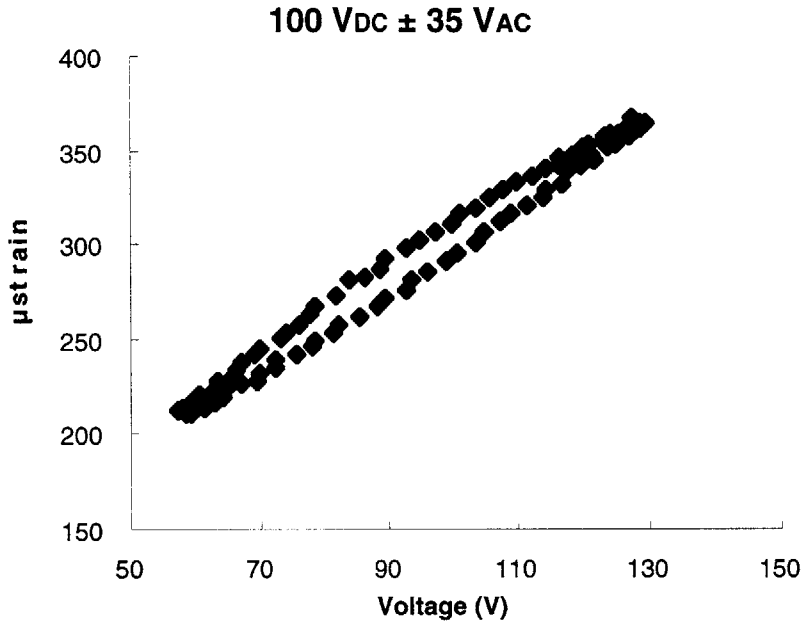

Figure B5: PZT 5H characterization.

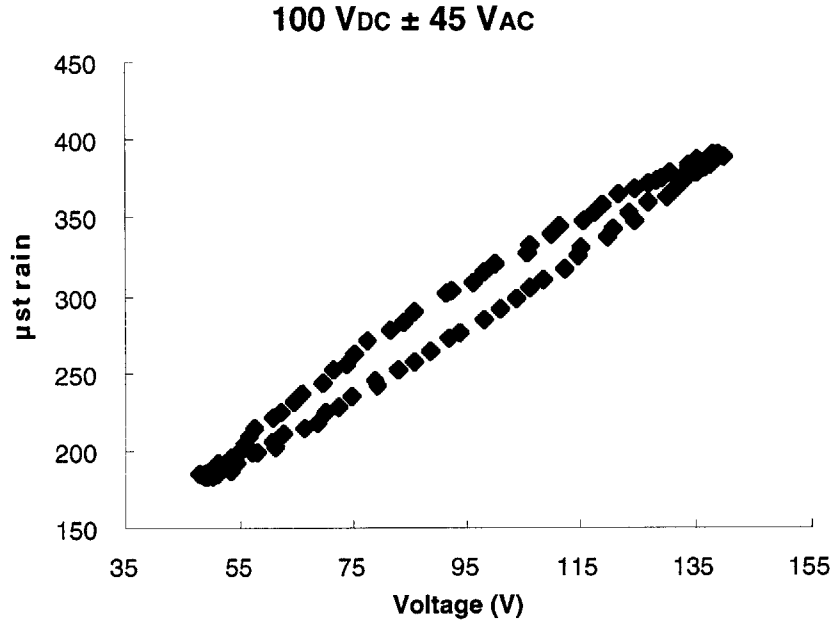

Figure B6: PZT 5H characterization.

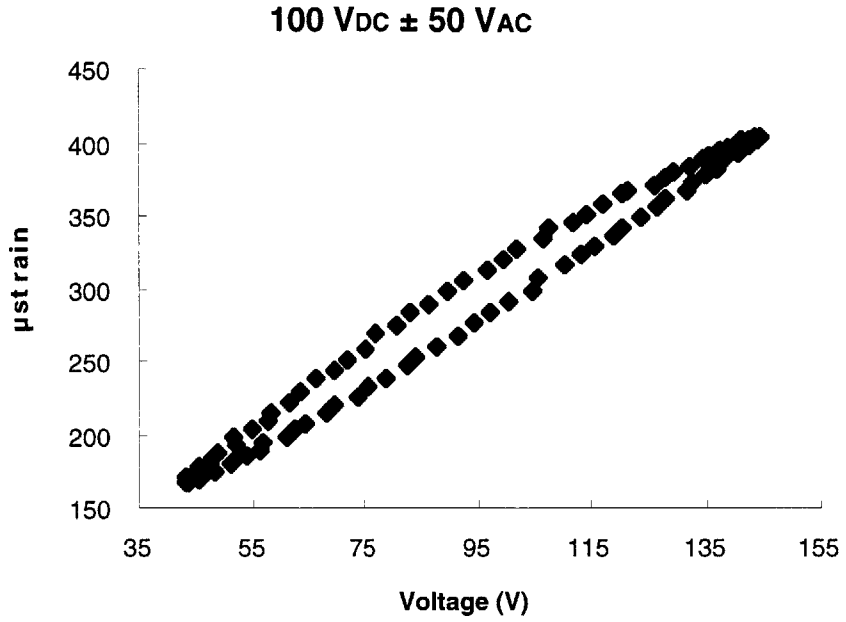

Figure B7: PZT 5H characterization.

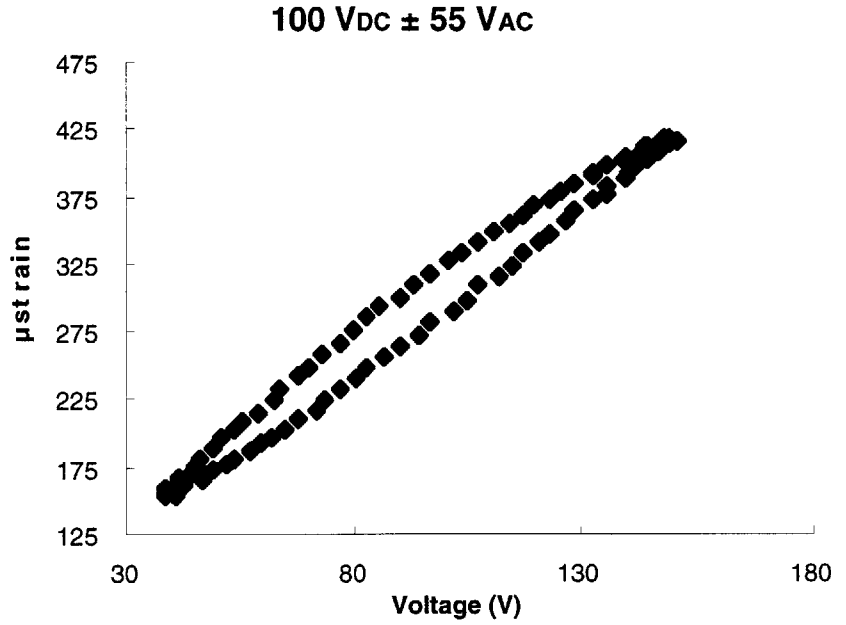

Figure B8: PZT 5H characterization.

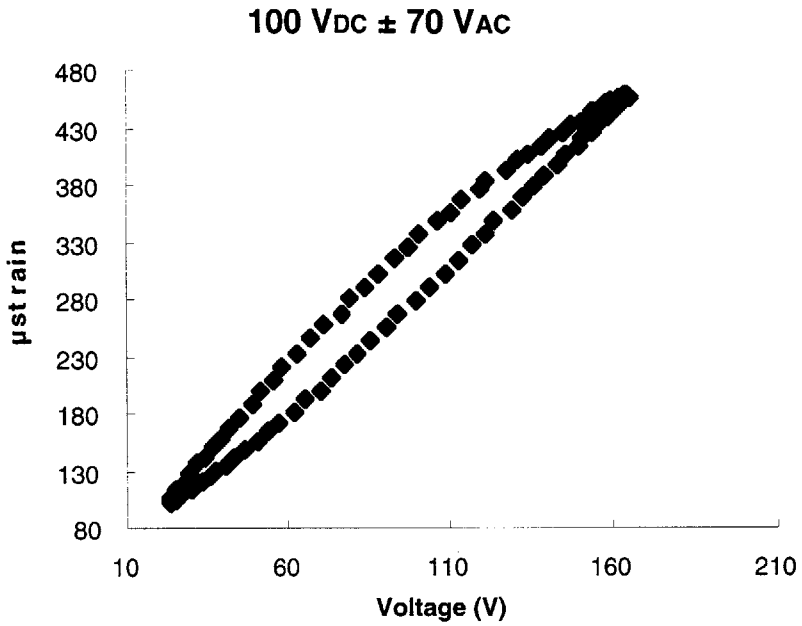

Figure B9: PZT 5H characterization.

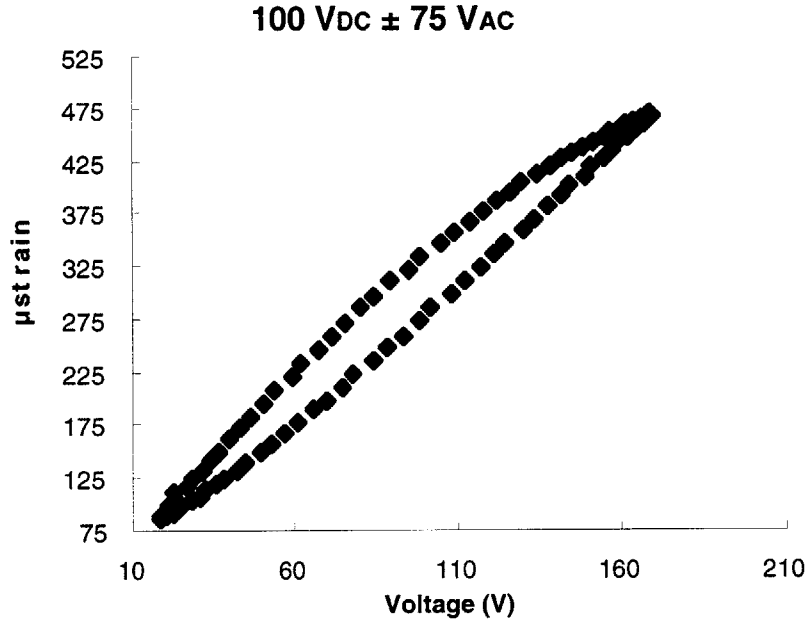

Figure B10: PZT 5H characterization.

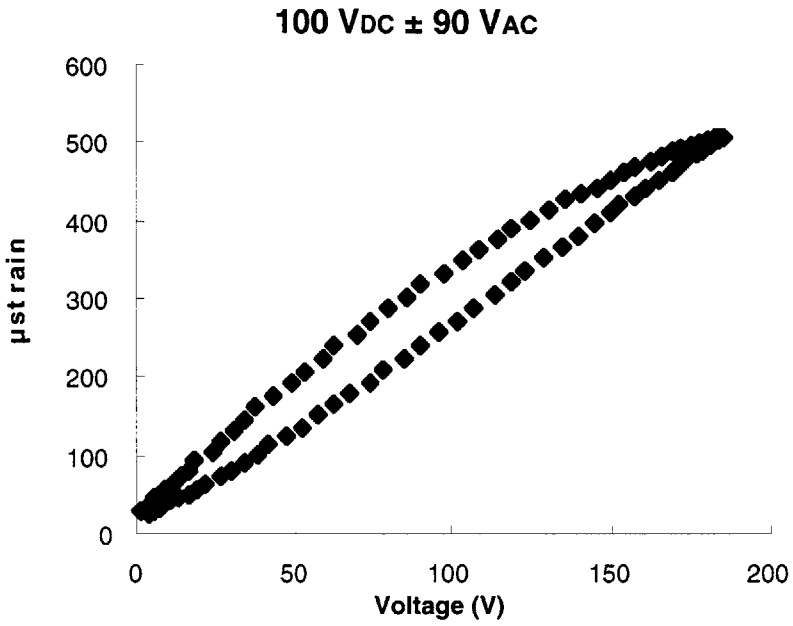

Figure B11: PZT 5H characterization.

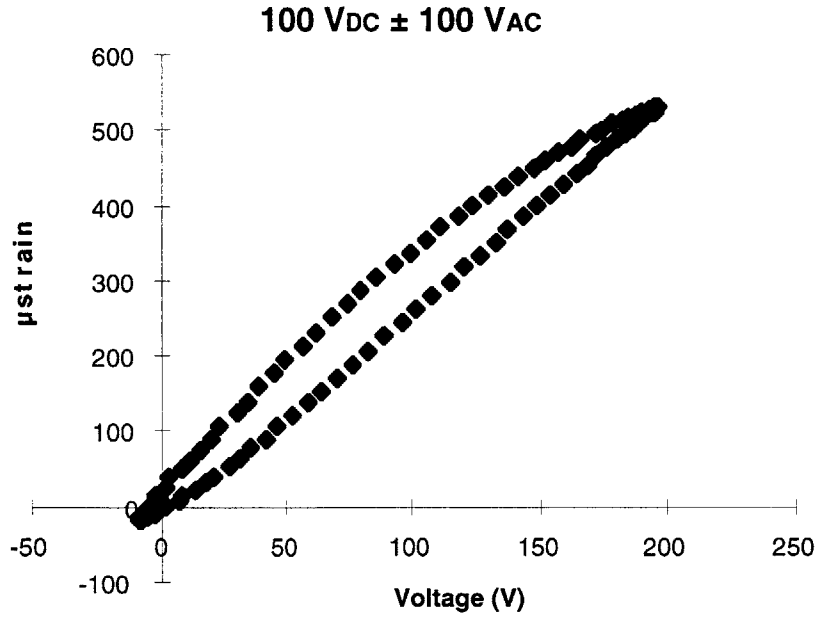

Figure B12: PZT 5H characterization.

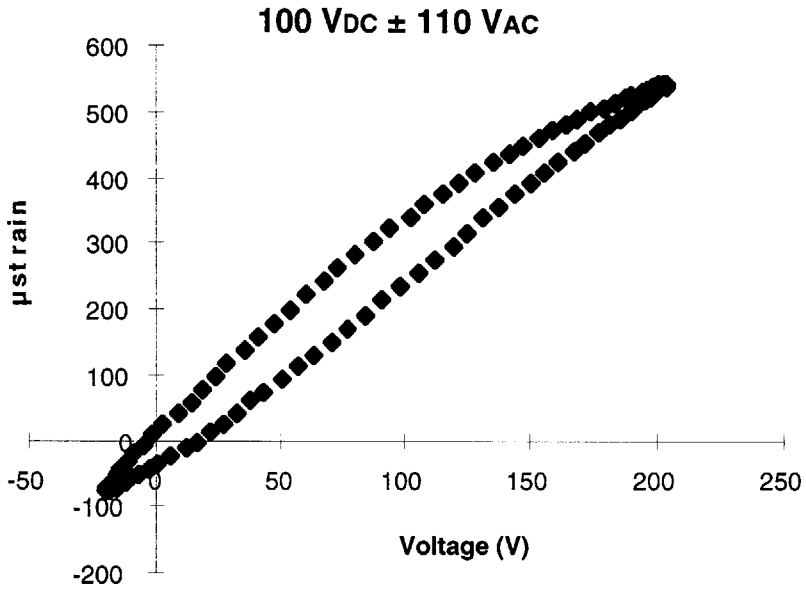

Figure B13: PZT 5H characterization.

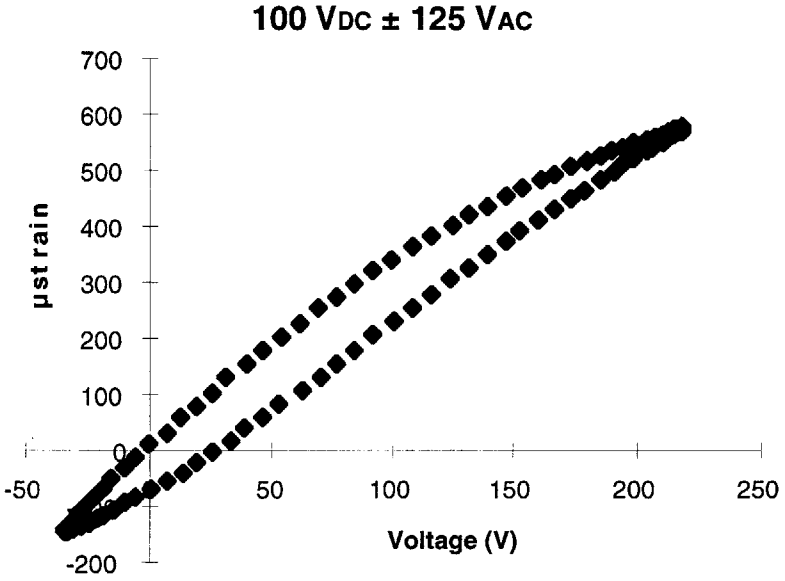

Figure B14: PZT 5H characterization.

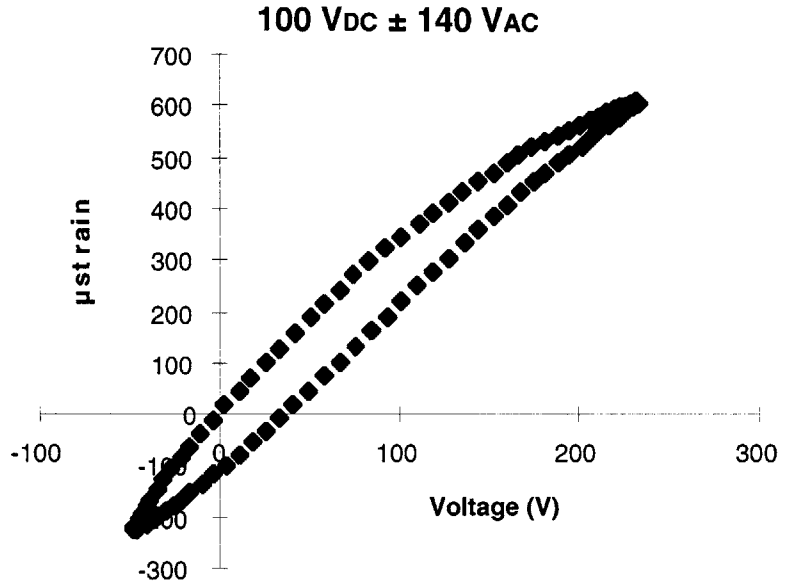

Figure B15: PZT 5H characterization.

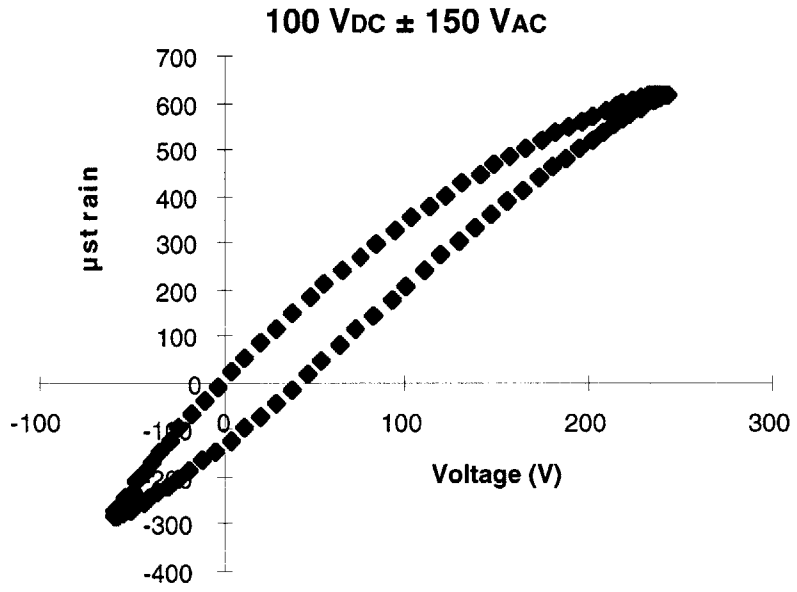

Figure B16: PZT 5H characterization.

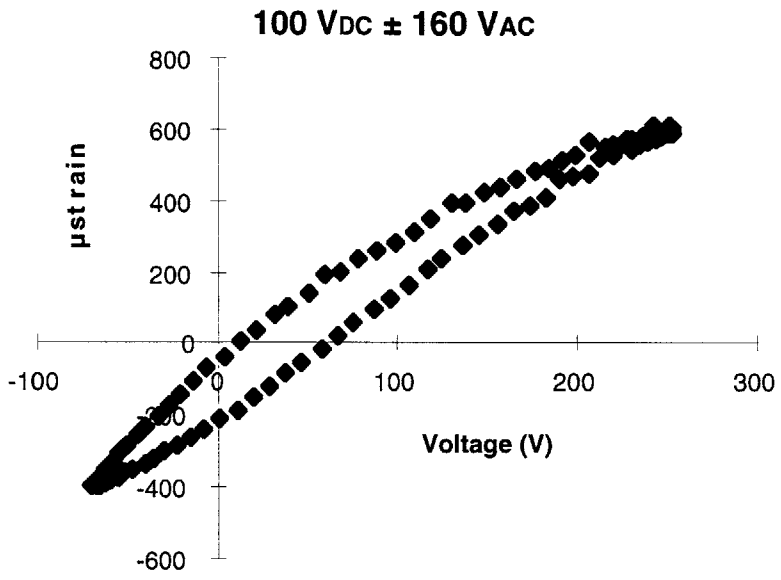

Figure B17: PZT 5H characterization.

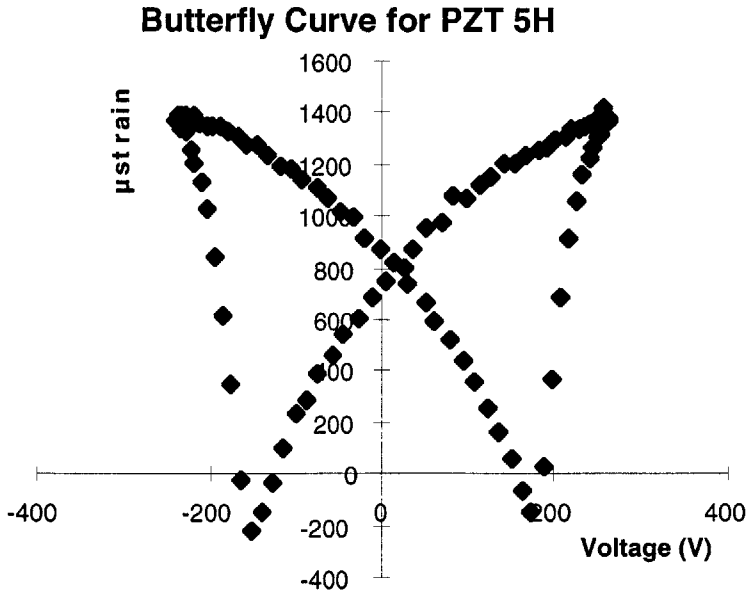

Figure B18: PZT 5H - butterfly curve, unpoled.

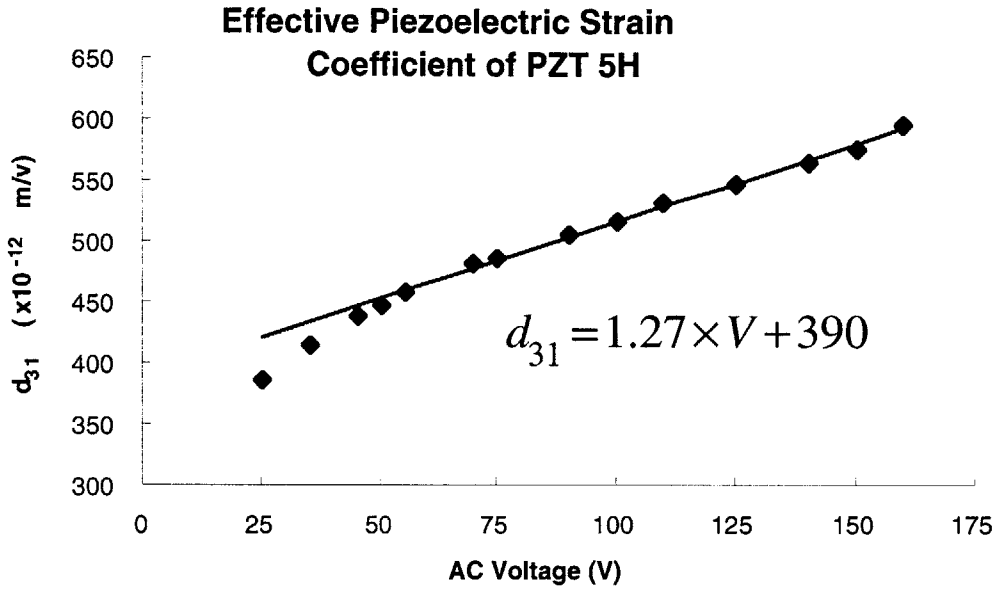

Figure B19: Piezoelectric strain coefficient as a function of voltage.

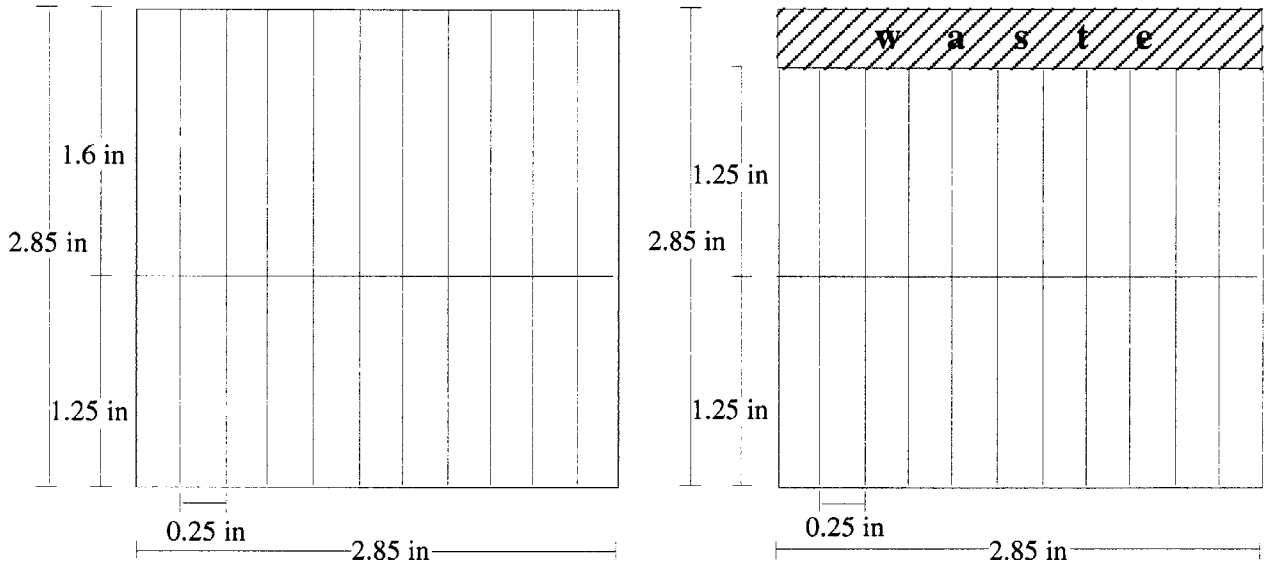

Figure B20: Cutting diagrams supplied to Piezo Systems, Inc. specifying the dimensions piezo sheets (dual tab configuration). Seven sheets of the left configuration and three of the right configuration were cut per ten sheet order, resulting in 70 long (center piezo) and 130 short (outer piezos) piezo pieces.

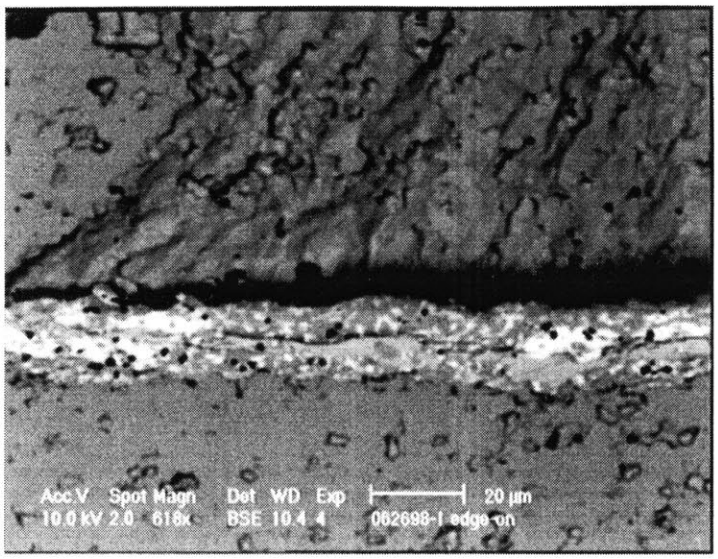

Figure B21: SEM photomicrograph of large debonded region.

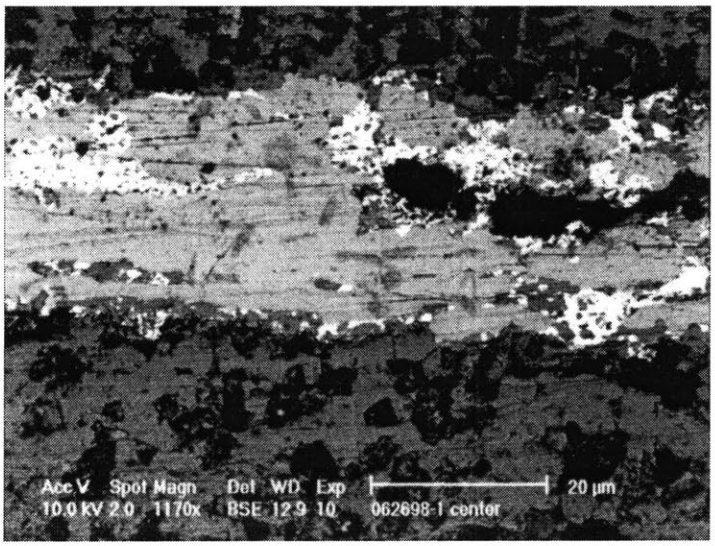

Figure B22: SEM photomicrograph of large void (internal section of solder joint).

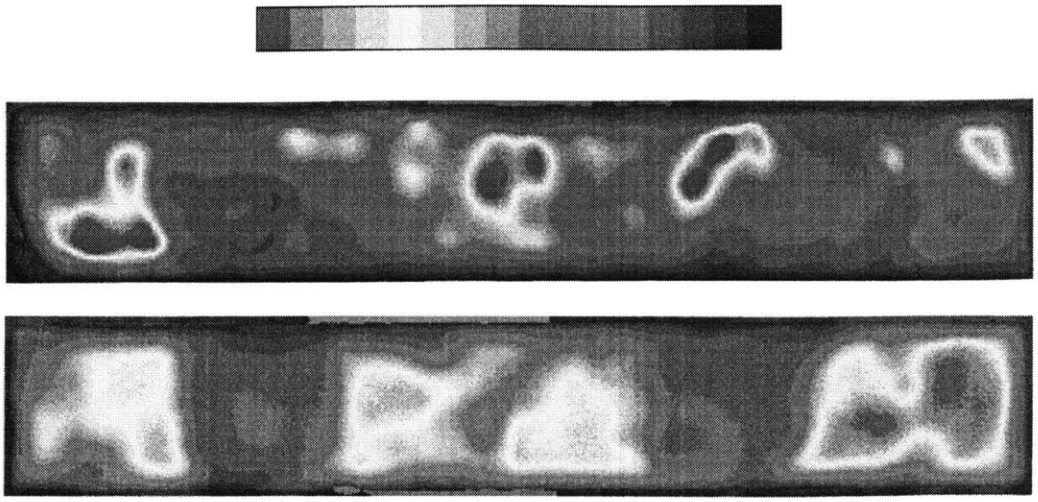

Figure B23: Ultrasonic scan of two piezo solder joints (bi-layer). Top: a two mil solder joint; bottom: a one mil solder joint. The bottom joint shows well-bonded regions where weights were placed during manufacturing.

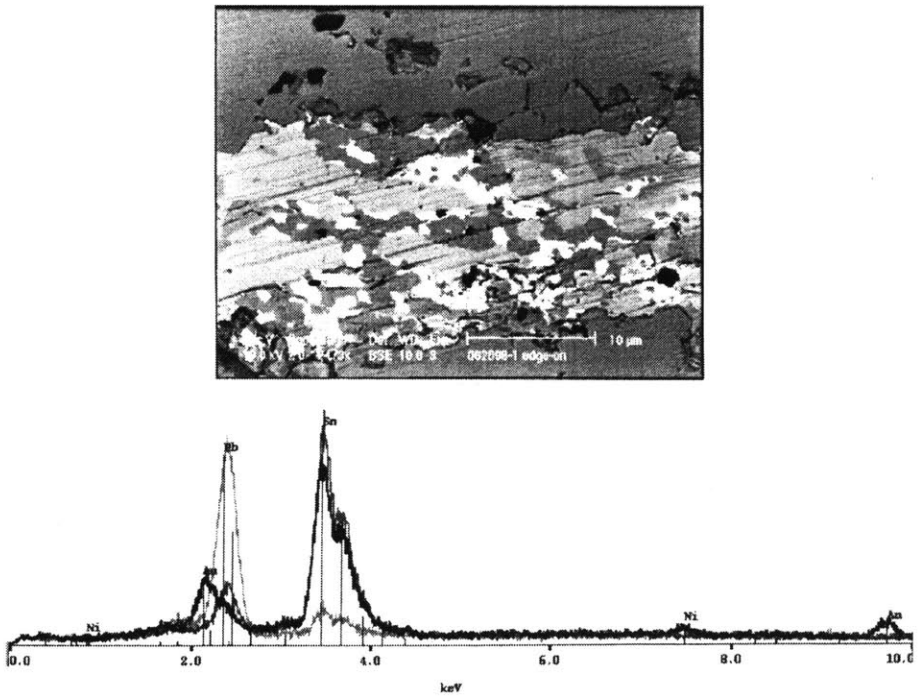

Figure B24: Compositional analysis of gold-embrittled solder. In photograph, bright regions: Pb-rich; medium gray regions: Sn-Au; dark gray regions: Sn-Rich.

Appendix C: Voltage Cycling Circuit Design and Construction

Voltage States

In order to achieve the maximum shear strain in the solder joint, the voltage levels must be cycled between the maximum allowable voltage settings as determined by the piezoelectric characterization. To avoid depoling or shorting the piezo, the maximum voltages used in this study were -100 V to +300 V accomplished by cycling up to ±200 V with a fixed 100 V DC offset. Each piezo sheet must achieve these voltage limits and be perfectly synchronized with the other piezos in the stack. If the center piezo is receiving + 300 V, then the outer two piezos receive -100 V and vice versa. Figure C1 shows the voltage states that must be achieved for each piezo sheet in the stack. The cycling voltage was varied from ±90 V to ±200 V achieve a range of strain levels.

Design of H-Bridge Voltage Cycling Circuit

Instead of using a variable AC power supply to produce the required cyclic voltage, an H-bridge voltage cycling circuit was designed and manufactured utilizing only DC power supplies. The circuit was largely designed by Craig Winterhalter at Rockwell International at Thousand Oaks, CA. The circuit utilizes a function generator to output a square wave to an inverter chip (MC14584B). The signal is then sent through an optical isolator chip (HCPL-4506), and another non-inverted signal is sent through a different optical isolator. Both of these chips' output signals are sent to separate gate drive chips (IR2101), which produce a high side and low side voltage that is fed through power n- and p-channel MOSFETS (IRFBC40). The outputs from the system are the AC and DC voltages required. The out-of-phase actuation of the piezos is created by the inverted and non-inverted signal generated from the same square wave signal acting as a double pole, double throw switch, as shown in Figure C2. An electrical diagram of the circuit can be found in Figure C3. The system requires a function generator, two 9 V batteries or power sources to drive the inverter chips, two 15 V power supplies to drive the optical isolator and gate drive chips, two high voltage (up to 200 V) power supplies that will provide the AC switching voltage, and one 200 V power supply that will be used to provide the +100 V and -100 V DC offset voltage. The system works by utilizing five isolated grounds and relative voltages between them, as shown in Figure C4. The function generator and the 9 V batteries share one ground, the 15 V and 200 V power supplies share another ground (2 sets), the 200 V power supply (offset voltage) has another ground, and the outputs of the system share a final ground. The outputs of the system

are two (+/-) AC voltages that are always opposite each other and are equivalent to the input voltage, one positive 100 V DC offset, one negative 100 V DC offset, and their respective grounds, which are connected externally to the circuit. The elegant nature of the design allows for variable frequency based on the input signal from the function generator and variable voltage based on the voltage input level from the power supplies.

Manufacturing of H-Bridge Voltage Cycling Circuit

A prototype of the H-bridge circuit was created by manually wire wrapping the components in a fiberglass electrical breadboard. This preliminary circuit was soldered after preliminary testing proved its switching capabilities at low voltages. After further testing, the electrical connections were found to be unreliable and inconsistent, which is unacceptable with the high voltages required for this study. Therefore, for safety and reliability reasons, a more permanent circuit was created using a copper-etched board. The board consists of two copper faceplates adhered to a fiberglass/epoxy composite core. From CAD computer instructions, a punching and milling machine etches out the traces, forming moats of non-conductive material around electrical connections. The moats provide a 0.43 mm (17 mil) track of insulation around the copper connections. Because the punched holes, where components are placed, have no electrical conductivity, small tubes of solder-coated nickel were injected into the holes of the board. The components are then dropped in and soldered to the copper surface. The process is extremely tedious and time consuming, plus unforgiving of small errors in soldering, which could delaminate the copper trace, causing a loss of electrical connections to part of the circuit. After successfully manufacturing one of these boards, high voltage testing was conducted. The electrical insulation of the etched tracks proved to be insufficient, as the circuit failed to work above ± 150 V due to a short that failed the system. The electrical breakdown was most likely caused by a small solder defect, such as a fleck of solder spanning the insulating track. Another circuit manufacturing technique that provided more insulation was employed. A professional printed circuit board made of plastic with a solder mask was contracted. Compared to the copper-etched board, the printed circuit board featured substantial improvements, such as solder-lined punch holes, greatly enhanced insulation, and ease in soldering, all of which contributed to a more reliable and stable H-bridge circuit. This final design was manufactured and tested up to ± 250 V repeatedly for several hours of continuous usage with no problems or failures. To contain and protect the printed circuit board, a standard aluminum electronics box with banana clip terminals was constructed. The box is grounded to G2, the ground of the high voltage power supplies.

Appendix C Figures:

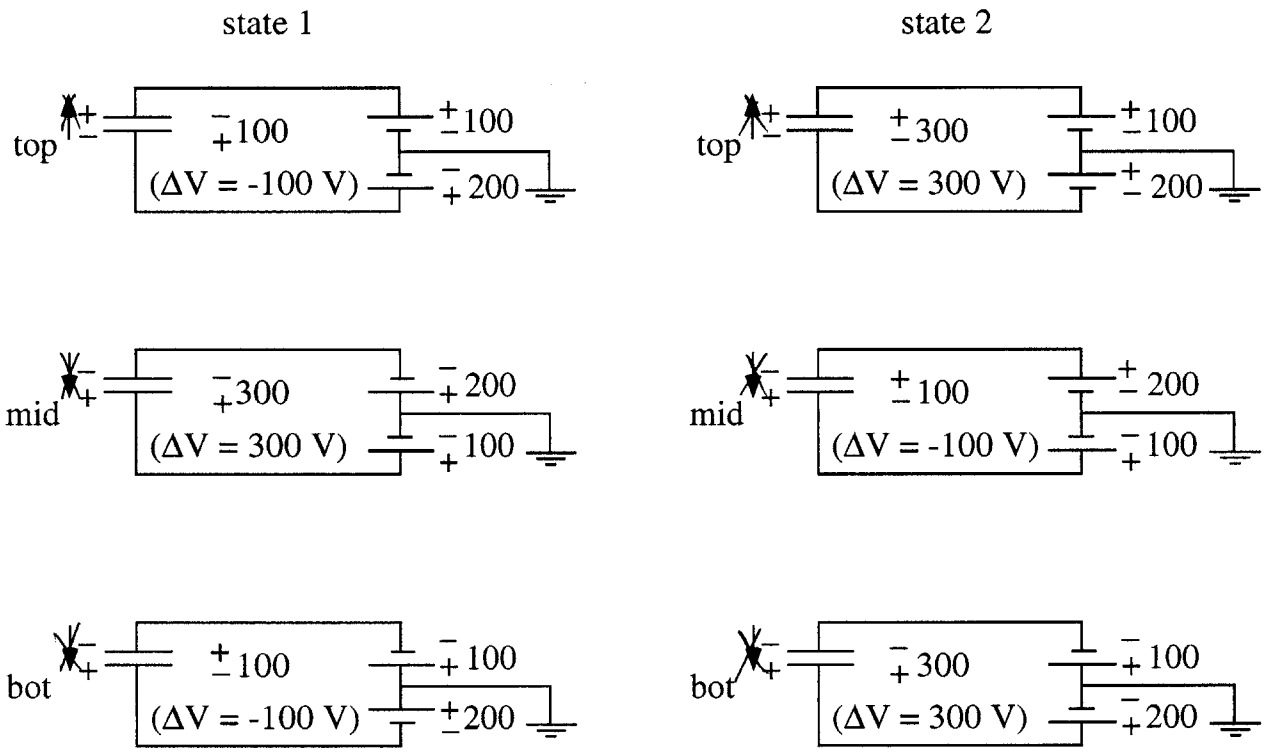

Figure C1: Voltage states for the top, middle, and bottom piezos in the piezo/solder stack (maximum actuation range). The arrow indicates poling direction.

H-bridge state 1:

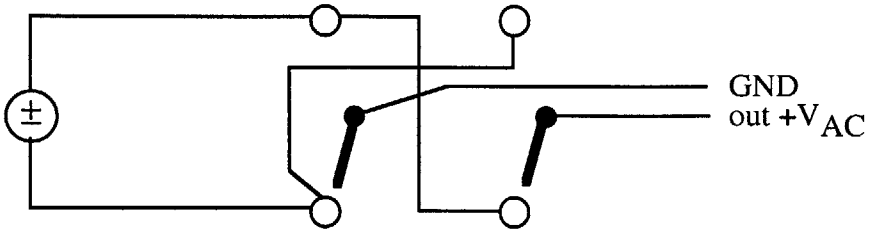

H-bridge state 2:

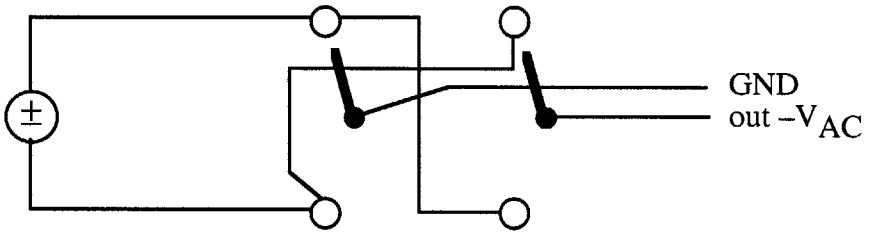

Complete System:

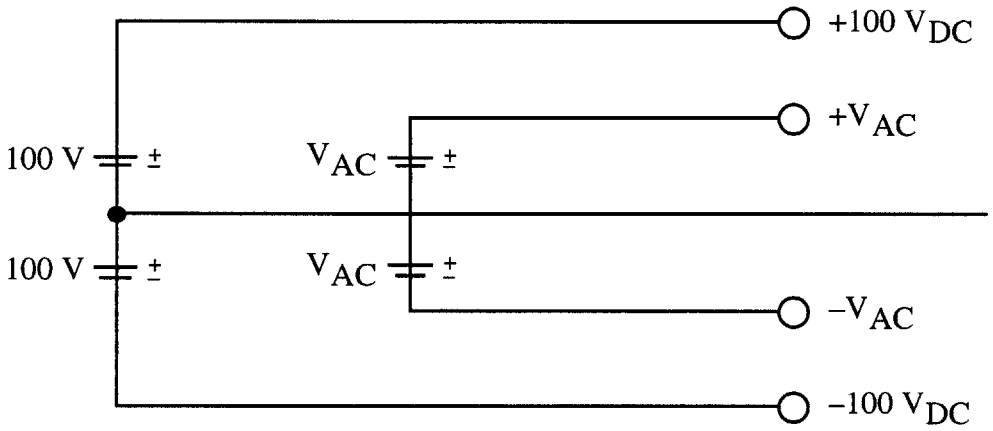

Figure C2: H-bridge switching circuit - graphical interpretation.

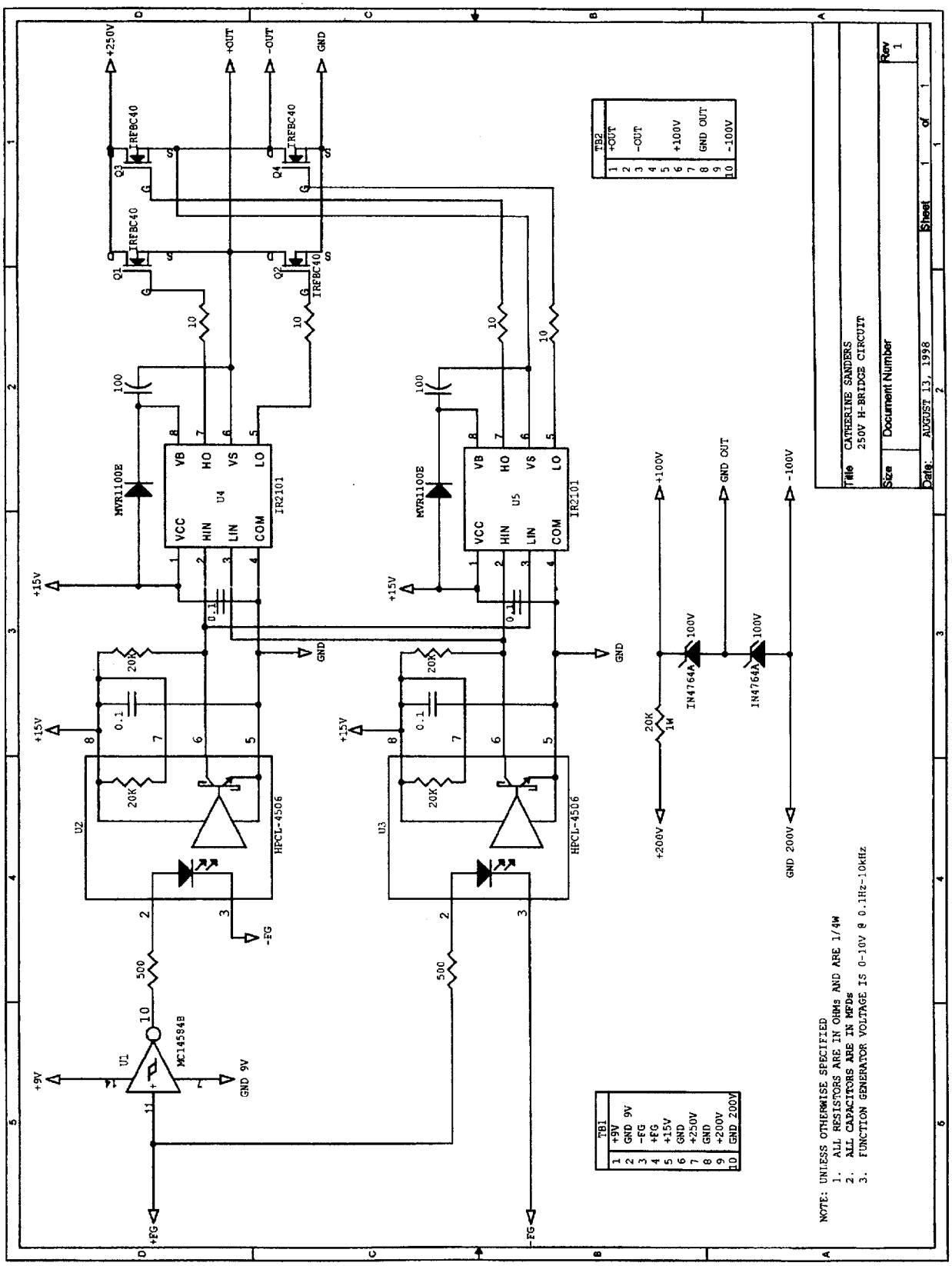

Figure C3: Electrical schematic diagram of H-bridge voltage cycling circuit.

H-bridge Circuit:

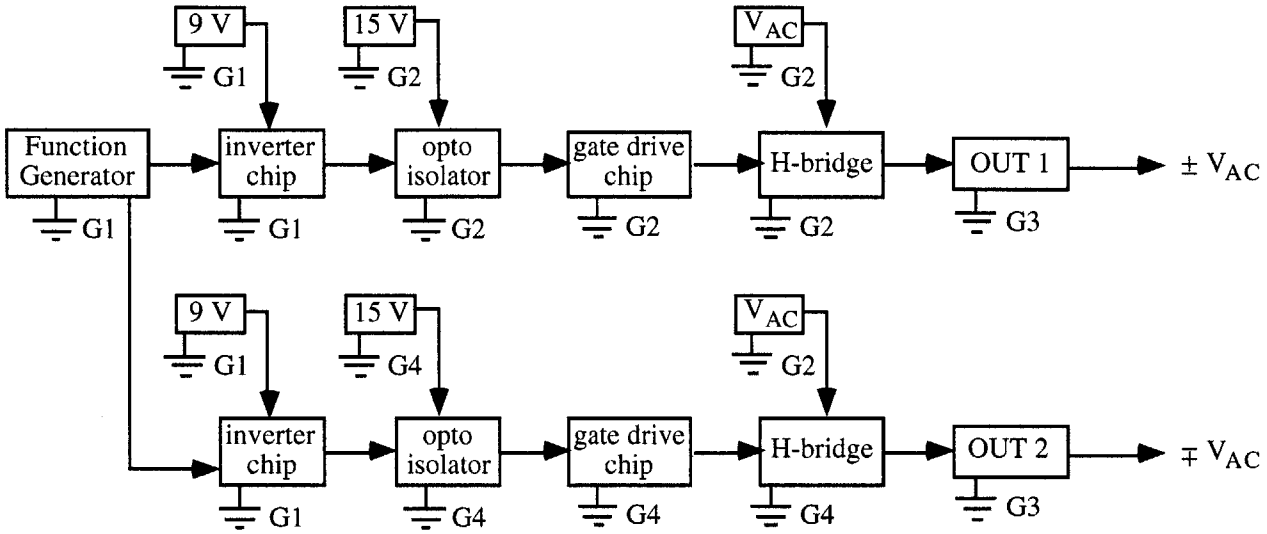

DC Offset Circuit:

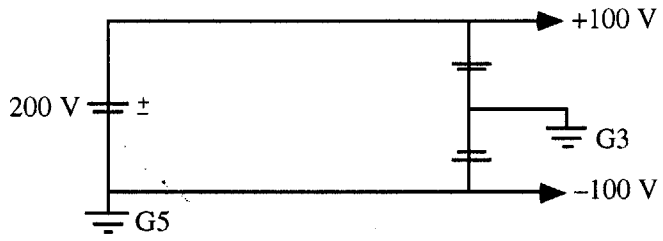

Figure C4: 5 isolated grounds in H-bridge circuit.

Appendix D: Fatigue Testing

Experimental Set-Up

The experimental set-up consists of three high voltage power supplies ($\pm$1000 V, 40 mA Kepco Amplifiers), two 13.8 V power supplies, and a function generator arranged on a moveable cart plus the circuit box, which is placed on a laboratory table. The inverter chip in the circuit box is powered by either two 9 V batteries or two external 9 V power sources for long duration testing, because the batteries drain after approximately 6 to 7 hours. There were several components of the experimental set-up that were constructed to facilitate testing: a specimen holder to secure the specimens at one end and to provide electrical connections to the piezo sheets; an interrupt box to provide a voltage cut-off between the specimen holder and the circuit box; and a thermal box to test the specimen isothermally at temperatures other than room temperature.

Specimen Holder

The specimen holder provides two important functions. Firstly, it enables the delivery of voltage to the three separate piezo sheets without the need for soldering of leads. Early attempts at lead soldering proved to be extremely tedious and often led to center tab breakage due to the extremely brittle nature of piezoceramics. The specimen holder features a copper finger assembly that applies an even, spring-loaded pressure to the piezo, holding it firmly. This ensures that the voltage is applied directly to the conductive gold-coated surface and acts to hold the one end of the stack firmly in place. This second important function provides a "fixed end" and a "free end," which should facilitate cracking at the uninhibited end in an opening (K_I) mode. A prototype specimen holder was manufactured at Rockwell Science Center consisting of four copper finger assemblies soldered to copper plates. They were aligned with insulation paper separating the inner and outer layers, and a plastic spacer separating the inner layers. The copper fingers were situated a fixed distance apart by two nut and bolt assemblies that attached the copper finger assembly to a plastic base. This specimen holder functioned quite well as far as applying the voltage; however, it was difficult to insert and remove the specimens without breaking the center tab of the specimen. The specimen holder was redesigned, and a second one manufactured at the central machine shop at MIT. The concept for the specimen holder was the same, utilizing copper fingers to hold the specimen in place, but the pressure of the copper fingers can be varied via a nylon wing nut. The two halves of the specimen holder were consolidated and could be opened so that the specimen

could be inserted and removed easily. Once in place, the wing nut could be tightened, applying an even pressure that resulted in no breakage of any specimen. The body of the second specimen holder is aluminum with insulating plastic and paper separating all the conductive areas. Photographs of the completed holder are shown in Figure 12. The specimen holder was clamped to a fiberglass platform on a ring stand to raise it to the level of the long-range microscope used in testing.

Voltage Interrupt Box

Initially, it was thought that measuring capacitance and resistance could reveal information about the fatigue of the solder during testing. It was decided to monitor the capacitance and resistance during testing using a Hewlett-Packard Capacitance Analyzer. However, because the HP analyzer could be damaged by voltage input from the specimen, the power to the specimen had to be shut off before the measurement could be taken. Rather than turn off the power supplies or the H-bridge circuit, it was decided to create a voltage interrupt box utilizing a simple switching mechanism that would either connect the specimen with the power supplies or the HP analyzer but never at the same time. A separate switch was used for each of the four leads running from the circuit box to the specimen holder. Later, it was proven that capacitance was not a useful indicator of solder fatigue activity. However, the interrupt box, although no longer needed for the capacitance measurements, was still used because it was an effective method of interrupting voltage to the specimen very quickly should a problem, such as sparking or extremely rapid crack growth, occur during testing.

Thermal Box

A Styrofoam insulated thermal box with a transparent plastic window was constructed for *in situ* monitoring of crack growth for elevated and reduced temperature testing. This box is a prototype and is not intended for long-term usage. The box was constructed to verify that temperature does have an effect on the fatigue behavior of solder joints; for further testing, it is strongly recommended that a more robust thermal chamber be constructed. The challenge of this thermal box was that it had to allow for visual *in situ* monitoring of the crack growth and be able to both cool and heat the specimen. Therefore, a unique, yet rudimentary, thermal chamber was constructed.

Two layers of 3/4 inch-thick Styrofoam sheet were used to construct the box. The sides were joined with white glue suitable for use with Styrofoam. Nails held the foam in place while the glue dried. On the six-sided box, five sides are fixed, and the sixth or front of the box is removable so that the specimen holder can be inserted. The face of the box also contains the window, which is inset in the Styrofoam with white glue. A Styrofoam ledge was installed in the box to enable the specimen holder to rest (unclamped) so that the specimen is clearly visible through the window. The box has holes for the input voltage wires to the specimen holder (no ring stand required) and a hole for a thermometer to monitor temperature. A photo of the box is shown in Figure D1.

The box is cooled and heated by a thermoelectric device, or Peltier junction, which uses a doped semiconductor-based electronic component to function as a small heat pump (Ferrotec-America, model P/N 6320/157/040). By applying a low voltage DC power source, the module moves heat from one side to the other, creating one face that heats and one face that cools. The concept is analogous to a mechanical refrigerator. The heating direction of the thermoelectric device may be inverted by simply switching the polarity of the applied electric field. Fins are adhered to the heating and cooling faces to facilitate heat dissipation. The fins are held in place with thermal grease (Ferrotec-America, AOS Heat Sink Compound-400), an exceptionally soft, non-silicone grease. This specially formulated grease is designed to not harden, degrade, or migrate under normal use within temperature environments from -40°C to 200°C. This ensures excellent heat transfer between the thermoelectric device and the cooling fins. Aluminum wire was then wrapped around the entire assembly to hold the fins securely in place. A photo of the thermoelectric device with attached fins is shown in Figure D2. The device is placed such that half of it is inside the thermal box and other half outside the box, with Styrofoam insulation filling the gaps as much as possible. Heat sinks of a metal plate and a bath of ice water are used for the heating and cooling modes respectively. To ensure the temperature inside the box is uniform, a fan is placed over the fins of the thermoelectric device. Using a 20 V, 1 A power supply, a temperature of 80°C could be maintained inside the box when heated and 0°C when cooled. A greater temperature difference could have been realized if a larger power supply were available, since the current rating on the thermoelectric device is 4 A.

To perform the testing, first the wires of the specimen holder are threaded through the openings in the thermal box. Next, the sample is mounted into the specimen holder. The front face of the box is then fitted onto the box and held in place with masking tape. Next, the box is placed on top of the thermoelectric device. If heating is desired, the positive lead from the device is connected to the positive terminal on the power supply and similarly with the negative lead. If cooling is desired

inside the box, then the negative lead from the thermoelectric device is connected to the positive terminal on the power supply and similarly with the positive lead. The power supply is then turned on and the voltage increased until the 1 A current limit of the power supply is reached. As the device heats, the resistance decrease within the device will cause the voltage level of the power supply to drop. The voltage is continually increased as this occurs to continue the heating process. After approximately 20 minutes, the voltage, and subsequently the temperature inside the box, will stabilize. As long as a proper heat sink is maintained outside the box, the temperature inside the box will remain constant. This is a challenge for the tests at 0°C; ice must be continually added to the ice bath surrounding the cooling fins outside the box. As the device pumps heat out of the box (cooling mode), the heat melts the ice. Water must be siphoned off, and more ice added approximately every 15 minutes to maintain the temperature inside the box. Temperature was monitored continuously using a thermometer and was kept within ± 2°C during testing. Crack growth measurements are then performed following the same procedure as those taken at room temperature.

Procedures

Crack Length

The primary objective of this study is to investigate crack growth during piezo-induced solder fatigue. One of the benefits of the piezomechanical approach to fatigue testing is that the cracking can be optically monitored and measured *in situ*. A long range microscope manufactured by Questar, Inc. of New Hope, PA was used to measure solder fatigue crack length. The microscope with a 2X magnification lens was used. The image from the microscope was fed through a single charged coupled device (CCD), black and white digital video camera into a television monitor. A digital measuring system with resolution up to 0.01 mm monitored the x-y-z positions of the Questar microscope's stage based on the manual adjust knobs on the microscope's base. The x-direction was used for measuring crack length and the z-direction for measuring crack opening displacement. For measuring reference, cross-hairs were drawn on a transparency, which was taped to the television monitor. To begin testing, the specimen was carefully inserted and tightened into the specimen holder. The Questar microscope was then focused on the plane of the specimen, and the plane of the microscope's optics was made parallel with the surface of the specimen by rotating the specimen stand or the microscope itself. This ensured that a fatigue crack would remain in focus along the length of the specimen or only require slight focusing adjustments. A severe y-direction misalignment can cause errors in crack length accuracy. The lighting on the

specimen was adjusted for best contrast; both external and beam splitter lighting techniques were used. The entire joint was examined for defects that could act as crack initiators. Any suspect voids or debonded regions were measured. Next the desired input voltage was set on the high voltage power supplies and the desired frequency was set on the function generator. The functionality of the circuit box was checked with a voltmeter on the output terminals. The function generator was halted while the voltage was delivered to the specimen via the voltage interrupt box. The cycling was then started by turning on the function generator. At the same time, a stop watch was started to monitor cycling time. The cycling frequency was slowed at intervals to provide an opportunity to scan the entire joint for crack opening. At frequencies of 1 Hz and lower, there was often no need to slow the actuation frequency for crack measurements. A crack appeared as a dark line either inside the solder or along an interface. If it were truly a crack, an opening relative to the piezo adherends was apparent. The crack length was measured by first aligning the cross-hairs at one end of the crack. This was either an internal location or the end of the specimen (free or fixed). The stage of the microscope was then moved in the x-direction to the tip of the crack. The crack tip was often difficult to see; therefore, the crack length was measured to the point where its opening can no longer be observed. The cycles and length were recorded, and the testing continued. This process continued until either the specimen broke or a certain "run-out" number of cycles was reached. The latter was only used if the specimen showed no cracking or was cracking at an extremely slow rate. Tests were as short as 1 hour for high voltages and frequencies, and as long as several days for low voltages and frequencies.

Crack Opening Displacement

Crack opening displacement measurements were made when a crack reached the free end of the specimen and opened in I (opening) mode. The procedure was identical to the crack length measurements except that the stage of the microscope was moved in the z-direction. Crack opening displacement measurements were made when the specimen exhibited a through-thickness crack with a planar crack front; therefore, only a few of these data sets exist. Figure 15 demonstrates a crack opening from the free end.

Capacitance/Resistance

The capacitance and resistance of the solder were measured across both solder joints during initial testing. It was hoped that capacitance and resistance measurements could be a sensitive metric to changes occurring in the solder during fatigue. However, the values remained virtually unchanged

over the course of the fatigue life, only deviating at failure when the piezo itself would break. An example of these results is shown in Figure D3. These measurements were discontinued after they were shown to be ineffective.

Appendix D Figures

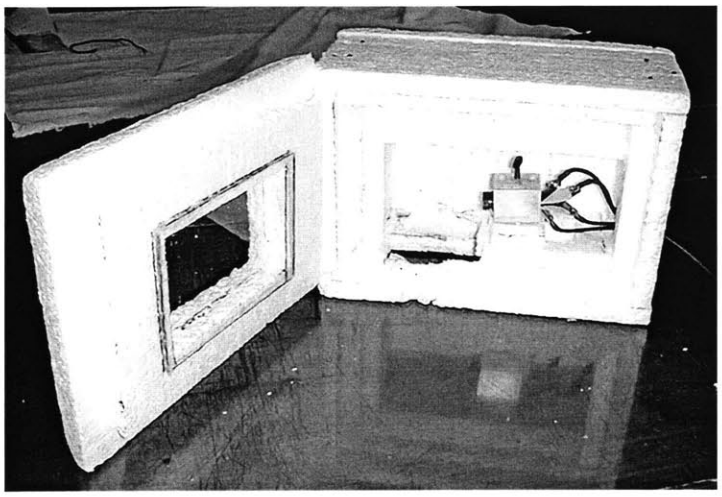

Figure D1: Photograph of thermal box.

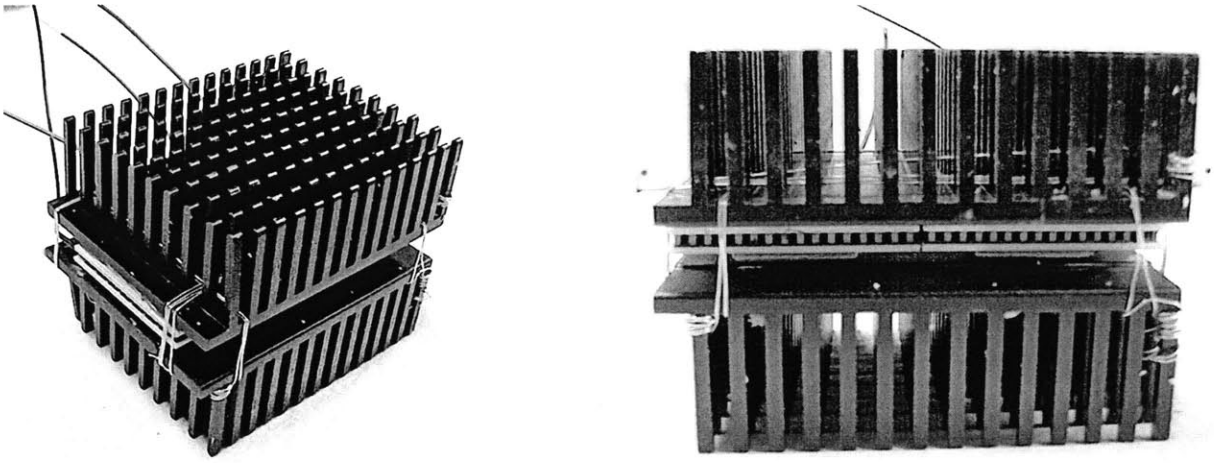

Figure D2: Photograph of thermoelectric device.

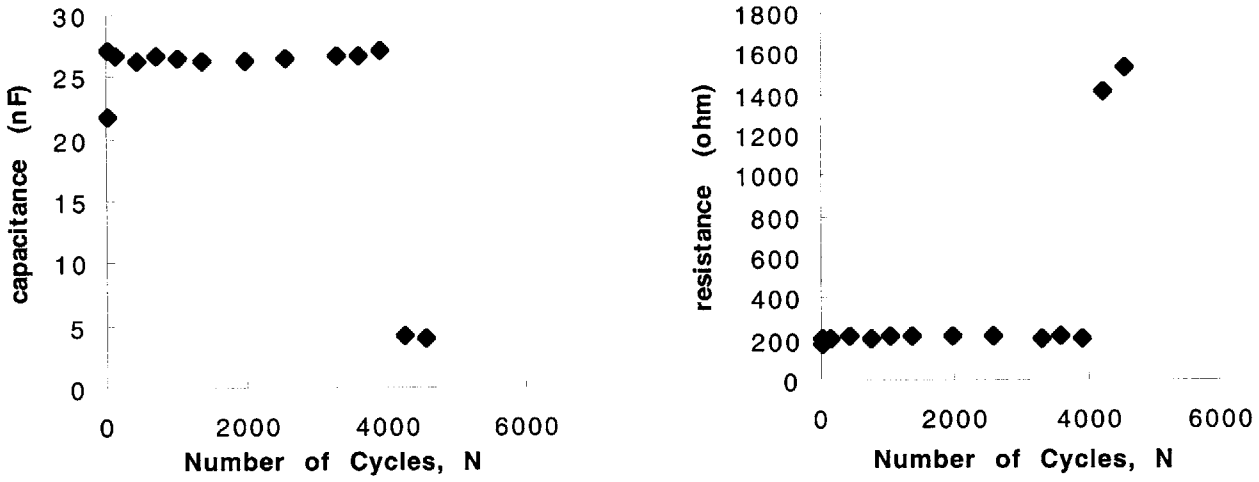

Figure D3: Capacitance (left) and resistance (right) measurements of solder joint during fatigue testing. The final drop in capacitance and rise in resistance was caused by failure of the piezo.

Appendix E: Data Analysis

Calculation of Strain Energy Release Rate Amplitude (ΔG)

In order to apply a fracture mechanics technique to the fatigue data, the crack growth rate must be plotted versus the strain energy release rate amplitude, ΔG.

Strain energy release rate is calculated for a single crack growing in a double symmetric joint, as shown in Figure 11, by subtracting the strain energy associated with the intact bond in the crack wake from the total strain energy that would be released if both bonds were breaking.

The total strain energy release rate is given by:

$$G = \frac{U_A - (U_B + U_C)}{w\,da} \tag{18}$$

The strain energy for region A is given by equation 17, above.

$$U_A = \frac{3}{2} d_{31}^2 \frac{E}{t} (\Delta V_1 + \Delta V_2)^2 \tag{19}$$

Region B is stress free, therefore $U_B = 0$.

$$U = \int \frac{\sigma^2}{2E} tb\,da \tag{20}$$

Region C requires the evaluation of the strain energy in a bilayer, bimaterial strip. This is obtained by enforcing considerations of equilibrium of forces and bending moments and the compatibility of strains and curvatures in the two layers (Spearing, 1996). Hence:

$$U_C = \frac{\beta^2 \xi^2 t_1 (\lambda\xi^2 + 1)}{2E_1} \left[\xi^2 (\lambda\xi + 1)(\lambda\xi^3 + 1) + 3\lambda\xi^3 (\xi + 1)^2 \right] \tag{21}$$

where

$$\beta = \frac{\varepsilon_p E_1}{\xi (\lambda\xi^3 + 1)(\lambda\xi + 1) + 3\lambda\xi^2 (\xi + 1)^2}\ ,\ \varepsilon_p = \frac{d_{31}}{t}(\Delta V_1 + \Delta V_2)\ ,\ \xi = \frac{t_1}{t_2}\ ,$$

$$\text{and } \lambda = \frac{E_1}{E_2}$$

In the case corresponding to the experiments in which the piezoceramic substrates are made of the same material with the same thickness, $\lambda = \frac{E_1}{E_2} = 1$, ξ=1

This simplifies to:

$$\Delta G = \frac{13}{48}\frac{E}{t} d_{31}^2 \left(\Delta V_1 + \Delta V_2\right)^2 \tag{22}$$

The equation for ΔG was given in equation 22 as:

$$\Delta G = \frac{13}{48}\frac{E}{t} d_{31}^2 \left(\Delta V_1 + \Delta V_2\right)^2$$

E is the modulus of elasticity of the piezoceramic adherend, given as 62 GPa by the manufacturer. The thickness, t, is the height of the adherend, which was measured at 0.1905 mm (7.5 mil), and d_{31} is the piezoelectric strain coefficient as determined by the piezoceramic characterization described in Appendix B. The sum of ΔV_1 and ΔV_2 represent the total actuating voltage of the out-of-phase piezos, taking into account that the piezos are moving in opposite directions. For example, if the center piezo is experiencing a ΔV_1 of -150 V, and the outer piezos are experiencing a ΔV_2 of +250 V, values are added to achieve 400 V total because the piezos are straining in opposite directions, which increases the shear strain in the solder. Substituting into this equation, the strain energy release rate was calculated for each testing scenario, as shown in Table E1.

Correction of d_{31} for Temperature

The piezoelectric strain coefficient, d_{31}, varies with temperature in PZT 5H. The percentage of deviation from the room temperature d_{31} is given by the manufacturer as shown in Figure E1. For the high and low temperature testing, a new d_{31} was calculated accommodating for this deviation. At 80°C, the d_{31} is 22.6% greater than the room temperature d_{31} and at 0°C, the d_{31} is 5.4% less than the room temperature d_{31}.

Calculation of Shear Strain ($\Delta\gamma$)

The shear strain of the solder joint is calculated using shear lag analysis, as given equation in 13:

$$\Delta\gamma_{\max} = \frac{1}{2h\tau}\left(\vec{E}_1 d_{31,1} + \vec{E}_2 d_{31,2}\right)^2 \left(\frac{E_1 t_1 E_2 t_2}{E_1 t_1 + E_2 t_2}\right)$$

Since the adherends are made from the same PZT material, $E_1 = E_2$, $t_1 = t_2$, and $d_{31,1} = d_{31,2}$, simplifying the above equation to:

$$\Delta\gamma_{max} = \frac{d_{31}^2 E}{4h\tau t}\left(\Delta V_1 + \Delta V_2\right)^2$$

where $\left(\Delta V_1 + \Delta V_2\right)$, E, t, and d_{31} are given above. The height of the solder joint, h, is 0.0254 mm (1 mil) and the shear strength of solder, τ, is 37 MPa. Solder shear strain values for each actuation scenario are given in Table E1.

Crack Growth Data

Each data set collected in this study is presented in Appendix F. For a given voltage and frequency, the crack length versus number of cycles was plotted. This data was then imported into MacCurveFit™, and a linear regression was performed. The slope of the line was recorded as the crack growth rate or da/dN. The data was only fit through zero if cracking initiated immediately from the onset of testing. Since most specimens exhibited a period of cycling before the onset of cracking (initiation), a forced fit through zero would skew da/dN. If clear initiation and steady state crack growth regions were apparent in the data, the linear regression was performed only on the steady state crack growth region. The crack growth rate was then plotted versus strain energy release rate. Cycles to initiation, or the number of cycles accumulated for a crack to reach an arbitrary two mm criterion, were plotted versus shear strain.

Appendix E Tables

Table E1: ΔG and $\Delta\gamma$ values for each testing scenario.

ROOM TEMPERATURE:

Voltage	ΔG	Δγ
$100\,V_{DC} \pm 100\,V_{AC}$	0.942	0.00093
$100\,V_{DC} \pm 110\,V_{AC}$	1.197	0.00118
$100\,V_{DC} \pm 120\,V_{AC}$	1.494	0.00147
$100\,V_{DC} \pm 130\,V_{AC}$	1.836	0.00180
$100\,V_{DC} \pm 140\,V_{AC}$	2.228	0.00219
$100\,V_{DC} \pm 150\,V_{AC}$	2.673	0.00263
$100\,V_{DC} \pm 160\,V_{AC}$	3.176	0.00312
$100\,V_{DC} \pm 175\,V_{AC}$	4.048	0.00398
$100\,V_{DC} \pm 190\,V_{AC}$	5.073	0.00498
$100\,V_{DC} \pm 200\,V_{AC}$	5.849	0.00575

0°C:

Voltage	ΔG	Δγ
$100\,V_{DC} \pm 160\,V_{AC}$	2.806	0.00276
$100\,V_{DC} \pm 180\,V_{AC}$	3.863	0.00379
$100\,V_{DC} \pm 200\,V_{AC}$	5.168	0.00508
$100\,V_{DC} \pm 220\,V_{AC}$	6.757	0.00664

80°C:

Voltage	ΔG	Δγ
$100\,V_{DC} \pm 130\,V_{AC}$	2.869	0.00282
$100\,V_{DC} \pm 140\,V_{AC}$	3.481	0.00342
$100\,V_{DC} \pm 160\,V_{AC}$	4.963	0.00487
$100\,V_{DC} \pm 180\,V_{AC}$	6.830	0.00671

Appendix E Figures

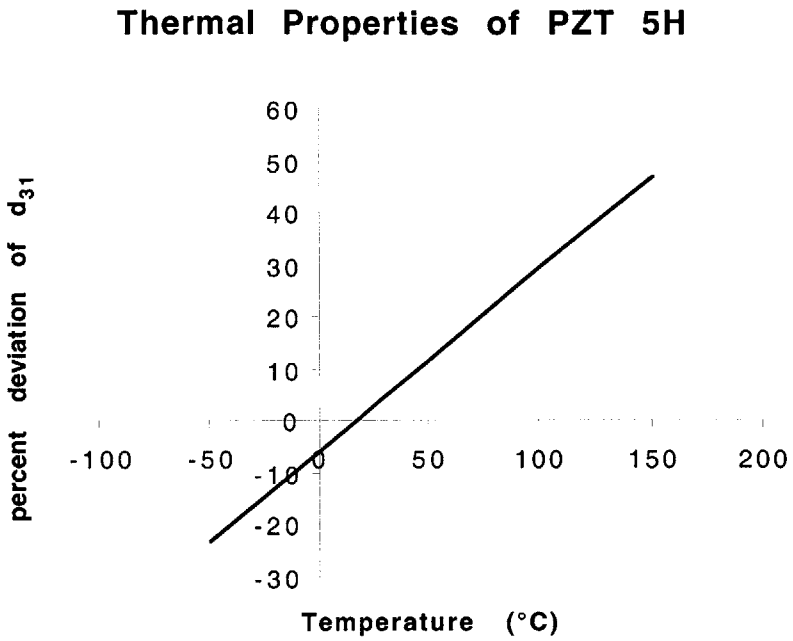

Figure E1: Thermal properties of PZT 5H (Piezo Systems, Inc.).

Appendix F: Crack Growth Data

Room Temperature:

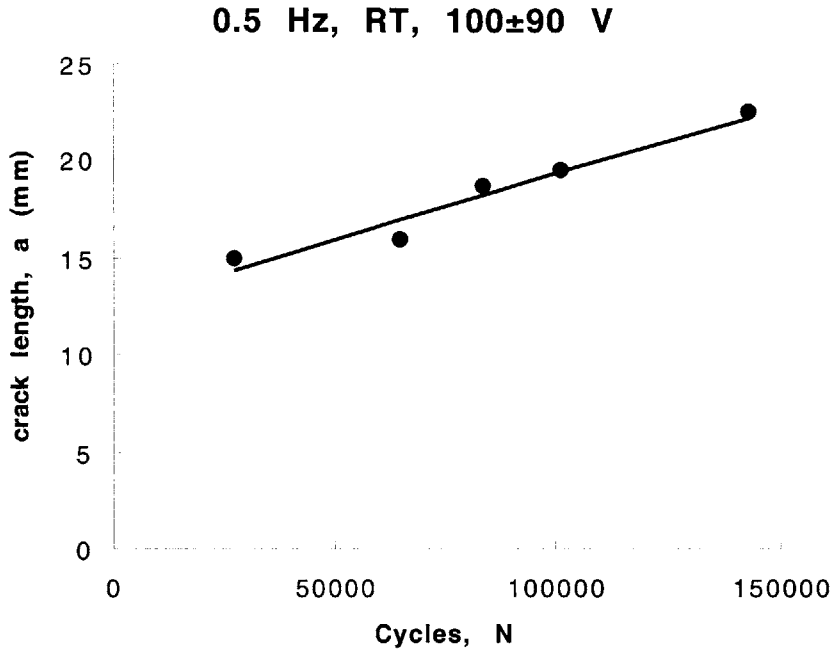

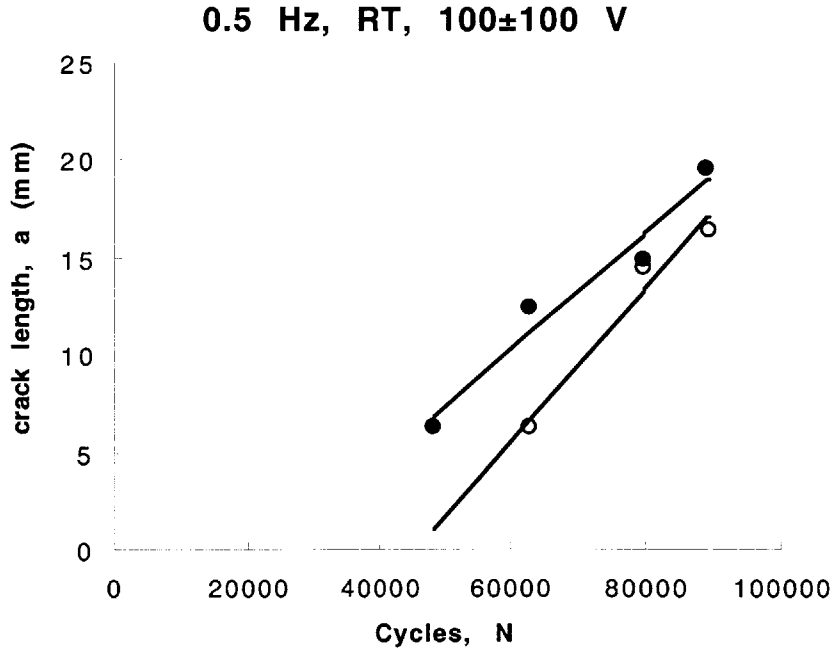

Two data sets and line fits indicate two cracks running simultaneously in the same specimen.

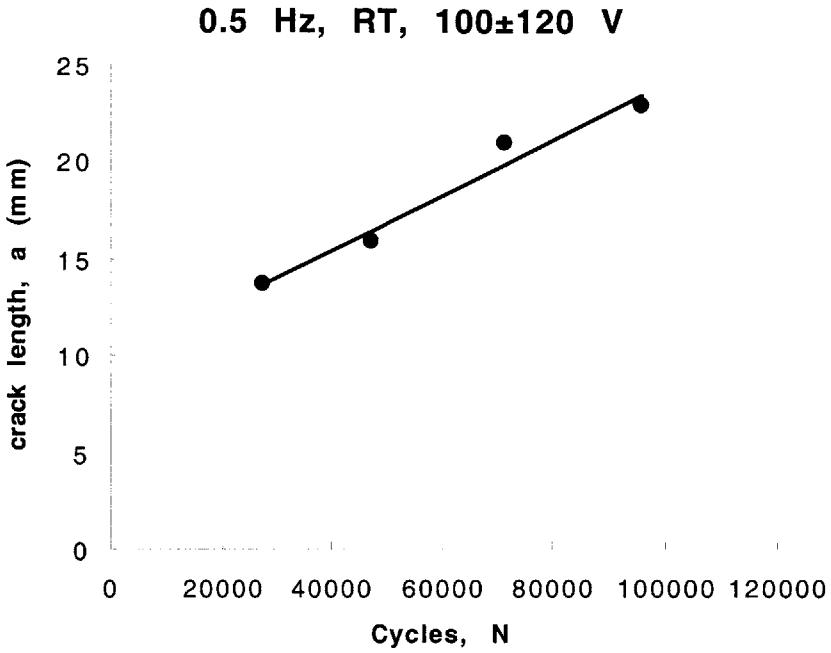
0.5 Hz, RT, 100±120 V
crack length, a (mm)
25
20
15
10
5
0
0
20000
40000
60000
80000
100000
120000
Cycles, N

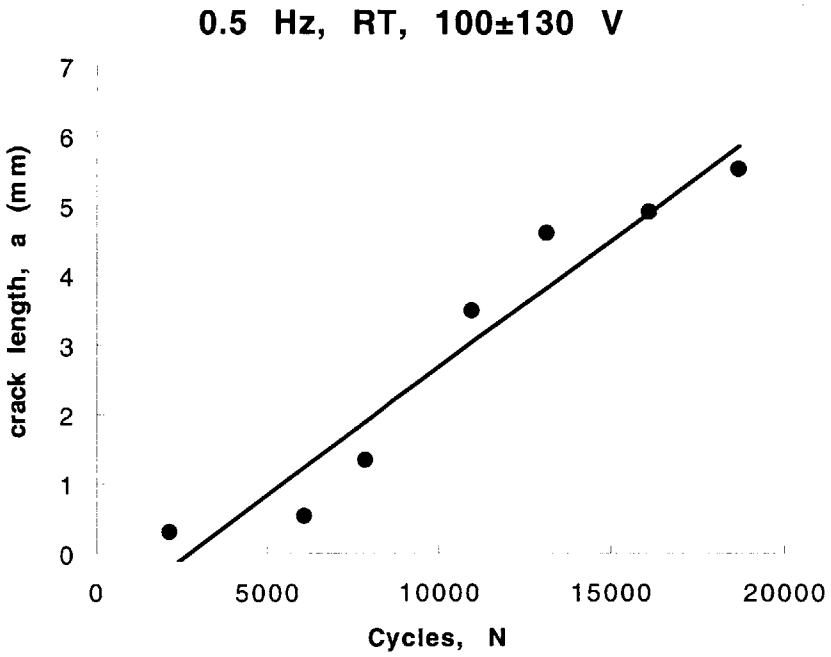
0.5 Hz, RT, 100±130 V
crack length, a (mm)
7
6
5
4
3
2
1
0
0
5000
10000
15000
20000
Cycles, N

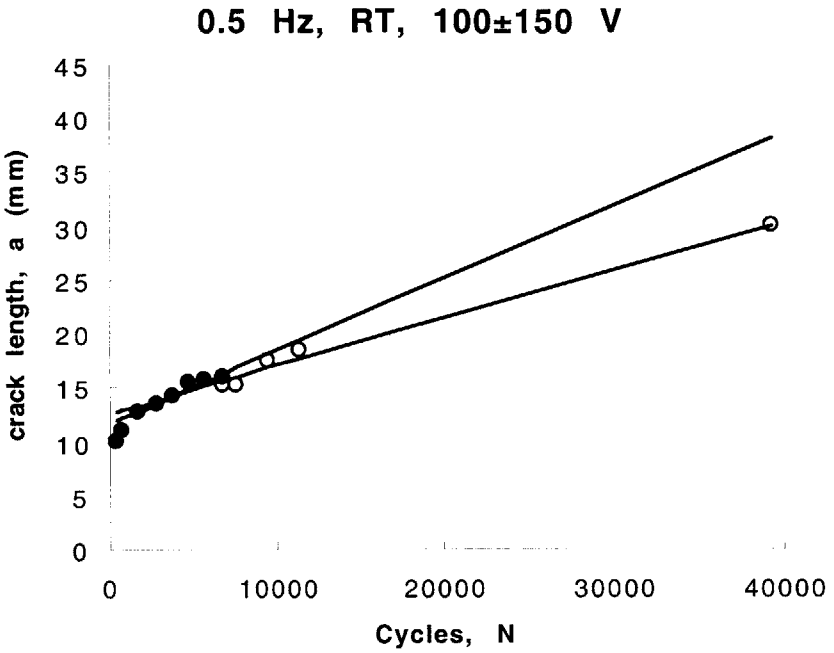

Two data sets and line fits indicate two cracks running simultaneously in the same specimen.

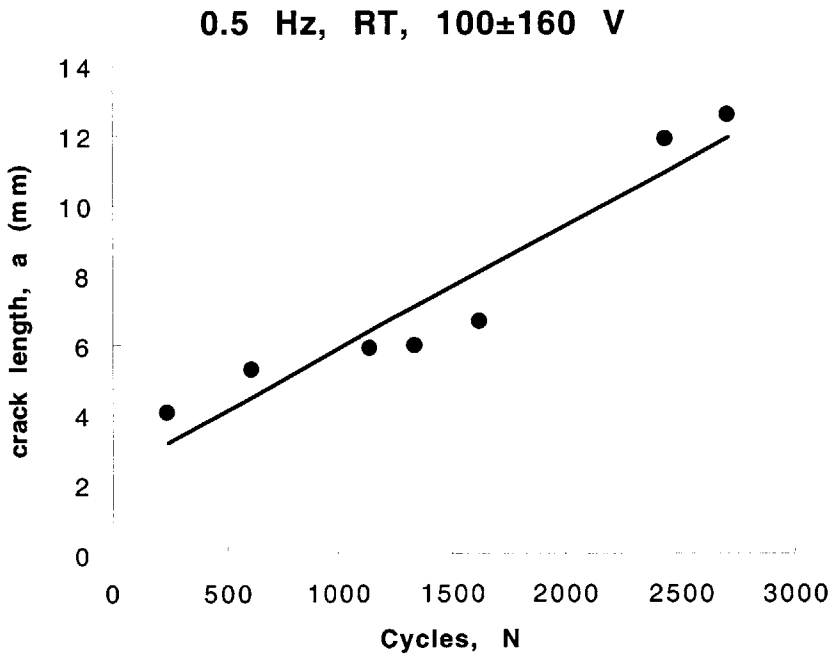

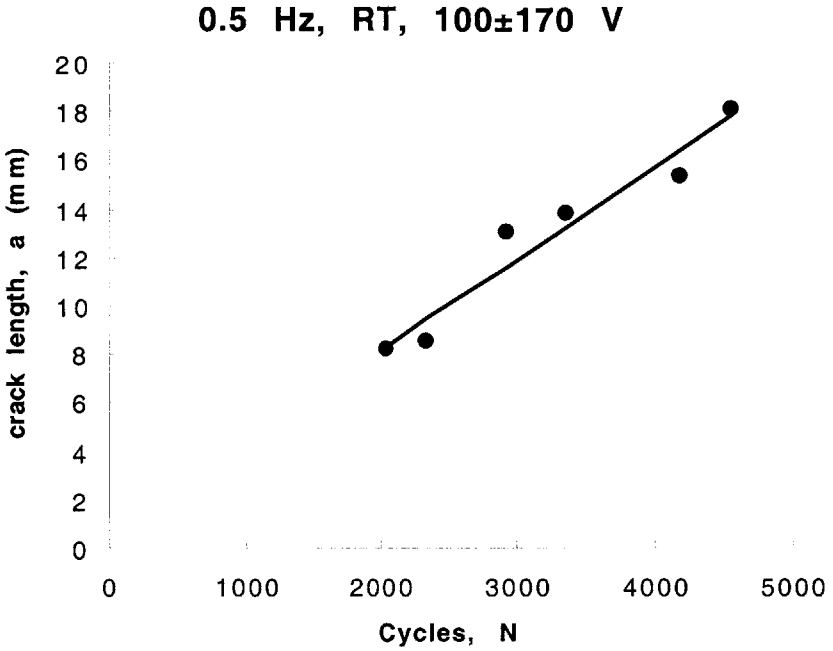
0.5 Hz, RT, 100±170 V
crack length, a (mm)
20
18
16
14
12
10
8
6
4
2
0
0
1000
2000
3000
4000
5000
Cycles, N

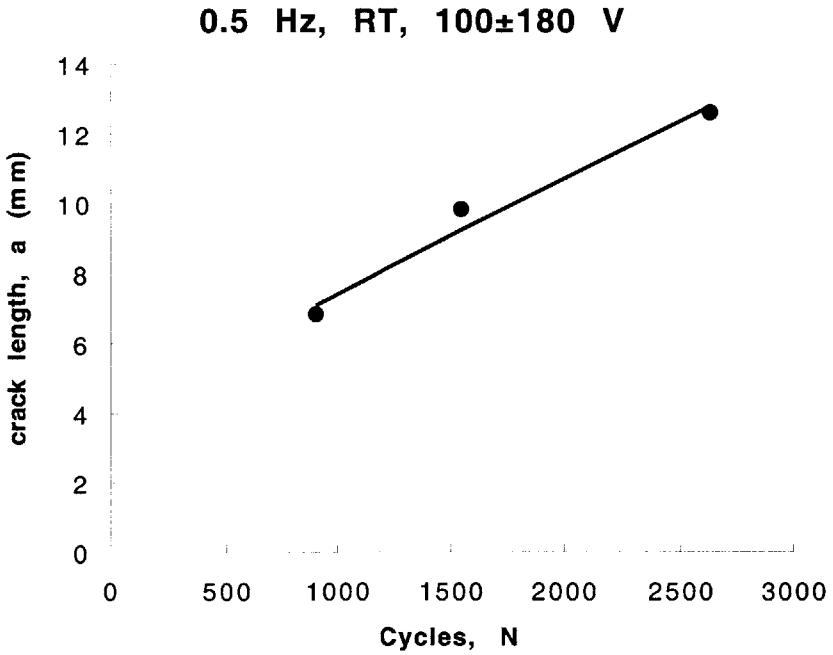
0.5 Hz, RT, 100±180 V
crack length, a (mm)
14
12
10
8
6
4
2
0
0
500
1000
1500
2000
2500
3000
Cycles, N

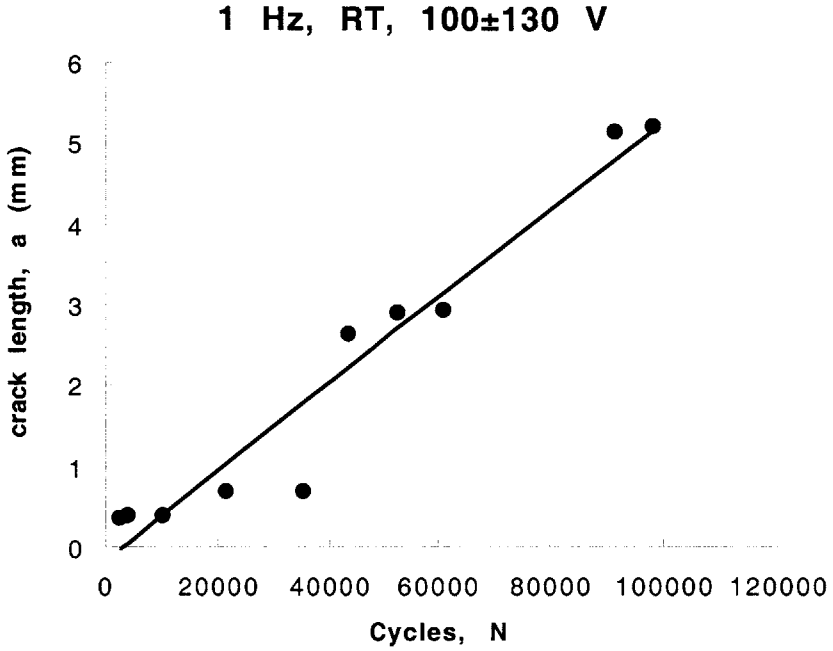
1 Hz, RT, 100±130 V
crack length, a (mm)
0
1
2
3
4
5
6
0
20000
40000
60000
80000
100000
120000
Cycles, N

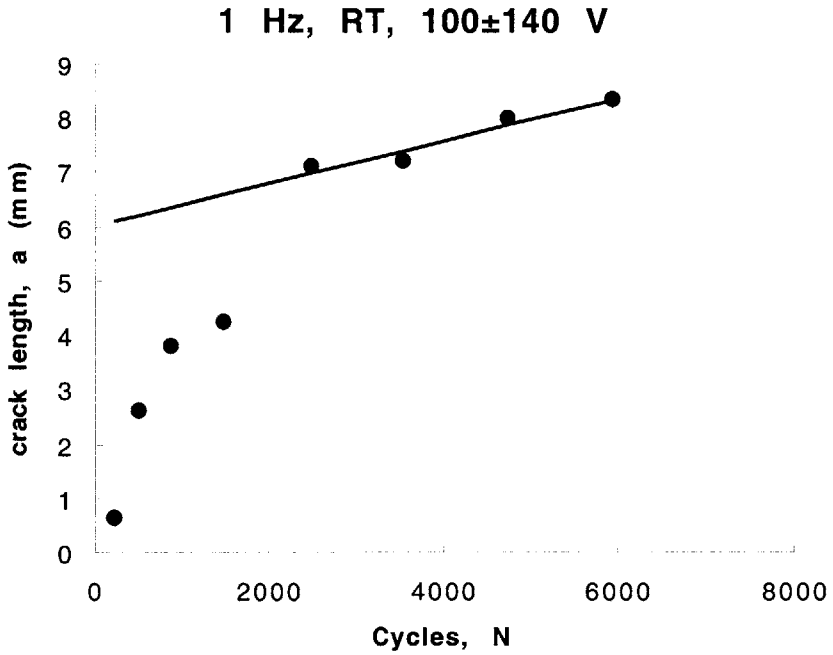
1 Hz, RT, 100±140 V
crack length, a (mm)
0
1
2
3
4
5
6
7
8
9
0
2000
4000
6000
8000
Cycles, N

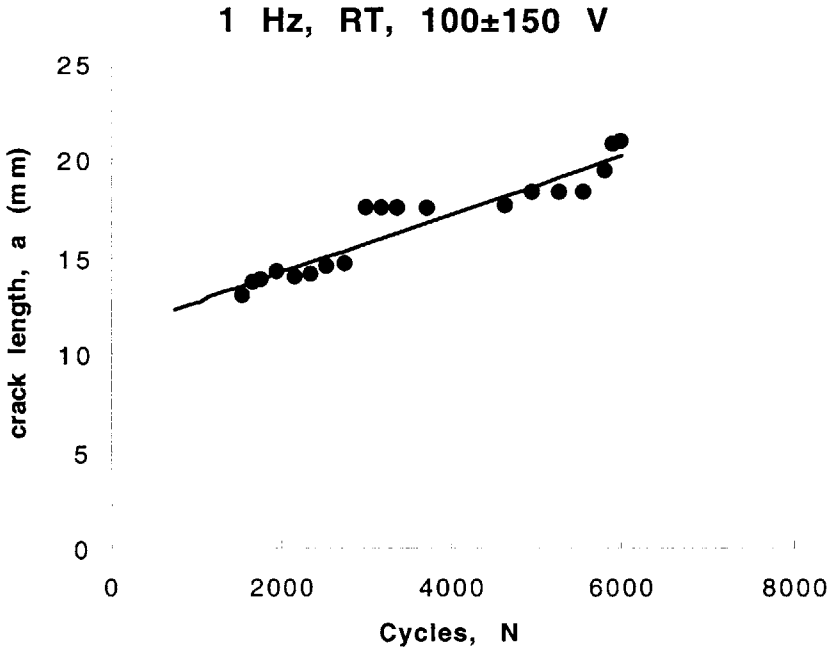
1 Hz, RT, 100±150 V
crack length, a (mm)
25
20
15
10
5
0
0
2000
4000
6000
8000
Cycles, N

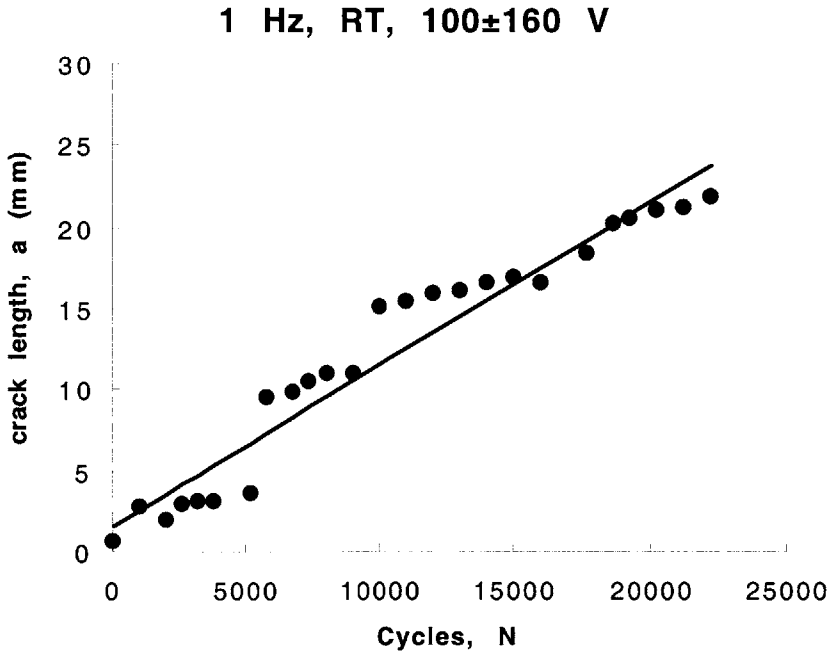
1 Hz, RT, 100±160 V
crack length, a (mm)
30
25
20
15
10
5
0
0
5000
10000
15000
20000
25000
Cycles, N

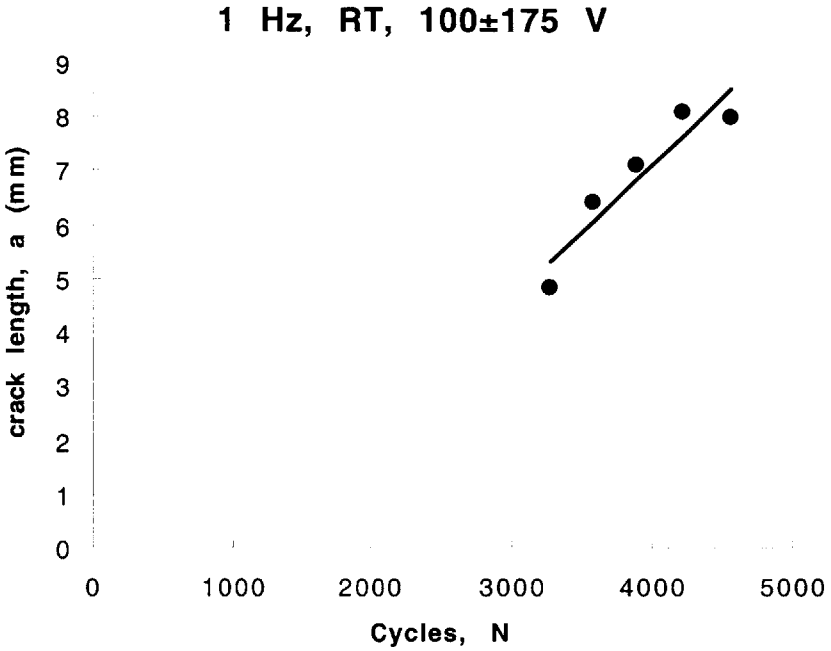
1 Hz, RT, 100±175 V
crack length, a (mm)
0
1
2
3
4
5
6
7
8
9
0
1000
2000
3000
4000
5000
Cycles, N

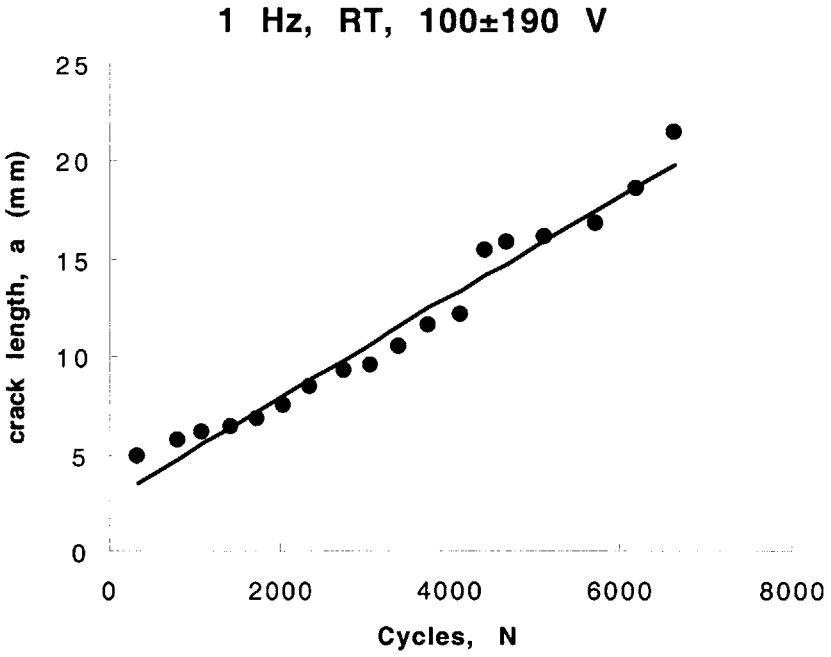
1 Hz, RT, 100±190 V
crack length, a (mm)
0
5
10
15
20
25
0
2000
4000
6000
8000
Cycles, N

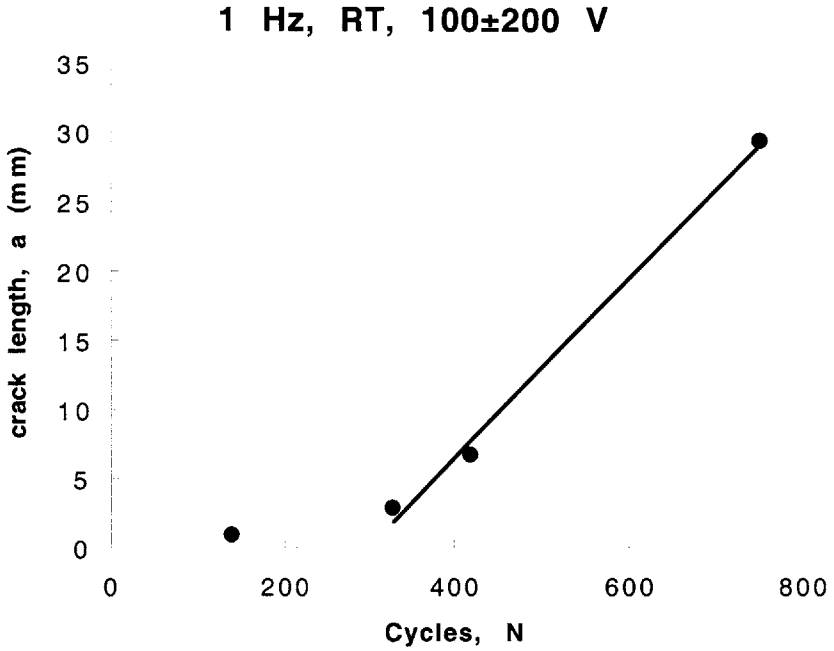
1 Hz, RT, 100±200 V
crack length, a (mm)
35
30
25
20
15
10
5
0
0
200
400
600
800
Cycles, N

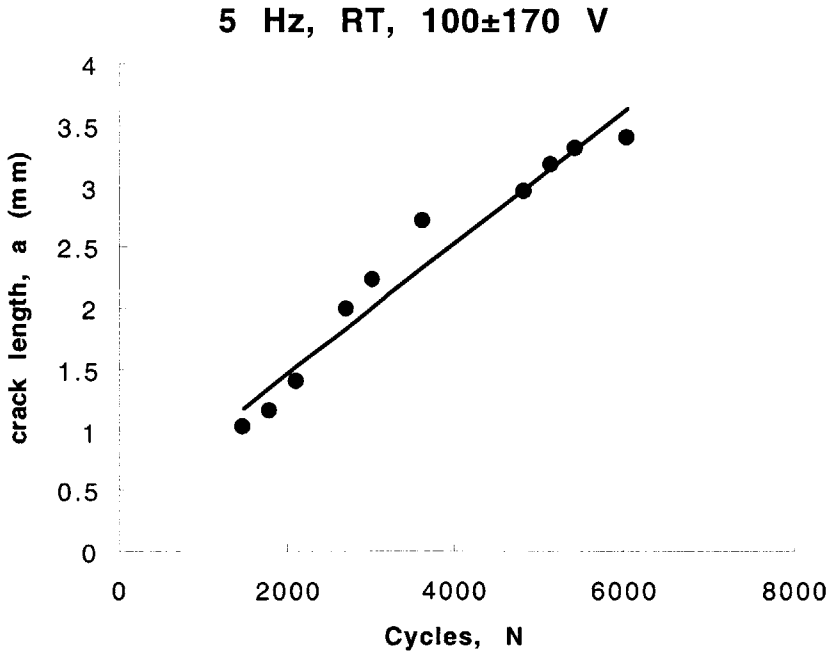
5 Hz, RT, 100±170 V
crack length, a (mm)
4
3.5
3
2.5
2
1.5
1
0.5
0
0
2000
4000
6000
8000
Cycles, N

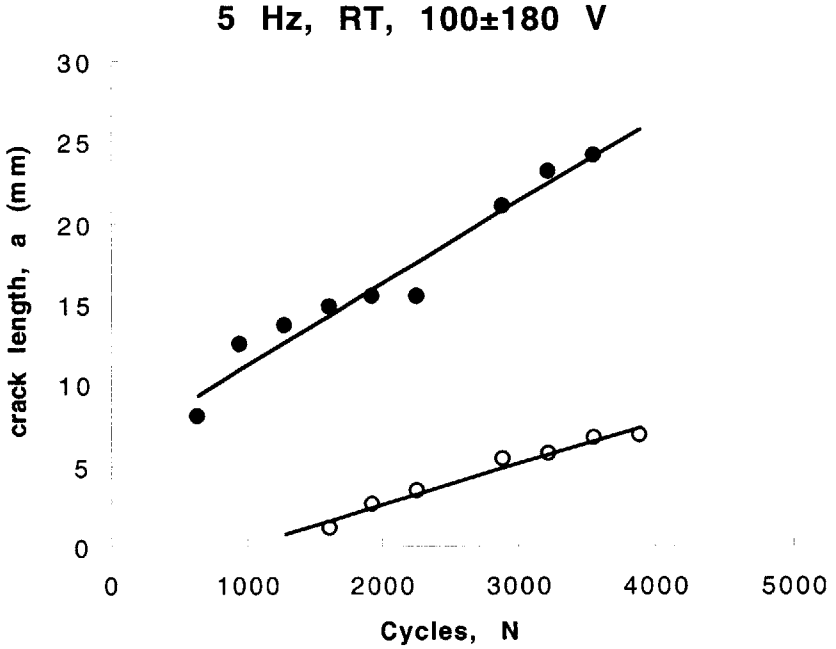

Two data sets and line fits indicate two cracks running simultaneously in the same specimen.

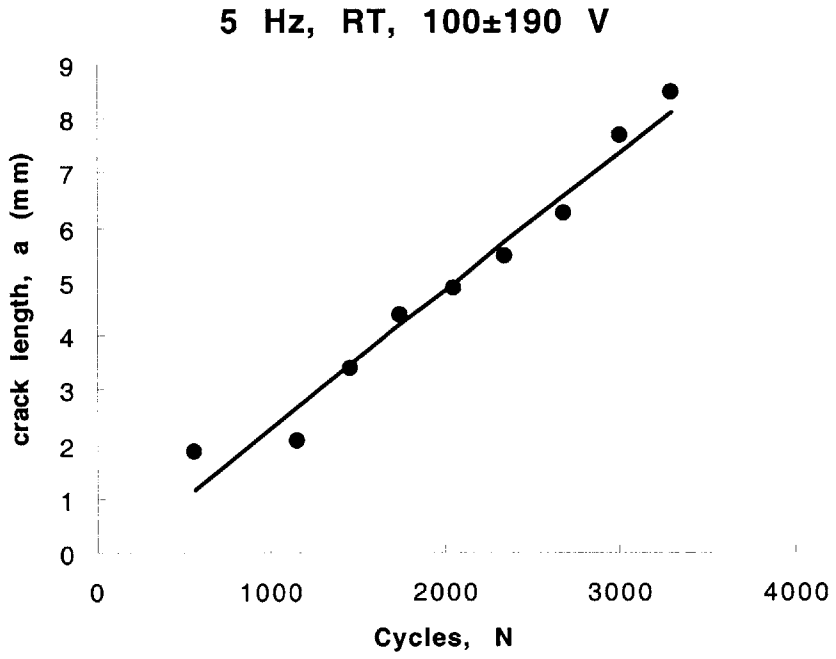

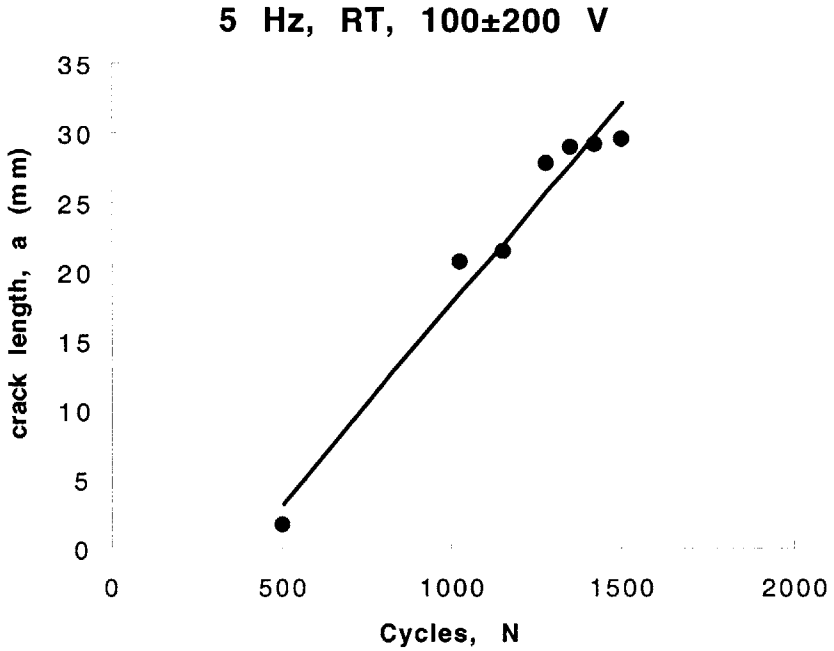
5 Hz, RT, 100±200 V
crack length, a (mm)
35
30
25
20
15
10
5
0
0
500
1000
1500
2000
Cycles, N

0°C:

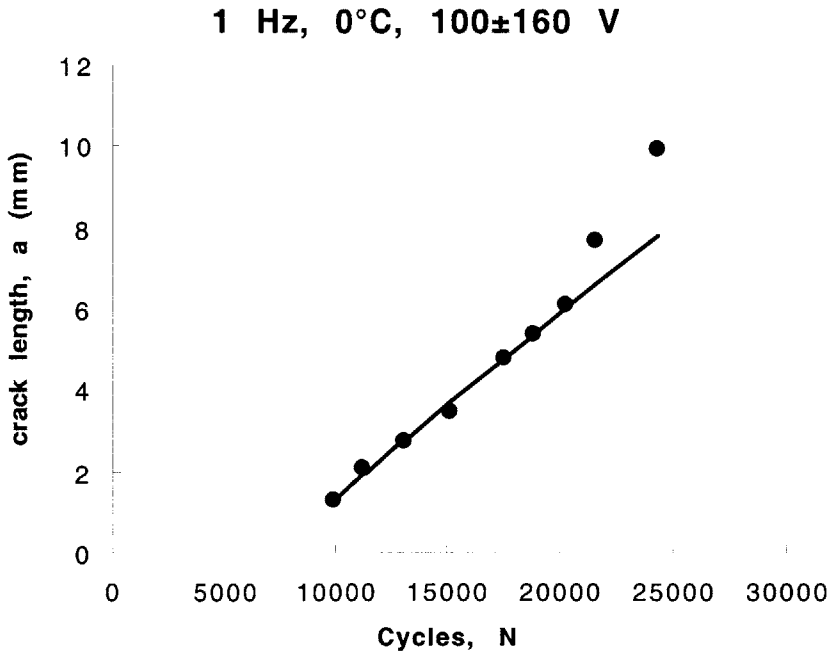
1 Hz, 0°C, 100±160 V
crack length, a (mm)
12
10
8
6
4
2
0
0
5000
10000
15000
20000
25000
30000
Cycles, N

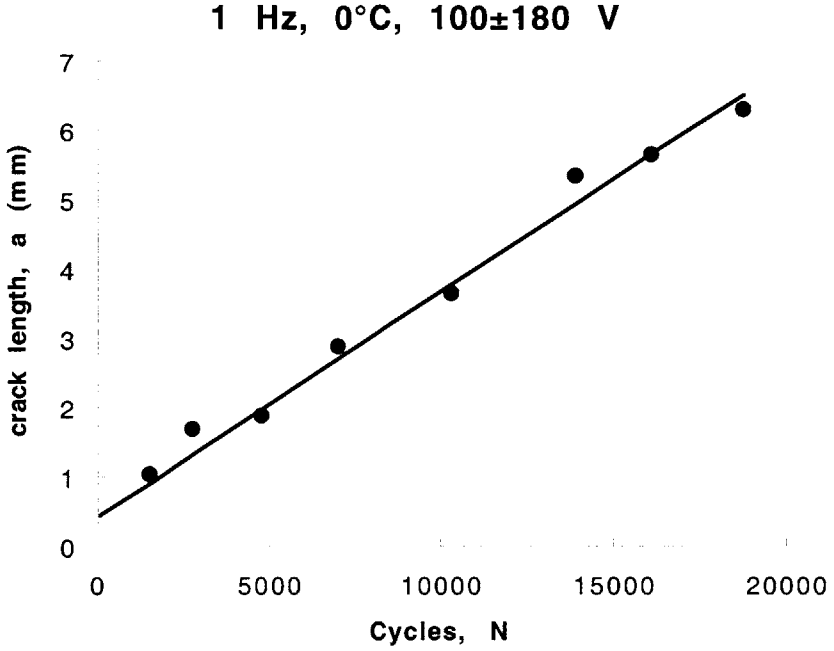

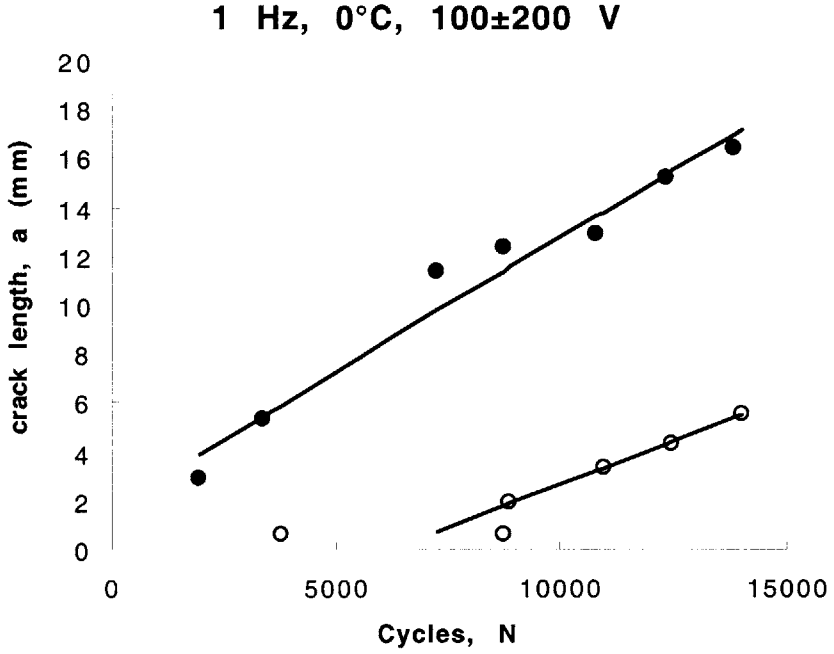

Two data sets and line fits indicate two cracks running simultaneously in the same specimen.

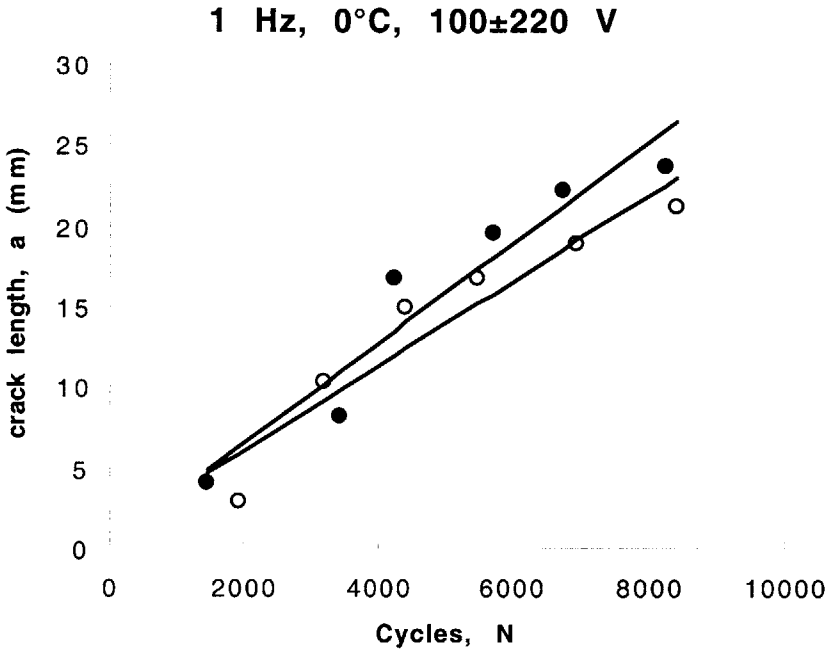

Two data sets and line fits indicate two cracks running simultaneously in the same specimen.

80°C:

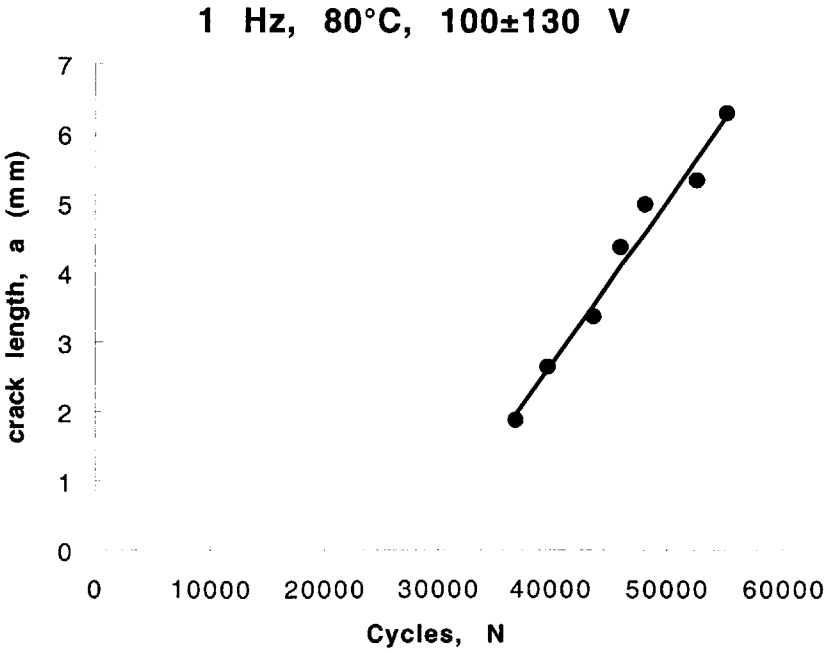

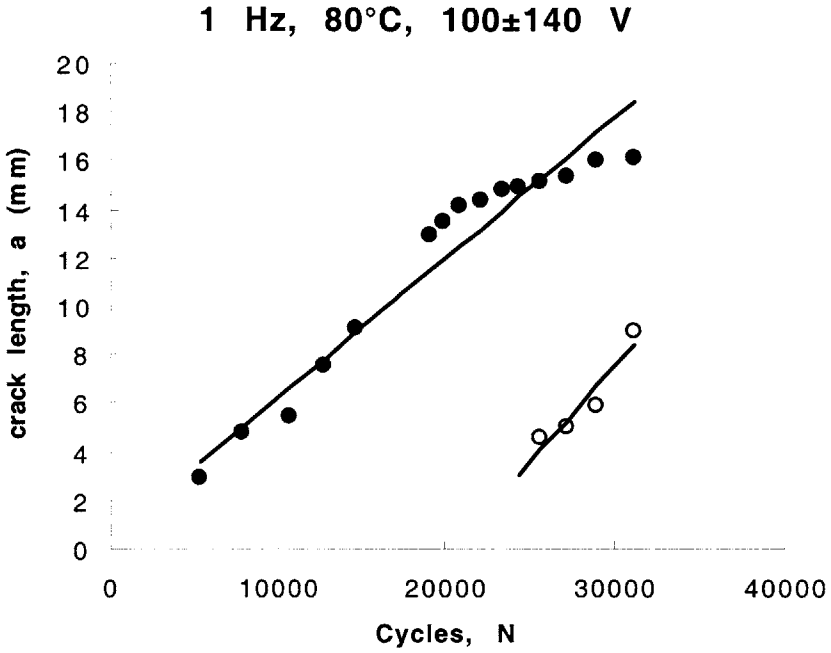

Two data sets and line fits indicate two cracks running simultaneously in the same specimen.

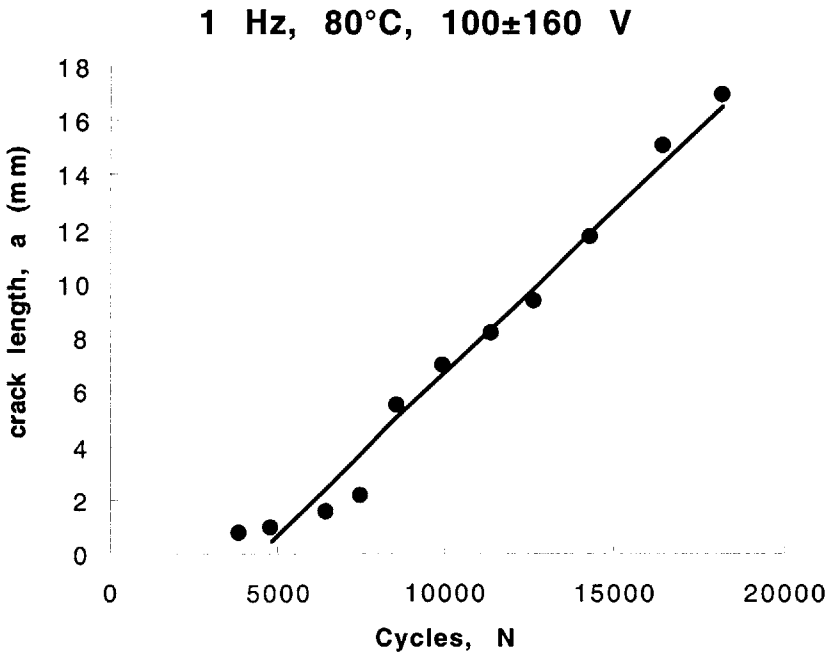

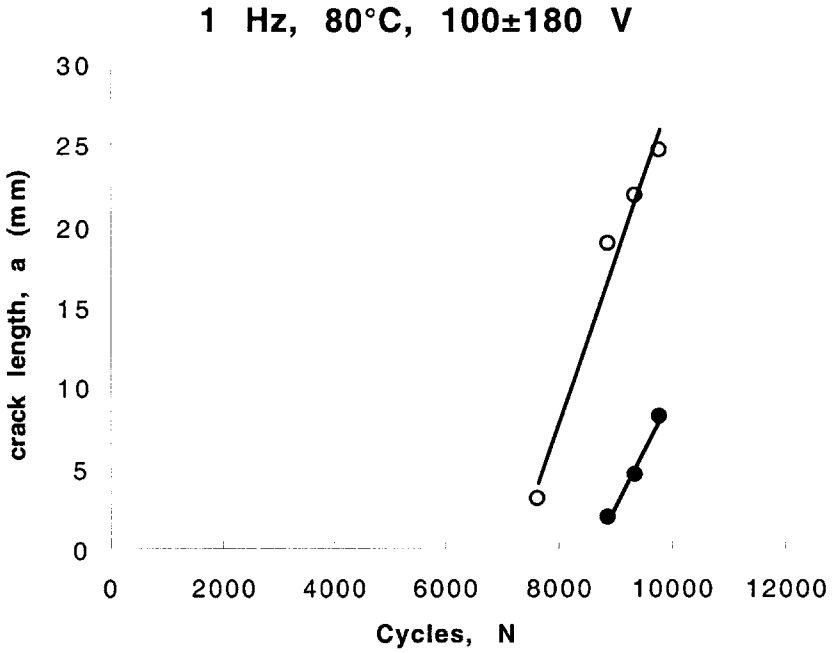

Two data sets and line fits indicate two cracks running simultaneously in the same specimen.